A computational study of self-assembled surfactant systems applications to drug delivery

Allen, Daniel Thomas

Awarding institution:
King's College London

A Computational Study of Self-Assembled Surfactant Systems: Applications to Drug Delivery

Daniel Thomas Allen

Department of Physics

King's College London

A thesis submitted in partial fulfilment of the requirements for the degree of Doctor of Philosophy in Physics at King's College London

30/03/2017

This thesis is dedicated to my family: Steve, Mary and Laura Allen. Their continued love and support has shaped who I am and for this I am eternally grateful.

Acknowledgements

I owe a debt of gratitude to my supervisor Dr Chris Lorenz for giving me the opportunity, the resources and the guidance to complete this thesis, which would not have been possible without him. Thanks to my girlfriend Kasia Katner, who keeps me grounded during my most difficult moments in a way that no one else can. Her unconditional support (particularly in the last few months) is something that I will forever appreciate and never forget. I feel enormously grateful to have completed my PhD alongside so many amazingly talented, diverse, kind and interesting people. Special thanks goes to Marcello Caio, Pooya Azarhoosh, Maxwell Fulford, Alix Le Maroix, Marco Caccin, Marco de Cesare, Krzysiek Bożek, Thomas Helfer, Katy Clough, Alena Vishina, Robert Hogan, Fedor Simkovic, Soraya Caixeiro, Chiara Paris, James Cook and Federico Comitani. I thank all of the people who have so kindly supported me in preparing this thesis in the final stretch, my second supervisor Prof Carla Molteni, Dr Jemma Trick who has always made time to assist me whilst we have worked together and Mateusz Bieniek who's knowledge on computer science has been invaluable to me. A special thanks is owed to Dr Luis Carlos Pardo who welcomed me to Barcelona and kindly spent two weeks working with me. I thank Dr Alessio Comisso, who was incredibly generous with his time and expertise offering support in high performance computing whilst he was working at King's in the early years of my PhD. Thanks to the administrative staff who have assisted me throughout my PhD and who keep the Physics department running so smoothly, Rowena Peake, Simona Kippins, James French and Dr Paul Le Long who

has supported me from the start of this process and who is truly an asset to the department. I thank my collaborators Dr Yussif Saaka and Prof Jayne Lawrence who have provided stimulating discussions and vital input from their experiments to aid my research. Finally, I thank my parents and my sister who this thesis is dedicated to. They have always encouraged me to better myself without putting pressure on me. I couldn't wish for a more loving and caring family.

Publications

The following publications have been produced throughout the course of writing this thesis:

- Atomistic Description of the Solubilisation of Testosterone Propionate in a Sodium Dodecyl Sulfate Micelle. Allen *et al*, (2014), *The Journal of Physical Chemistry B.* 118 (46), 13192–13201

- Molecular Scale Simulations of the Self-Assembly of Amphiphilic Molecules: Current State-of-the-Art and Future Directions. D. T. Allen and C. D. Lorenz, (2015), *The Journal of Self Assembly and Molecular Electronics*, doi: 10.13052/jsame2245-4551.2015006

- Specific effects of monovalent counterions on the structural and interfacial properties of dodecyl sulfate monolayers. Allen *et al*, (2016), *Physical Chemistry Chemical Physics* 18, 30394-30406

- A novel method for constructing continuous intrinsic surfaces of nanoparticles. D. T. Allen and C. D. Lorenz, (2017), Submitted to *The Journal of Molecular Modeling*

- Interaction of the hydrophobic drug, testosterone enanthate, with monolayers of the surfactant, sodium dodecyl sulphate. Y. Saaka, D. Allen *et al*, 2017, Submitted to *ACS Nano*

Abstract

Surfactant aggregate structures in bulk solutions have maintained their crucial importance in science and technology as they have a wide range of applications in a plethora of different industries. Surfactant molecules consist of polar head groups and nonpolar tails. Because of this chemical composition, surfactant molecules spontaneously self-assemble into aggregate structures when their concentration in water exceeds their critical micelle concentration. This thesis focusses specifically on the interaction of drug molecules within surfactant monolayers and micelles. The hydrophobic microenvironment arising from the resulting aggregate structures can be used to enhance the solubility of other, partially soluble substances by a process referred to in the literature as "solubilisation". The encapsulation of these poorly water soluble drug compounds, within surfactant micelles, enables their oral delivery to patients. Sodium dodecyl sulphate micelles show great promise as drug delivery vehicles for hydrophobic compounds in general and the purpose of this thesis is to develop an understanding of how the molecular components of a micellar drug delivery system affect the observed encapsulation ability. Using a combination of atomistic molecular dynamics and well-tempered metadynamics simulations, the interaction of testosterone-based compounds within dodecyl sulphate monolayers and micelles with different counterions has been investigated in detail. In addition, the resulting effects on the structural and interfacial properties of these aggregate structures is investigated thoroughly. The results presented within this thesis show that ammonium ions compete with water molecules to form hydrogen bonds with the

dodecyl sulphate headgroups. In doing so, they result in distinctly different interfacial properties of dodecyl sulphate monolayers compared to those with sodium ions, including the dehydration of the surfactant headgroups. This provides a possible explanation for the recently discovered experimental observation that SDS micelles encapsulate significantly more testosterone-based compounds than ADS micelles, despite the micelles being similar in size. Furthermore, the simulation results reported within this thesis reveal that the orientational behaviour of testosterone-based compounds varies depending on the number of polar interaction sites contained within each molecule. This is an effect which could have profound implications of the encapsulation behaviour of the drug compounds studied. The testosterone-based compounds are used as model drug molecules within the framework of this thesis, however the results obtained will aid the rationale design of new oral medications in the future. Moreover, the novel methods which have ben developed to construct an intrinsic surface of planar and (approximately) spherical interfaces of soft matter have significant scope for application in understanding the interfacial properties of these systems as studied within simulations and also as a collective variable when carrying out enhanced sampling simulations using techniques such as metadynamics.

List of Abbreviations

F-MMM	fluid-mosaic membrane model
CMC	critical micelle concentation
GI	gastrointestinal
MD	molecular dynamics
PPPM	particle particle particle mesh
SDS	sodium dodecyl sulphate
ADS	ammonium dodecyl sulphate
DS^-	dodecyl sulphate
T	testosterone
TP	testosterone propionate
TE	testosterone enanthate
SDM	spatial density map
RMSD	root mean squared deviation
RDF	radial distribution function
CV	collective variable
FES	free energy surface
PMF	potential of mean force
SASA	solvent accessible surface area

Table of contents

List of figures

List of tables

Chapter 1

Introduction

1.1 Self-Assembly

1.1.1 Biological Context

The phenomenon of molecular self-assembly is the cornerstone of life as we know it. The ability of a disordered molecular system to spontaneously form structurally well-defined aggregates, without guidance from an outside source, is observed throughout nature. For example, the major components of eukaryotic cells form spontaneously *in vivo* and are comprised of an astonishing range of complex molecular structures, responsible for performing a wide variety of cellular processes (see Figure 1.1). Such structures include the nucleus which contains the cell's genetic information (arranged in 23 chromosomes for humans), the mitochondria whose primary function is to produce energy in aerobic cells by synthesis of ATP, and the Golgi apparatus which modifies, sorts, and packages macromolecules both for delivery to other organelles and for expulsion from the cell via exocytosis.

The complex and intricate molecular structures contained within the interior of a cell are surrounded by a lipid bilayer membrane, which maintains the physical integrity of the cell whilst also acting as a selectively permeable barrier between

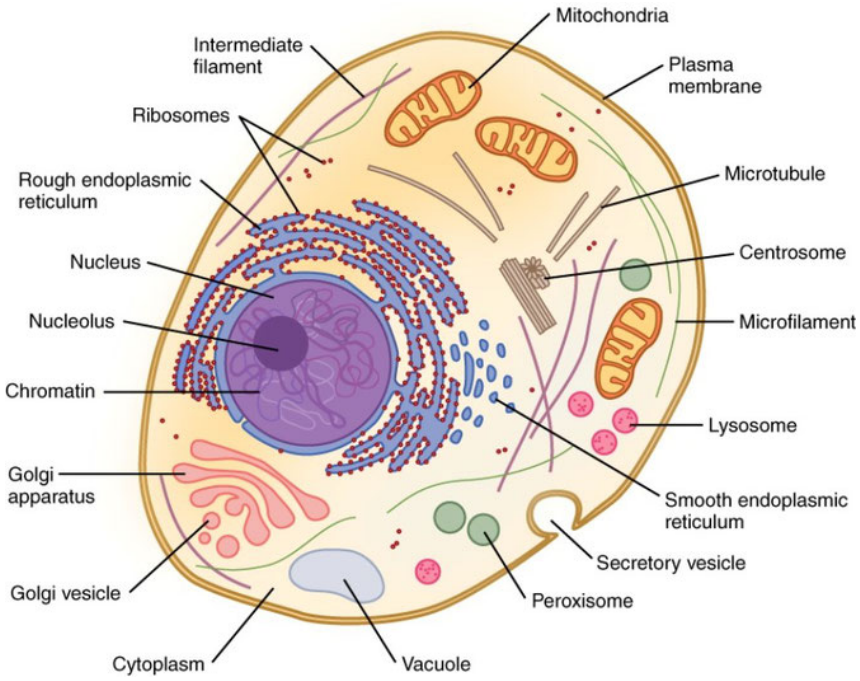

Fig. 1.1: An illustration showing the complex structure of a typical animal cell, including the many organelles found within. (Image adapted from: https://www.withcarbon.com/2014/12/13/animal-cell-parts-and-functions/)

the cell interior and the exterior environment, by controlling the flow of ions and organic molecules in and out of the cell. Additionally, many organelles such as the nucleus, mitochondria and chloroplasts are themselves surrounded by lipid bilayers which are among the most ubiquitous structures in biology.

In 1972, Singer and Nicolson proposed the Fluid-Mosaic Membrane model (F-MMM) [1] to describe the structure of lipid bilayers. In essence, the F-MMM represents biological membranes as a matrix made up of a mostly fluid bilayer of phospholipids with mobile globular proteins intercalated into the fluid lipid bilayer, as depicted in Figure 1.2. Over 40 years later, this simple model of the cell membrane remains relevant for describing the basic nano-structures of membranes in plant, bacteria and animal cells [2]. The actual composition of lipid bilayers varies widely, enabling the fine tuning of mechanical and chemical properties of organelles for different biological functions [3].

The mechanism behind any form of molecular self-assembly is derived from the

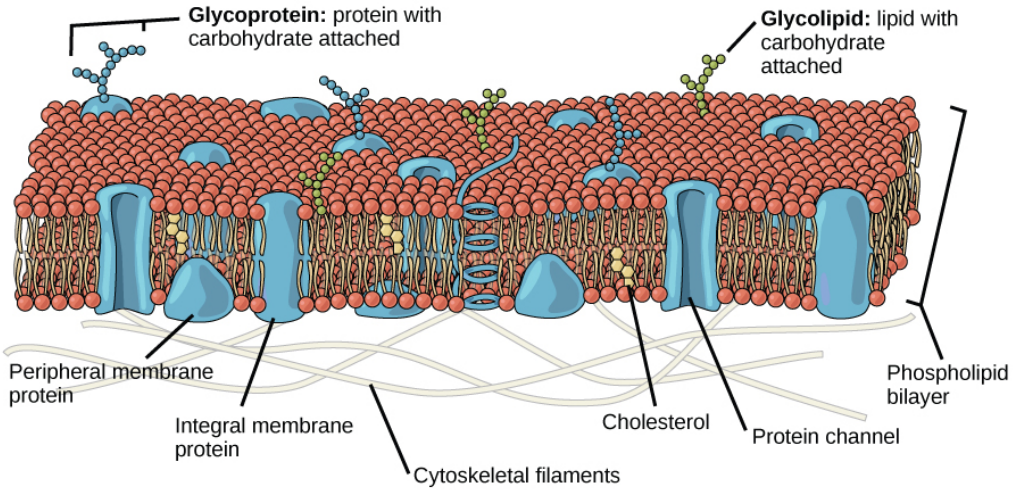

Fig. 1.2: A diagram of the Fluid-Mosaic Membrane model to describe the structure of lipid bilayers, containing phospholipid molecules, cholesterol and various different membrane proteins. (Image adapted from: https://www.boundless.com/biology/textbooks/boundless-biology-textbook/structure-and-function-of-plasma-membranes-5/components-and-structure-64/fluid-mosaic-model-327-11464/)

principal of molecular recognition, that is the specific interaction between two or more molecules through noncovalent interactions. In the case of the plasma membrane, self-assembly is driven by the hydrophobic effect which arises from the amphiphilic nature of lipid molecules.

1.1.2 Surfactants

The lipids which comprise the plasma membrane are in fact a subset of a larger classification group of molecules called "surfactants" (surface active agents) which are amphiphilic in nature, meaning that they contain both hydrophilic and hydrophobic moieties within the same molecule. The result of this chemically contrasting structure is that the hydrophobic tail regions tend to minimise their contact with the surrounding water molecules, whilst the polar head groups prefer to be in contact with the water forming favourable electrostatic interactions. Sodium dodecyl sulphate (SDS) is an example of a surfactant molecule which perfectly illustrates their dual chemical nature, with its nonpolar hydrocarbon chain, negatively charged sul-

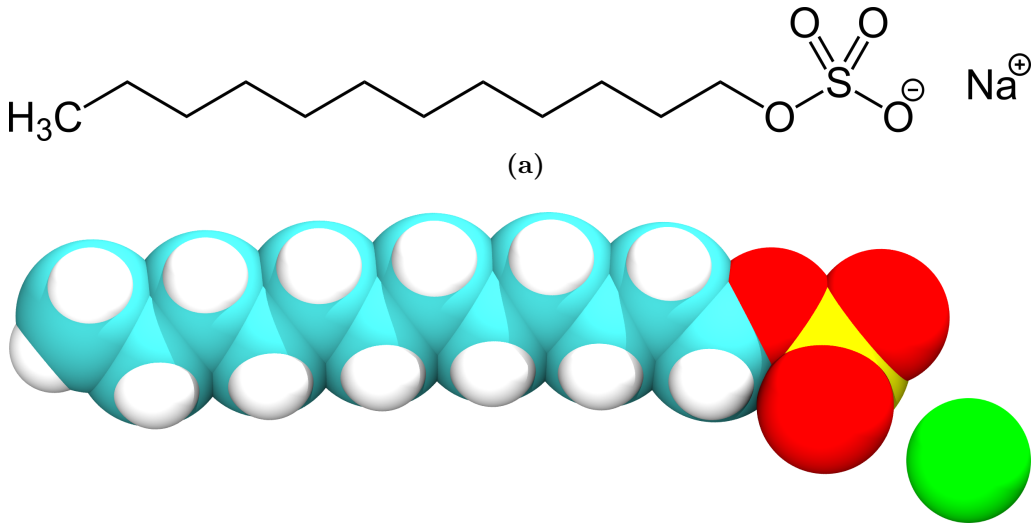

(a)

(b)

Fig. 1.3: a) The chemical structure of sodium dodecyl sulphate, b) A van der Waals depiction of sodium dodecyl sulphate, the head group is shown in red and yellow whereas the tail is depicted in cyan and white. The sodium counterion is depicted in green.

phate head group and positively charged sodium counterion. SDS is one of the most common surfactants and is studied extensively throughout the course of this thesis. There are clearly a vast range of chemistries that fulfill the aforementioned surfactant criteria, and so a large number of chemically different surfactant molecules are possible, which exhibit interesting and diverse physical behaviour upon dissolution in aqueous environments including aggregation, a decrease in the surface tension of water and many more [4].

1.1.2.1 Surface Activity of Liquids

The phenomenon of surface tension in liquids arises due to an imbalance of attractive intermolecular interactions at liquid surfaces. The surface tension of liquids is defined as the interfacial free energy per unit area and can be thought of as a measure of how difficult it is to break the surface film of a liquid. For water, where hydrogen bonding and polar interactions are strong, the surface tension is relatively high (around 72 mN m^{-1}) compared to nonpolar solvents such as hydrocarbons

which experience much weaker attractive interactions, resulting in a lower surface tension (in the range of 20-30 mN m^{-1}). The surface tension of a liquid can be measured experimentally using the Du Noüy ring method [5] in which a ring, often made of platinum, is lifted slowly from the surface of a liquid. The force required to raise the ring from the liquid's surface, F, is measured and the surface tension of the liquid, γ, is calculated from the relation:

$$F = 2\pi(r_i - r_a)\gamma \tag{1.1}$$

where r_i and r_a are the inner and outer diameters of the liquid film pulled respectively.

The origin of surface tension can be understood on a microscopic level by considering the cohesive forces acting between liquids. Atoms which are situated in the bulk liquid phase are subjected to favourable cohesive forces in all directions. However, atoms at the interface of a liquid experience a net force pulling them inwards towards the bulk phase due to an absense of cohesive interactions from the vacuum phase above, which physically corresponds to air. This effect is illustrated in Figure 1.4 and results in the surface atoms being in a higher energy state to those located within the bulk. Because of this, liquids tend to minimise their surface area at interfaces in order to decrease their free energy.

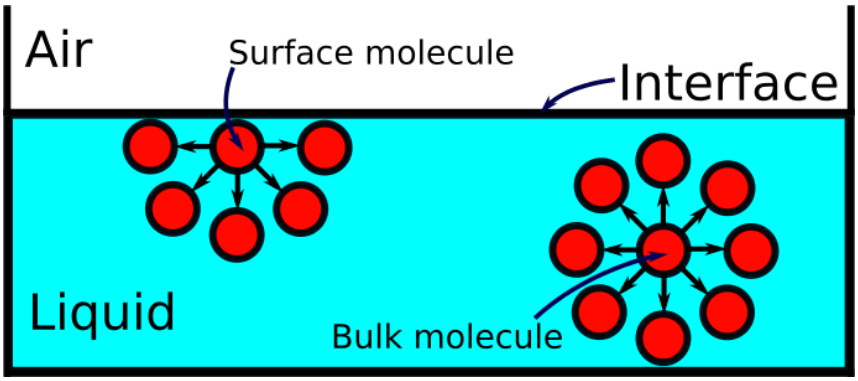

Fig. 1.4: A schematic diagram illustrating the attractive forces between a liquid at the surface and within the bulk phase.

The implications of the high surface tension of water are routinely observed throughout nature. For example, large spherical water droplets are observed on waxy plant leaves such as that in Figure 1.5a. The waxy leaf surface is highly repulsive to water molecules and a spherical droplet is formed to minimise the surface area of the water phase in contact with air and the hydrophobic leaf surface. Moreover, mosquitos use the high surface tension of water to walk across the surface of ponds and lakes without breaking the surface (Figure 1.5b), despite the fact that mosquitos are much denser than water.

(a) **(b)**

Fig. 1.5: a) A photograph of a spherical water droplet on a waxy leaf (Image adapted from http://dartofphysics.ie/blog/nanotechnology-can-help-keep-dart-clean), b) A photograph of a mosquito walking on the surface of a pond or lake. The high surface tension of water is illustrated by the large deformation, without breaking, of the water surface under the mosquito's feet. (Image adapted from https://uk.pinterest.com/haluchlandscape/educate-yourself-mosquito-control/)

When surfactant molecules are immersed in an aqueous solution, the resulting behaviour is dictated by their dual chemical nature. There are two different processes which occur upon dissolution of surfactants in an aqueous solution. The first relates to how the presence of the surfactant affects the surrounding solvent, whilst the second concerns the freedom of motion of the hydrophobic tail region of the molecule. Liquid water is composed of random molecular arrangements of water

molecules that interact with one another through energetically favourable hydrogen bonds. These are enabled by the strong attraction between the positive and negative partial charges on hydrogen and oxygen atoms of neighbouring water molecules, respectively. For the overwhelming majority of cases, the surfactant tails are much larger than the head group and their ability to form hydrogen bonds is effectively zero due to their complete lack of polar interaction sites. Once a surfactant is submerged within an aqueous phase, the hydrogen bond network is initially disrupted and this is energetically unfavourable to the system. The head groups do however possess hydrogen bonding capabilities and form strong electrostatic interactions with surrounding water molecules. At the same time, the nonpolar tails are surrounded by a highly ordered water "cage" which impinges on the internal vibrational degrees of freedom of the hydrocarbon chains. This is responsible for an entropy decrease upon dissolution of a surfactant molecule because the vibrational dynamics of the chain become severely restricted.

The two processes outlined in the preceding paragraphs predict that the preferable configuration for a surfactant molecule coming in contact with an aqueous interface would be for the polar head group to be in contact with the water and the nonpolar tail to be situated away from the solvent in the vacuum region, corresponding to air. Such a configuration would fulfill the favourable criteria of both minimising disruption to the solvent hydrogen bond network, whilst also preserving the entropic contribution from the vibrational degrees of freedom of the hydrocarbon tail. Indeed this prediction turns out to be correct and results in the formation of surfactant monolayers at aqueous interfaces at low concentrations, as shown on the left-hand side region of Figure 1.6.

1.1.2.2 The Critical Micelle Concentration

As the concentration of surfactants is increased from zero, they adsorb to the interface and spread out evenly resulting in a reduction of the interfacial tension (as a

result of the attractive interactions between the interfacial water molecules and the hydrophilic surfactant head groups). At a certain point when the surfactant concentration exceeds a critical value, namely the "critical micelle concentration" (CMC), the interfacial tension will become sufficiently low such that any further increase in concentration will trigger buckling of the monolayer into the bulk phase as this is energetically preferable compared to packing additional molecules into the monolayer. Once this buckling occurs, the surfactant molecules will begin to populate the bulk water phase whilst the concentration on the surface will remain constant, irrespective of how many more surfactants are added to the system.

There are numerous experimental methods to determine the CMC. Surface tensiometry measurements are amongst the most popular of these techniques. Plotting the surface tension as a function of the surfactant concentration will reveal a trend of decreasing surface tension with increasing concentration, up to a point after which the surface tension will plateau and will remain constant even after increasing the surfactant concentration further, as shown schematically in Figure 1.6. The concentration at which the surface tension first reaches the plateau is taken to be the CMC. The CMC can also be determined by measuring other physical properties as a function of surfactant concentration such as electrical conductivity [6], or fluorescence [7] and locating the point of inflection in these curves.

1.1.2.3 Aggregation

At concentrations above the CMC, the surfactants within the bulk aqueous solution will still attempt to minimise the contact between their hydrophobic tails and the surrounding polar solvent. This is achieved by forming a number of different aggregate structures which will be discussed later, such as micelles (of the spherical or cylindrical variety), bilayers, vesicles and lamellar phases as shown in Figure 1.7. At significantly high concentrations, more complex phases may be observed such as cubic, hexagonal and bicontinuous geometries. Surfactant assemblies in bulk solutions

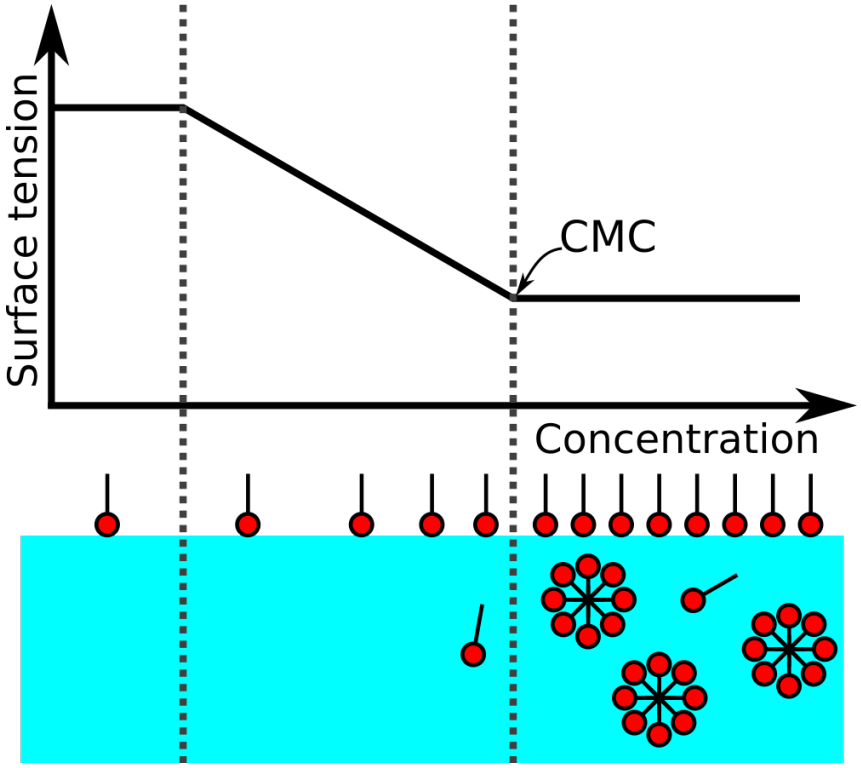

Fig. 1.6: The graph illustrates the relationship between the surface tension of water and the concentration of surfactants, whilst the schematic diagram shows the behaviour of surfactant molecules as a function of their concentration in water, where the colour blue depicts the water in the system and colours red and black depict the surfactant headgroups and tailgroups respectively. The dashed line on the right represents the CMC.

have maintained their crucial importance in science and technology as they are used in various different applications. These include the production of food and personal care products, mineral separation processes, petroleum recovery and environmental remediation [8–12]. Moreover, surfactant micelles have been utilised extensively in pharmaceuticals for their ability to stabilise nucleic acids [13] and to encapsulate drug molecules [14–16]. This thesis focusses on the interaction of drug molecules within surfactant monolayers and micelles.

The aggregation behaviour of surfactants is complex and determined by an interplay of interactions between the surfactant head groups, tail groups, and the solvent as well as geometric factors. There are several semi-quantitative theories that attempt to predict and explain the formation of surfactant aggregates in solu-

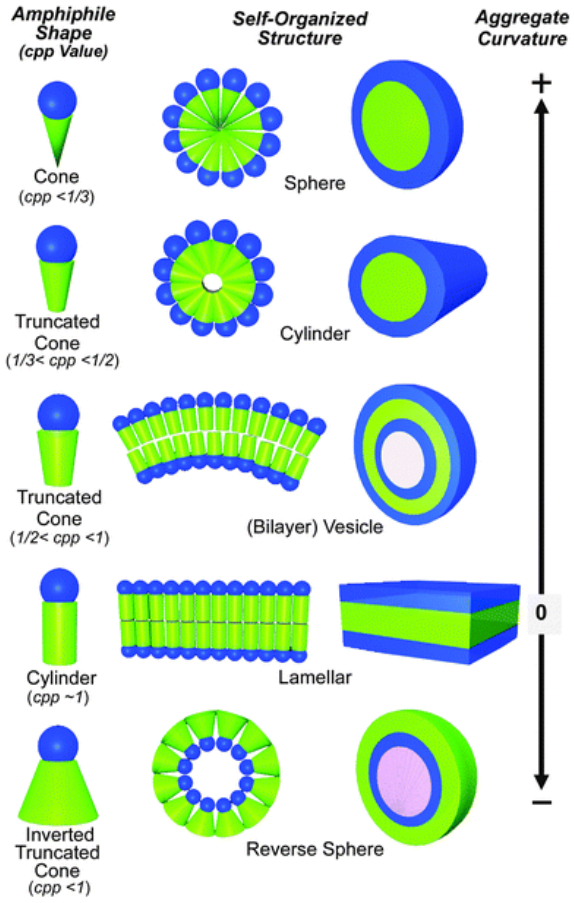

Fig. 1.7: A diagram of the various different self-assembled structures formed by surfactants depending on their geometry. (Image adapted from reference [17])

tion. In 1974, Tanford proposed a thermodynamic explanation of micelle formation using free energy considerations to predict the micelle size and size distribution [18]. When surfactants are dissolved in water the hydrophobic tails provide a free-energy advantage for aggregating but the molecules have more entropy when they remain in an unaggregated state. The molecules can either explore the system volume V like an ideal gas, or they can aggregate resulting in a decrease in their entropy. If there are N surfactant molecules in the system and the total number of molecules within aggregates of size m is N_m then the number of size m aggregates is $A_m = N_m/m$. The ideal gas free-energy (entropic contribution) is given by:

$$F_m^{id} = A_m \left[\ln \left(\frac{A_m v_0}{V} \right) - 1 \right] \tag{1.2}$$

where v_0 denotes the volume of a single surfactant molecule and setting $k_BT \equiv 1$. Now, letting the energy per molecule belonging to aggregates comprised of m monomers be ϵ_m then the total free energy of an aggregate with m monomers is:

$$F_m = N_m\epsilon_m + \frac{N_m}{m}\left[\ln\left(\frac{N_m v_0}{mV}\right) - 1\right] \tag{1.3}$$

As micelles are dynamic structures and can exchange molecules freely, at equilibrium the chemical potential, μ, must be equal in aggregates of all sizes and therefore $\mu = \partial F_m/\partial N_m$ which is a constant and independent of m. Taking the partial derivative of Equation 1.3 with respect to N_m, yields an expression for the chemical potential:

$$\mu = \epsilon_m + \frac{1}{m}\left[\ln\left(\frac{N_m v_0}{mV}\right) - 1\right] + \frac{N_m}{m}\left[\frac{1}{N_m}\right] = \epsilon_m + \frac{1}{m}\ln\left(\frac{N_m v_0}{mV}\right) \tag{1.4}$$

This expression can be rewritten in terms of the volume fraction of aggregates consisting of m monomers, $\phi_m = N_m v_0/V$:

$$\mu = \epsilon_m + \frac{1}{m}\ln\left(\frac{\phi_m}{m}\right) \tag{1.5}$$

Next, μ is eliminated by setting $m = 1$ ($\epsilon_1 + \ln\phi_1 = \mu$):

$$\frac{1}{m}\ln\frac{\phi_m}{m} = \epsilon_1 - \epsilon_m + \ln\phi_1 \Rightarrow \left(\frac{\phi_m}{m}\right)^{\frac{1}{m}} = \phi_1 \exp\left(\epsilon_1 - \epsilon_m\right) \Rightarrow \phi_m = m[\phi_1 \exp\Delta\epsilon_m]^m \tag{1.6}$$

This result provides the concentration of an aggregate composed of m monomers for a given concentration of free monomers, ϕ_1 which can be expressed in terms of the total surfactant concentration ($\phi = \sum_{m=1}^{\infty} m[\phi_1 \exp\Delta\epsilon_m]^m$). A critical value of ϕ_1 is found at the CMC, where ϕ_m switches from a small to a large value. Above the CMC, the predominant micelle size m depends on what type of micelle has the strongest binding energy $\Delta\epsilon_m$, which requires consideration of the surfactants

molecular geometry.

In 1976, merely two years after Tanford's thermodynamic explanation of micelle formation, Israelachvili proposed a method to predict the shape of surfactant aggregates using the "critical packing parameter" [19], cpp which is defined as:

$$\text{cpp} = \frac{V_t}{a_0 l_t} \tag{1.7}$$

where V_t is the volume of the tail region, l_t is the length of the tail region and a_0 denotes the equilibrium cross-sectional area of a surfactant head group at the aggregate surface. The value of cpp can be used to define criteria of formation for aggregates with different shapes by predicting the curvature of an aggregate interface. For example consider a spherical micelle with aggregation number n. The volume of the core is given by $V_{\text{core}} = nV_t = 4\pi R^3/3$ and the area of the micelle surface is given by $A = na_0 = 4\pi R^2$. Solving these equations for R in terms of V_t and a_0, and then constraining $R \leq l_t$ affords the condition $0 < \text{cpp} \leq 1/3$ for the formation of a spherical micelle. Using similar arguments one finds that the condition for the formation of cylindrical micelles is $1/3 < \text{cpp} \leq 1/2$ and for a bilayer: $1/2 < \text{cpp} \leq 1$. Figure 1.7 provides a visual summary of the various aggregate structures formed by surfactants with different geometries and the packing parameter criteria for each. Essentially, the packing parameter describes the shape of a molecule of a particular surfactant species and then predicts the geometry of the aggregates formed. For example, cone shaped molecules assemble into spherical micelles, whilst cylindrical surfactants will more likely form bilayer or lamellar geometries. The physical manifestation of these different surfactant molecular geometries originates predominantly from the structure of their hydrophobic tails. For example, SDS has a single alkyl chain and a sulphate head group resulting in a cone like shape, whereas lipid molecules such as dipalmitoylphosphatidylcholine (DPPC) generally have two hydrophobic tails resulting in a cylindrical shape. Inverted truncated cone shapes may occur when there

is an unsaturated double bond present in at least one of the lipid tails, producing a kink in the acyl chain(s).

More rigorous approaches to estimate aggregate structures include experimental scattering techniques such as small angle x-ray scattering (SAXS) [20] and small angle neutron scattering (SANS) [21]. Alternatively, computational simulation techniques can also be employed to provide atomistic structural detail about surfactant aggregates. This thesis makes use of such techniques, which are explained thoroughly in Chapter 2.

1.2 Motivation

As was alluded to earlier, surfactants have many uses in society in diverse application areas. This thesis focusses specifically on their role within oral medications in the pharmaceutical industry. For patients, oral medications are extremely popular due to their ease of administration and noninvasiveness in comparison to other drug delivery methods [22–25]. From the perspective of pharmaceutical firms, oral drug formulations are heavily invested in and generally preferred because of their relative ease and low cost of manufacture, along with the high demand from patients and physicians.

For a drug molecule in an oral formulation to produce a desired effect in the body, it must first be released from its pharmaceutical dosage form and absorbed into the bloodstream in order to become available at its intended site of action. The degree to which this occurs is known as the bioavailability of the drug, and the 'site of action' is taken to be the systemic circulation [26]. The bioavailability of orally administered drugs is strongly influenced by their rate of absorption across the gastrointestinal (GI) tract [27]. In turn, the amount of a drug absorbed across the GI membrane is determined by its aqueous solubility, therefore a poor aqueous solubility generally suggests a poor bioavailability. It follows that a drug molecule

must have sufficient aqueous solubility to be considered as a likely candidate for formulation into an oral medication, however it is estimated that over 40 % of newly discovered drugs have poor aqueous solubility [28, 29]. The stark reality of this is that a large proportion of these chemical entities may never reach patients who desperately require their therapeutic effects. To combat this, a wealth of formulation and drug development techniques have emerged in recent years to overcome the problem of poor aqueous solubility. Many of these techniques involve the encapsulation of the poorly soluble drug compound within self-assembled nanostructures, a process which is energetically favourable to the system and enhances the apparent aqueous solubility of the drug compound. There is an abundance of research into biodegradable polymeric nanoparticles due to their controlled release and minimal toxicity [30, 31], as well as the use of surfactant aggregate systems [14–16] which are the primary focus of this thesis.

The preferred location of the encapsulated drug species within an aggregate is vital knowledge for the rational design of micelle-drug formulations because the number of drug molecules that can be loaded into a micelle will be determined by the effective volume of their preferred location. Figure 1.8 shows estimations of the main sites of encapsulation within micelles including: 1) the hydrophobic core, 2) the micelle/water interface, and 3) under the head groups in the micelle palisade layer. Surfactant aggregate structures are difficult to study experimentally due to their nanometre length scales. To interpret neutron scattering experiments, assumptions must be made regarding the position of the encapsulated solute prior to fitting the experimental data. Simulation and modelling techniques are able to provide invaluable information about the location of the encapsulated drug species within an aggregate which is of great relevance to such experiments. This requires a rigorous microscopic characterisation of the aggregate shape and interface, which remain prominent themes throughout this thesis.

The purpose of this thesis is to develop an understanding of how the chemical

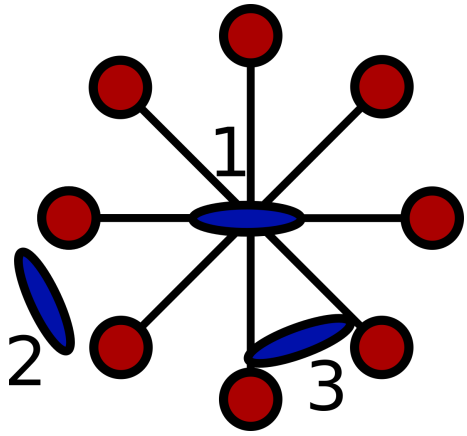

Fig. 1.8: A diagram depicting the different locations of a solute encapsulated within an ionic surfactant micelle: 1) the hydrophobic core, 2) the micelle/water interface, 3) under the head groups in the micelle palisade layer. The drug molecules and surfactant head groups are depicted in blue and red respectively.

composition of a surfactant species, the counterion species and the drug compound affects the relative ability for the drug to be encapsulated within a surfactant aggregate and therefore be a potential formulation for oral drug delivery. This work is inspired, in part, by a recent study performed by Saaka [32] of the steroidal drugs: testosterone (T), testosterone propionate (TP) and testosterone enanthate (TE) which are all currently administered to patients undergoing testosterone replacement therapy, despite their poor water solubility. This thesis aims not to develop a testosterone-based medication specifically, but to build an understanding of how the chemical structure of the surfactants, counterions and drug molecules themselves affect the encapsulation process with the intent of designining more efficient oral medications in the future. In this sense, T, TP and TE are treated as model drug molecules. Saaka showed that the number of drug molecules that can be encapsulated within these aggregates is affected by changing the counterion species as well as the chemical structure of the drug molecule.

In this thesis, atomistic molecular simulations are applied to these systems to gain a detailed description of the molecular scale interactions which govern this behaviour. In reality drug loaded surfactant micelles are the nanostructures ad-

ministered to patients and therefore the most realistic systems to study. However, due to the challenges of simulating surfactant micelles (resulting from their large system sizes), surfactant monolayers are studied in conjunction with micelles and the interactions between drug molecules and surfactant monolayers is approximated to be equivalent to those between drug molecules and micelles. This is an entirely reasonable approximation given that monolayers and micelles coexist in dynamic equilibrium and monomers in both structures have the same chemical potential, thus exchanging freely between these two structures.

First, the interfacial properties of surfactant monolayers are studied in the presence of different counterions but without the presence of drug compounds. Then the interaction process of three model drugs within surfactant monolayers is investigated using different computational methods. Finally, the encapsulation process of TP within an SDS micelle is modelled, as this combination of surfactant and drug species was found to be the most successful formulation [32].

1.3 Overview of Thesis

The remainder of this thesis is organised as follows. In Chapter 2, the scientific methods used throughout this work are explained in detail. Next the surfactant monolayer studies are presented: Chapter 3 outlines the simulation protocol and analysis methods used for simulating surfactant monolayers. In Chapter 4, results are presented from dodecyl sulphate monolayers with different counterion species and the structural and interfacial properties are compared. Building upon these result, Chapter 5 presents the results from a study of the interaction of testosterone-based compounds within surfactant monolayers and Chapter 6 reports the results from metadynamics calculations used to estimate the free energy of permeation of the different drugs within SDS monolayers. Following this, surfactant micelles are investigated. In Chapter 7, the simulation protocol and analysis of surfactant mi-

celles is described and the results from these simulations are presented in Chapter 8. Finally, the overall findings are summarised and future prospects are discussed in Chapter 9.

Chapter 2

Methods

2.1 Classical Molecular Dynamics Simulations

Molecular dynamics (MD) is a computational technique commonly used to study both the time-dependent and equilibrium behaviour of molecular systems with atomistic detail. The first example of a molecular dynamics simulation dates back to the late 1950's and was implemented by Alder and Wainwright [33], modelling atoms as hard spheres interacting with square well potentials. Despite this rather simplified model, many important insights regarding the behaviour of liquids emerged from their studies concerning phase transitions at different volume fractions. Later in 1964, Rahman carried out the first MD simulation using a realistic potential for liquid argon [34] and obtained results for the pair correlation function and the self-diffusion coefficient which were in close agreement with experimental data. Then in 1974, Rahman and Stillinger simulated liquid water [35] which was the first reported MD simulation of a realistic system. In the literature today, one routinely finds MD simulations studying the complex phase behaviour of large lipid systems [36], fully solvated proteins [37] and protein-DNA complexes [38] to name but a few. MD simulations provide a microscopic insight into molecular systems, information which is hardly accessible by experiments. The trajectories generated from these

simulations can be visualised in three dimensions which aids the understanding of complex molecular mechanisms such as protein folding [39] and self-assembly [40]. MD simulations are vastly considered as a method of research in their own right, in addition to providing a useful compliment to experimental work and are now routinely used to investigate the structure, dynamics and thermodynamics of matter. In particular, there is a large abundance of research investigating biological molecules such as proteins and peptides [41].

The idea behind MD is relatively simple: the positions and velocities of the particles which compose the system are obtained as a function of time by integrating Newton's equations of motion. In actuality, a thorough description of the interaction between atoms requires quantum mechanical considerations. Such interactions are included in *ab initio* MD simulations but are incredibly expensive to compute which restricts the length and time scales that can be modelled. In classical MD, the underlying assumption is that the atomic nuclei obey the laws of classical mechanics and this turns out to be an entirely reasonable assumption for a wide range of materials. Although this assumption limits the information that can be extracted from calculations, it also permits simulations on large spatial and temporal scales which would be simply unfeasible using *ab initio* methods such as density functional theory (DFT) [42, 43]. Using classical MD, ensemble averages can be monitored, the phase space of the system can be explored and the system dynamics can be probed.

2.1.1 Force Field

The force field is an integral part of molecular simulation, that is the set of empirical equations and parameters which govern the physical interactions within the system. The first force fields were parametrised to reproduce structural properties and vibrational spectra [44]. Later, in the 1980's Amber, CHARMM and OPLS developed force fields which used united atom approaches for hydrogen atoms bound

to carbons. Most parameters were developed and tested on gas-phase simulations and partial charges were derived from quantum mechanical calculations by fitting partial charges to the electrostatic potential [45]. In the 1990's, both AMBER and CHARMM force fields were further developed to take liquid phase properties directly into account in the parametrisation such as densities and heats of vaporisation [46]. A major update of the AMBER force field was published in 1995 and is still widely used [47] and CHARMM has seen numerous updates since the 1990's [48]. The total potential energy of a molecular system is given by the sum of the bonded, U_{bonded}, and non-bonded, $U_{\text{non-bonded}}$ contributions:

$$U_{\text{total}} = U_{\text{bonded}} + U_{\text{non-bonded}} \tag{2.1}$$

The CHARMM force field [48] has been used to describe the interactions in all of the simulations presented within this thesis. For this reason, the relevant functional forms for U_{bonded} and $U_{\text{non-bonded}}$ in the CHARMM force field are discussed in the following section. It should be noted however that other functional forms for these interactions do exist and are used in other force fields.

2.1.1.1 Non-bonded Interactions

The non-bonded term, $U_{\text{non-bonded}}$, can be represented using the functional form of a Lennard-Jones potential to describe dispersion interactions with the addition of a Coulombic term to model electrostatic interactions, where applicable. The Lennard Jones potential, also commonly referred to as the "12-6" potential, is chosen because the functional form can be evaluated efficiently whilst also giving rise to a potential which is attractive at mid-long distances but repulsive at short distances (see Figure 2.1), thus providing a physical description of van der Waals interactions.

The full non-bonded potential is therefore expressed as:

$$U_{\text{non-bonded}} = u^{LJ}(r_{ij}) + u^{\text{Coul}}(r_{ij}) = 4\epsilon_{ij}\left[\left(\frac{\sigma_{ij}}{r_{ij}}\right)^{12} - \left(\frac{\sigma_{ij}}{r_{ij}}\right)^{6}\right] + \frac{q_1 q_2}{4\pi\epsilon_0 r_{ij}} \tag{2.2}$$

where ϵ_{ij} and σ_{ij} denote the characteristic interaction energy and distance respectively for particles i and j. Specifically, σ_{ij} is the value of r_{ij} where the Lennard-Jones function intercepts the x-axis (shown in Figure 2.1). In the CHARMM force field, one value for σ and ϵ is provided per atom type and inter-type interactions are calculated using the arithmetic mean of σ ($\sigma_{\text{ij}} = (\sigma_{\text{i}} + \sigma_{\text{j}})/2$) and the geometric mean of the well-depths ($\epsilon_{\text{ij}} = \sqrt{\epsilon_{\text{i}}\epsilon_{\text{j}}}$). In the Coulombic term, q_i and q_j are the charges on particles i and j respectively, and ϵ_0 denotes the permittivity of free space. It is common to use a shifted potential which ensures that the function tends smoothly to zero at the desired cutoff distance to prevent discontinuities in both the forces and the energy of the system. This is achieved by using a slightly modified version of Equation 2.2 which affects $U_{\text{non-bonded}}$ like so:

$$U_{\text{non-bonded}}(r_{ij}) = \begin{cases} u^{\text{LJ}}(r_{ij}) + u^{\text{Coul}}(r_{ij}), & r < r_{\text{in}} \\ S(r_{ij})u^{\text{LJ}}(r_{ij}) + u^{\text{Coul}}(r_{ij}), & r_{\text{in}} < r < r_{\text{out}} \\ 0, & r > r_{\text{out}} \end{cases} \tag{2.3}$$

where r_{in} and r_{out} are the inner and outer cutoff radii respectively which are used in the switching function:

$$S(r_{ij}) = \frac{[r_{\text{out}}^2 - r^2]^2[r_{\text{out}}^2 + 2r^2 - 3r_{\text{in}}^2]}{[r_{\text{out}}^2 - r_{\text{in}}^2]^3} \tag{2.4}$$

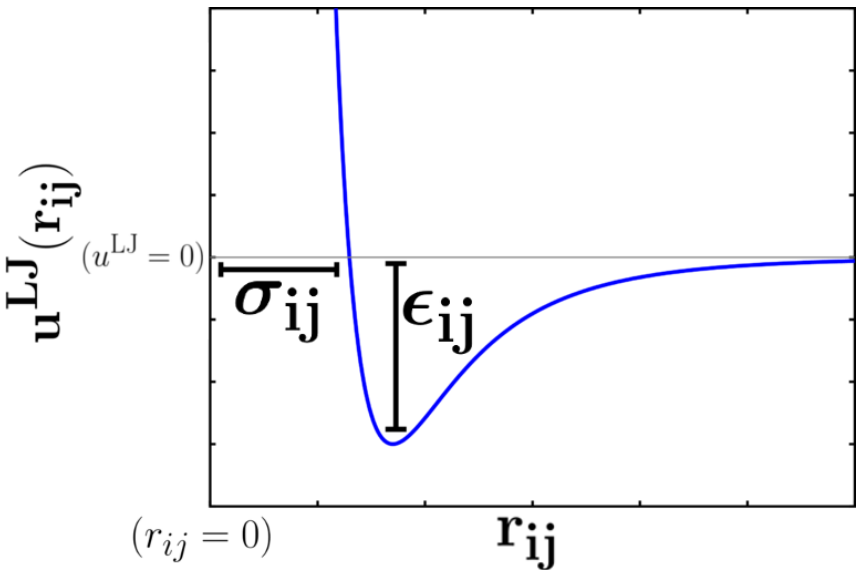

Fig. 2.1: A graph showing functional form of the Lennard-Jones potential, $u^{\mathrm{LJ}}(r_{ij})$, used to describe van der Waals interactions in the CHARMM force field. The parameters σ_{ij} and ϵ_{ij} are labelled.

Both the Lennard Jones and Coulombic interactions depend on one variable, the module $|r_{ij}|$ and are therefore spherically symmetric. The full contribution to the potential energy of the system from the non-bonded interactions is given by the summation over all pairs of atoms for these two interactions. It is common for van der Waals interactions to be truncated at 2.5σ ($\sim$ 10-12 Å), where the Lennard Jones potential is approximately $1/60^{\mathrm{th}}$ of its minimum value, ϵ. The electrostatic interactions however require a more careful treatment of the long-range interactions due to the $1/r$ decay of the Coulomb function. One cannot simply truncate this term like the procedure performed for Lennard Jones interactions because long range electrostatics are known to have a significant effect on structure and dynamics. A common method of dealing with these long range electrostatic interactions is by using the Particle-Particle-Particle Mesh (PPPM)[49] method which is a Fourier-based Ewald summation over the charges in periodic box images. The accurate evaluation of long-range electrostatic interactions is a necessary, yet computationally expensive part of MD simulations. The PPPM solver scales as $N \log N$ where N is the number of atoms in the system. The traditional Ewald sum scales as $N^{3/2}$, so

the PPPM method is almost always the preferable choice over the traditional Ewald summation with respect to CPU time as a result of the fast Fourier transforms implemented.

2.1.1.2 Bonded Interactions

With regard to the bonded interactions, there are contributions to the potential energy from bond stretching, angle deformation, torsional angles and in some instances, improper angles (see Figure 2.2 for illustrations). The total bonded contributions to the potential energy are given by the following expression:

$$\begin{aligned} U_{\text{bonded}} = \sum_{\text{bonds}} \frac{k_b}{2}(l - l_0)^2 + \sum_{\text{angles}} \frac{k_\theta}{2}(\theta - \theta_0)^2 \\ + \sum_{\text{dihedrals}} \frac{k_\phi}{2}(1 + \cos(n\phi - \phi_0)) + \sum_{\text{impropers}} \frac{k_\psi}{2}(\psi - \psi_0)^2 \end{aligned} \tag{2.5}$$

The bond stretching is usually represented by a harmonic term such as the first term in Equation 2.5 which is valid for small displacements from the equilibrium bond length, l_0. The force constant, k_b, is usually large indicating that a large amount of energy is required to stretch or compress a chemical bond by any significant length. The second term in Equation 2.5 represents the potential energy associated with deformation of valence angles from their equilibrium value, θ_0. The angle deformation force constant, k_θ, is typically lower than that of bond stretching because it takes less energy for a valence angle to deviate from its equilibrium value. Historically, bond and angle parameters were taken from small-molecule crystallography and vibrational spectroscopy. These days, quantum mechanical methods are employed on small compounds to provide more accurate values for bond and angle parameters. The third term in Equation 2.5 represents the torsional contribution and quantifies the potential energy associated with rotations around each dihedral angle. These torsional terms include atoms which are separated by three bonds. The force constant for dihedral angles, ϕ_0, is usually significantly less than both bond stretching

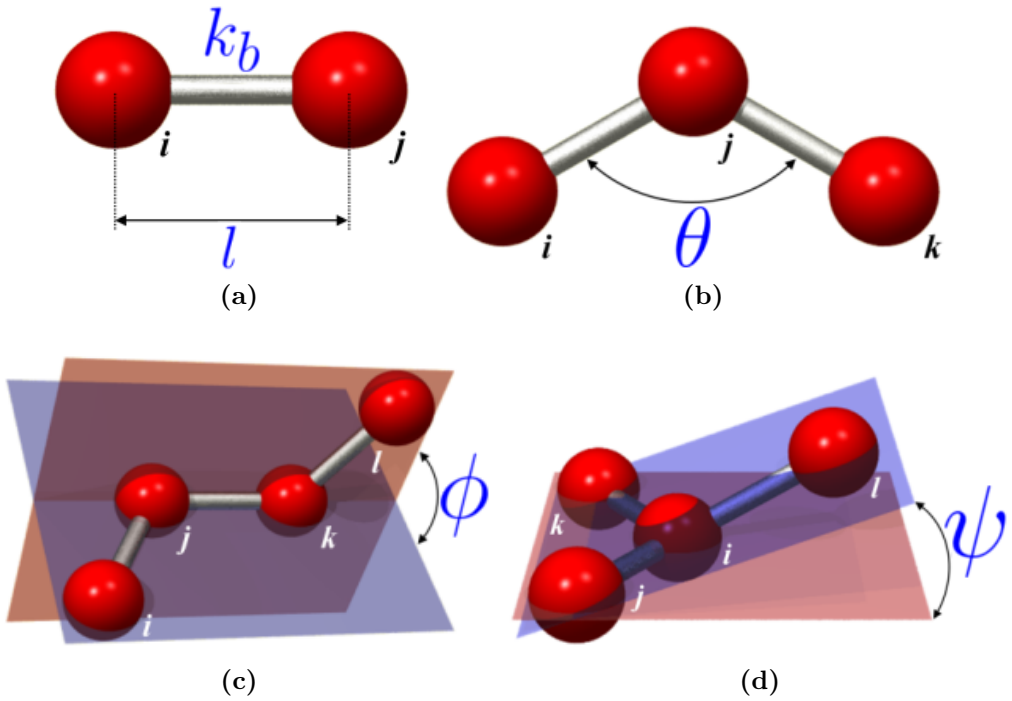

Fig. 2.2: Schematic diagrams illustrating the various contributions to the bonded potential energy: a) bonds, b) angles, c) dihedrals and d) improper angles (images adapted from http://cbio.bmt.tue.nl/pumma/index.php/Theory/Potentials).

and angle bending [50]. Here, n corresponds to the number of minima in the energy landscape, often referred to as "multiplicity" and ϕ_0 is the phase factor which determines the location of the minima in the potential. This functional form is symmetric with the same minimum and maximum in the torsional energy landscape. Whilst spectroscopy can provide relative populations of trans and gauche conformations for simple molecules and hence the free energy difference between these states can be derived, quantum mechanical calculations are more frequently used as they provide information about the rest of the potential. Finally, improper angles are imposed on some molecules to preserve geometry or chirality of atoms in a molecule, for example to maintain the planarity of aromatic carbon rings in testosterone molecules. The definition of an improper angle is shown in Figure 2.2d as the angle between the vector formed between atoms i and l, and the plane in which atoms i, j and k are incident. The improper angle contribution to the potential energy adopts a

harmonic functional form for convenience, as shown in the last term in Equation 2.5. Here, k_ψ and ψ_0 are the force constant and equilibrium improper angle respectively.

2.1.2 Initialisation

The first stage of conducting any MD simulation is the assignment of the initial coordinates of the system. The initial coordinates should be chosen to somewhat resemble the desired structure which is to be modelled. For example, if simulating a surfactant micelle then the coordinates should be chosen so that the surfactant tails form a spherical hydrophobic core, and the head groups are in contact with the surrounding water molecules. It is especially important to build configurations which do not result in significant overlapping of atoms which will result in extremely high energy states. One way to achieve this for simple systems such as gases is to place the atoms on a cubic lattice. For more complex molecular geometries, there are a number of different software packages to generate configurations such as Packmol [51] which is commonly used to build structures such as bilayers, micelles and vesicles and has been used extensively throughout this thesis to build initial configurations for the monolayer and micelle simulations.

2.1.3 Energy Minimisation

Once an initial set of coordinates has been generated, energy minimisation is performed and the system is brought to a minimum in the potential energy landscape as determined by the force field. There are numerous different methods to accomplish this, all of which are able to steer the system towards the closest local potential energy minimum but none are able to sample the full conformational space. Perhaps the simplest of these is the steepest descent algorithm, which is the energy minimisation algorithm used for all of the simulations reported within this thesis. The steepest descent algorithm exploits the first derivative of the potential energy

surface to find the local minimum. An iterative process: $\mathbf{r}(k) = \mathbf{r}(k-1) + \lambda(k)\mathbf{F}(k)$ is applied where λ is the "learning rate" and $\mathbf{F}(k)$ is the effective force vector which consists of the forces derived from the gradient of the potential energy and is applied to the atoms at each iteration step. The value of $\lambda(k)$ can be adapted at each iteration to ensure that the energy minimum is not overshot by following the curvature of the potential surface [52].

2.1.4 Assigning Initial Velocities

After the potential energy of the system has been minimised, the next step is to set the initial atomic velocities. This is accomplished by randomly assigning each velocity component of every particle a value taken from a Maxwell-Boltzmann distribution in the range [-0.5:0.5]. The subsequent velocity components are then shifted such that the total momentum of the system is zero and then the velocities are scaled so that the mean kinetic energy is equal to the desired value. In thermal equilibrium, the equipartition theorem should hold: $< v_\alpha^2 >= k_B T/m$, where v_α is the α^{th} velocity component of a given particle. From this, the instantaneous temperature at time t, $T(t)$ is given by:

$$k_B T(t) \equiv \sum_{i=1}^{N} \frac{m v_{\alpha,i}^2(t)}{N_f} \tag{2.6}$$

The instantaneous temperature $T(t)$ is adjusted to match the desired temperature by scaling all velocities by the factor $(T/T(t))^{1/2}$. At this point, the system is in a local minimum in the potential energy landscape and has a set of atomic velocities which produce the desired system temperature. At this point, the system dynamics are almost ready to be simulated, but first one must choose a thermodynamic ensemble with which the simulation will be performed.

2.1.5 The Velocity-Verlet Algorithm

Once the system has been built and minimised, dynamics can then be simulated. As was discussed above in Section 2.1.1, the potential energy of the system is described by a force field composed of simple mathematical functions which represent the interactions between different atom types in different chemical environments. This simplified molecular description allows for the quick integration of Newton's equations of motion for point-like particles, the interactions for which are pair-wise additive. This assumption makes use of the Born-Oppenheimer approximation [53] in which electronic and nuclear motions of atoms are decoupled due to the inherently large difference in their time scales, nuclear being much slower. MD integrators update the positions and velocities of the nuclei whilst the electronic behaviour is accounted for implicitly within the simple potential functions. Newton's equation of motion for a system comprised of N particles interacting via a potential $U(\mathbf{r}_1, \mathbf{r}_2, ..., \mathbf{r}_N)$, can be formulated as the second order differential equation:

$$\mathbf{f}_i = m_i \ddot{\mathbf{r}}_i = -\frac{\partial}{\partial \mathbf{r}_i} U(\mathbf{r}_1, \mathbf{r}_2, ..., \mathbf{r}_N) \tag{2.7}$$

where m_i is the mass of particle i and $\mathbf{r}_i$ its position vector. Expressions for the velocity and momentum of particle i are obtained from differentiating the position with respect to time, where $\mathbf{v}_i = \dot{\mathbf{r}}_i$ and $\mathbf{p}_i = m_i \ddot{\mathbf{r}}_i$ represent the velocity and momentum of particle i respectively. Thus, in three dimensions either a set of $3N$ second-order differential equations or an equivalent set of $6N$ first-order differential equations must be solved. This set of differential equations is transformed into difference equations in order for numerical integration to be performed.

An integrator is defined by the chosen form and solution method of the difference equations. There are several requirements of such an integrator. First, in the limit of the step size $\delta t \to 0$, it should reproduce the original differential equations. Another important requirement is that the numerical solution should be close to

the actual solution, which for longer time intervals also requires it to be stable. The algorithm should be time-reversible, consistent with Newton's equations. Additionally, the integration algorithm should also be symplectic which means that in the transformation from a given time step to the successive time step, the volume in phase space should remain unchanged as should the total energy of the system. Another important characteristic of an integrator is efficiency, it is in one's interest to use the largest time-step possible, whilst ensuring numerical stability. Evaluating forces is computationally expensive and so using a larger time-step will result in a longer trajectory per unit of real simulation time. This allows larger sampling of phase space and thus a more accurate data set. One integration scheme which satisfies all of the requirements listed above is the *velocity Verlet* algorithm, which is a modification of the Verlet algorithm introduced by Loup Verlet in 1967 [54]. Although other integration schemes exist, such as the leapfrog algorithm and position Verlet algorithms, the *velocity Verlet* algorithm is used within all of the MD simulations reported within this thesis.

The equations of motion in MD cannot be solved analytically because the forces change with every coordinate configuration and therefore must be solved numerically using a finite integration time step, δt. One operates under the assumption that the forces can be considered to be fixed within the duration of δt. The *velocity Verlet* algorithm yields positions, velocities and accelerations at time $t + \delta t$:

$$\mathbf{r}_i\left(t+\delta t\right) = \mathbf{r}_i(t) + \mathbf{v}_i\left(t\right)\delta t + \frac{1}{2}\mathbf{a}_i(t)\delta t^2 \tag{2.8}$$

$$\mathbf{v}_i\left(t+\frac{\delta t}{2}\right) = \mathbf{v}_i(t) + \mathbf{a}_i(t)\frac{\delta t}{2} \tag{2.9}$$

$$\mathbf{a}_i\left(t+\delta t\right) = -\frac{1}{m_i}\nabla V\left(r\left(t+\delta t\right)\right) \tag{2.10}$$

$$\mathbf{v}_i\left(t+\delta t\right) = \mathbf{v}_i\left(t+\frac{\delta t}{2}\right) + \mathbf{a}_i(t+\delta t)\frac{\delta t}{2} \tag{2.11}$$

The *velocity Verlet* algorithm can be summarised like so:

1. First, calculate the new positions of the atoms at time $t + \delta t$ and update the atomic coordinates.

2. Next, calculate the velocities of atoms in the middle of the time step (at $\delta t/2$).

3. Calculate accelerations of the atoms at time $t + \delta t$ by taking the gradient of the force field.

4. Calculate the new velocities of atoms in the system (after δt).

Repeating the steps above generates a time trajectory for the evolution of the molecular system under investigation. The behaviour of the system during this time evolution is determined by the details in the force field which is used to calculate the forces acting on each atom in the system. The choice of the finite integration time step, δt, is an important detail and one not to be overlooked [55]. The smaller the value of δt, the more accurate the resulting simulation dynamics will be. Conversely, using a larger value of δt is to one's benefit, allowing the system to explore phase space at a faster rate. If δt is too large however, resulting in one atom being moved within very close proximity to another atom, then this will cause large forces which will lead to extremely large changes in velocity and position in the next integration time step. This will typically result in a cascade of errors causing the system to "blow up". To ensure well behaved dynamics, δt should be in the order of the fastest time scale in the system: the bond stretching involving hydrogen atoms. The period of oscillation of a C-H chemical bond is ~ 11 fs and therefore a time step of 1 fs is chosen to ensure several data points per C-H bond vibration. The time step can be increased by using a constraint algorithm such as SHAKE [56] which fixes the high frequency hydrogen containing bond stretching and angle rotations in the system by using constraint forces formulated from Lagrange multipliers. This permits the use of a larger time step and therefore increases the efficiency of the simulation enabling longer simulation trajectories to be obtained per unit of real time running the sim-

ulation. The SHAKE algorithm is used to constrain the high frequency degrees of freedom in the simulations reported within this thesis.

2.1.6 Pressure and Temperature Control

Using the *velocity Verlet* algorithm described in Section 2.1.5, the simulation evolves in the microcanonical (constant NVE) ensemble where the total energy of the system is conserved. This ensemble corresponds to an isolated state which is not particularly applicable to describing situations in a laboratory or *in vivo*. It is often more instructive to run simulations in other ensembles such as constant NVT or NPT, especially if comparisons are to be drawn between the simulation and experimental results which were obtained from an ensemble other than the microcanonical. In the NVT ensemble, the system is kept in thermal equilibrium with a heat bath while the number of particles N and total volume V are constant extensive quantities, the temperature is intensive but can be determined from the kinetic energy, obtained from the equipartition theorem:

$$< K >_{\mathrm{NVT}} = \frac{3}{2} n k_{\mathrm{B}} T \tag{2.12}$$

where angle brackets denote a time average, k_{B} is the Boltzmann constant and n is the number of degrees of freedom. The most basic way of regulating temperature in MD is to use a velocity-rescale thermostat. This is applied by periodically rescaling particle velocities around a Boltzmann distribution centred at the desired temperature [57]. This method however does not produce a canonical ensemble as it does not capture the correct energy fluctuations in the system and is therefore unsuitable for production runs, nevertheless velocity-rescale thermostats are commonly used in the equilibration stage of simulations due to their extreme efficiency.

Stochastic thermostats are often used to regulate temperature in the NVT ensemble. Perhaps the most common stochastic thermostat is the Langevin, which

regulates temperature by applying both a frictional term and a random force to the equations of motion of the system. The average magnitude of the random forces and the friction are related in a way that guarantees that the "fluctuation-dissipation" theorem is obeyed, thereby producing NVT statistics. In this formalism, the equations of motion are modified like so:

$$m_i \frac{d^2\mathbf{r}_i(t)}{dt^2} = \mathbf{f}_i(t)\gamma_i m_i \frac{d\mathbf{r}_i(t)}{dt} - \xi_i \tag{2.13}$$

where f_i is the force acting on atom i due to the interaction potential, γ_i is a friction coefficient, and ξ_i is a random force exerted on atom i with dispersion σ_i. This random force is coupled to the friction coefficient through the relation: $\sigma_i^2 = 2m_i\gamma_i k_B T/\delta t$ and is uncorrelated in time and across particles. The Langevin thermostat is advantageous in that it permits the use of a larger time step than in NVE simulations, however a drawback of using the Langevin thermostat is that momentum transfer is destroyed, therefore it is unadvisable to use Langevin to study dynamic system properties such as diffusion.

Another example of a stochastic thermostat was proposed by Andersen [58] whereby the system is coupled to a heat bath that imposes the desired temperature. Stochastic impulsive forces act upon randomly selected particles and this represents the coupling of the system to a heat bath. The system evolves according to the usual Newton's equations of motion in between collisions. As a result of these stochastic collisions, all accessible constant-energy shells are visited according to their Boltzmann weight throughout the simulation. The strength of coupling to the heat bath must be specified through the collision frequency ν (or collision time $\tau = 1/\nu$) and should be chosen such that collisions occur less than every time step. When a particle is selected to undergo a collision with the heat bath, its velocity is randomly reassigned from a Maxwell-Boltzmann distribution at the desired temperature which turns the simulation into a Markov process, i.e the dynamics are

non-deterministic. Over an infinitely long simulation trajectory, this will produce a canonical distribution of kinetic and potential energies as well as the microstates of different system configurations. The true molecular kinetics of the system are once again not preserved and so the Andersen thermostat should not be used to study dynamic properties of the system.

The Nosé-Hoover thermostat [59] is an example of a thermostat which does indeed preserve the true molecular kinetics of the system by using an extended Lagrangian approach to maintaining constant temperature. This is achieved by making a modification to the *velocity Verlet* algorithm, specifically by the addition of a fictitious dynamical variable, which corresponds physically to a friction term, ξ, which either accelerates or decelerates particles until the desired temperature is reached. Under this scheme, the equations of motion in three dimensions are:

$$m_i \frac{d^2\mathbf{r}_i(t)}{dt^2} = \mathbf{f}_i(t) - \xi m_i \mathbf{v}_i(t) \tag{2.14}$$

$$\frac{d\xi(t)}{dt} = \frac{1}{Q}\left[\sum_{i=1}^{N} m_i \frac{\mathbf{v}_i(t)^2}{2} - \frac{3N+1}{2} k_B T\right] \tag{2.15}$$

where Q is a parameter which represents the "mass" of the heat bath and T denotes the desired temperature. It can be demonstrated that in the steady state, $\left\langle \frac{d\xi(t)}{dt} \right\rangle = 0$, the kinetic energy of the system is given by $\frac{1}{2}(3N+1)k_B T$ where the extra degree of freedom is due to the fictitious variable ξ. In this formulation, the system temperature is not fixed, rather it tends towards the target, T. These equations of motion which correspond to the implementation of the Nosé-Hoover thermostat are

incorporated into MD by modifying the velocity Verlet algorithm like so:

$$\mathbf{r}_i\left(t+\delta t\right) = \mathbf{r}_i(t) + \mathbf{v}_i(t)\delta t + \left(\frac{\mathbf{f}_i(t)}{m_i} - \xi(t)\mathbf{v}_i(t)\right)\frac{\delta t^2}{2} \tag{2.16}$$

$$\mathbf{v}_i\left(t+\frac{\delta t}{2}\right) = \mathbf{v}_i(t) + \frac{\delta t}{2}\left(\frac{\mathbf{f}_i(t)}{m_i} - \xi(t)\mathbf{v}_i(t)\right) \tag{2.17}$$

$$\mathbf{f}_i\left(t+\delta t\right) = \mathbf{f}_i(\mathbf{r}_i(t+\delta t)) \tag{2.18}$$

$$\xi\left(t+\frac{\delta t}{2}\right) = \xi(t) + \frac{\delta t}{2Q}\left[\sum_{i=1}^{N} m_i\frac{\mathbf{v}_i(t)^2}{2} - \frac{3N+1}{2}k_BT\right] \tag{2.19}$$

The NVT ensemble is useful for modelling certain experimental systems, such as the surfactant monolayers presented in this thesis. Other laboratory experiments are often better represented by the NPT ensemble however, such as surfactant micelles, in which the system is coupled to the atmosphere. In this instance, pressure must be regulated as well as temperature. The system pressure is calculable in a rather straight forward manner via the virial equation:

$$P = \frac{k_{\mathrm{B}}TN}{V} + \frac{1}{Vd}\left\langle\sum_{i<j}\mathbf{f}_{ij}\cdot\mathbf{r}_{ij}\right\rangle \tag{2.20}$$

where d is the dimensionality of the system, $\mathbf{f}_{ij}$ is the force exerted on particle i by particle j due to the force field and $\mathbf{r}_{ij}$ is the vector connecting atoms i and j. The first term on the right hand side of Eqn. 2.20 is an ideal gas term and the second is an interaction term: an ensemble average over the pairwise forces and distances. Similarly to thermostats, there is a simplistic approach to controlling the system pressure and this is achieved by periodically rescaling the system volume, along with particle coordinates, such that the pressure is equal to the desired value. Once again, this will not produce the correct ensemble.

The Nosé-Hoover barostat [60], analogous to the Nosé-Hoover thermostat, also uses an extended Lagrangian approach to pressure regulation. The additional degree of freedom in the Nosé-Hoover barostat, denoted by χ, corresponds physically to an

external piston which results in the following equations of motion:

$$\frac{d\mathbf{r}_i(t)}{dt} = \mathbf{v}_i(t) + \eta(t)(\mathbf{r}_i(t) - \mathbf{r}_{\mathrm{CM}} \tag{2.21}$$

$$\frac{d\mathbf{v}_i(t)}{dt} = \frac{\mathbf{f}_i(t)}{m} - [\eta(t) + \chi(t)]\mathbf{v}_i(t) \tag{2.22}$$

$$\frac{d\eta(t)}{dt} = \frac{1}{\tau_T^2}\left(\frac{T}{T_0} - 1\right) \tag{2.23}$$

$$\frac{d\chi(t)}{dt} = \frac{1}{Nk_B T_0 \tau_P^2} V(t)(P - P_0) \tag{2.24}$$

$$\frac{dV(t)}{dt} = 3\chi(t)V(t) \tag{2.25}$$

where $\mathbf{r}_{\mathrm{CM}}$ denotes the system centre of mass position vector, $V(t)$ is the volume of the simulation box, η is the thermostat extra degree of freedom and τ_T is the thermostat time constant. Meanwhile, χ represents the barostat extra degree of freedom and can be considered as a volume scaling factor and τ_P is the barostat time constant. The Nosé-Hoover barostat has been used in this thesis to generate a constant NPT ensemble where desired.

2.1.7 Boundary Conditions

Whilst thermostats and barostats provide the means to model different thermodynamic ensembles, further algorithmic developments have been made to get around problems of the limited computing resources available. Ideally we would like to calculate macroscopic properties of the materials which are being modelled, however the number of atoms that present-day computers are capable of simulating ranges from hundreds to several millions of atoms. This range is nowhere near the thermodynamic limit ($N_{\mathrm{A}} = 6.022 \times 10^{23}$) and using hard wall boundary conditions would result in a large fraction of the particles interacting directly with the simulation box surface. To simulate bulk properties, it is necessary to use boundary conditions that mimic an infinite bulk surrounding the N-particle simulation box. This is achieved

by choosing periodic boundary conditions, as are shown in the diagram in Figure 2.3. In this framework, particles interact with neighbours through the boundaries and when a particle diffuses across a periodic boundary, it re-enters the box on the opposite side which effectively deems the box to be infinite in size. One potential problem that could arise is if a particle were to interact with its own periodic image or 'ghost' which would lead to non-physical behaviour. This provides motivation for the 'minimum image convention' which sets a constraint on the relation between the sizes of the interaction cutoff distance and the length of the simulation box: $r_c > L/2$. Additionally, one should be wary of spurious correlations which result from the finite sized simulation box and as such, fluctuations with wavelength $\lambda = L$ are the largest that can be studied. This effect is relevant to many properties of interest such as capillary wave fluctuations at surfactant monolayer interfaces.

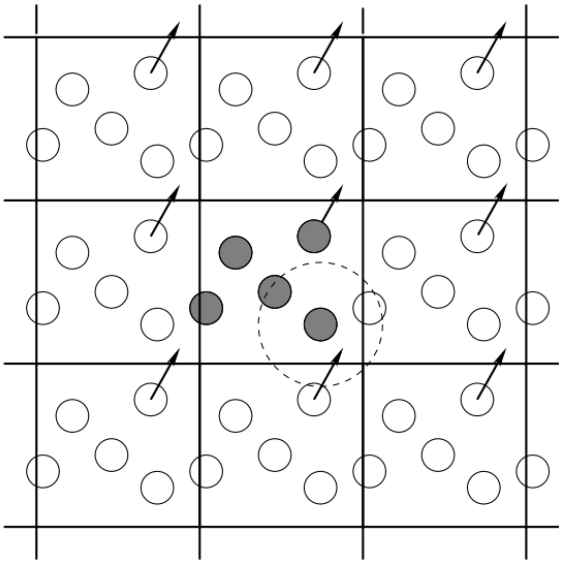

.

Fig. 2.3: A diagram showing a simple system in a periodic simulation box. The dashed circle depicts the interaction cut-off for pair-wise dispersion interactions and the arrows show a particle and its images travelling through the box boundary. Image adapted from [61]

2.1.8 Neighbour Lists

Employing a cutoff for pairwise interactions goes some way to alleviating the burden of force calculation, however it still remains a cumbersome process and so additional action is taken to further reduce processing time. Verlet neighbour lists contain for each atom, i, the list of indices j whose distance from i is less than a specified cutoff. These lists are time consuming to construct and must be updated periodically throughout the simulation as atoms drift in and out of the Verlet cutoff. The lists are typically updated every 10-20 time steps and they decrease the force evaluation time dramatically. Alternatively, the simulation box can simply be subdivided up into cells providing that the characteristic dimension of these cells is larger than the interaction cutoff. In this case, only the atoms, j, within the same cell and the nearest neighbour cells of atom i need to be considered in force evaluation. Furthermore, it has become standard to parallelise simulations on multiple processors using this technique whereby each individual domain is distributed to a single processor and communication is limited to nearest neighbour cells [62].

2.1.9 Water Models

Solvent effects are highly influential in the behaviour of many molecular systems, therefore the choice of how solvent is represented in a simulation has immense implications for the behaviour observed. Several implicit solvent models, including the Poisson-Boltzmann and Generalised Born schemes, are able to mimic solvent to a certain degree and have the advantage of being computationally inexpensive. The dynamics of these implicit solvent models are unrealistically fast however, due to a lack of friction between molecules which is problematic when studying kinetic processes like diffusion or self-assembly. Furthermore, simulation setups which have an inhomogeneous water density, such as the surfactant monolayers at the air/water interface presented in this thesis, cannot be modelled using an implicit solvent rep-

resentation. Accurate simulation of hydrophobicity is heavily reliant on the water model as well and to study the dynamics of water molecules and interfacial effects of systems such as surfactant micelles requires a more realistic approach to solvation, namely explicit water models.

A great deal of effort has been applied to providing explicit representations of water molecules in recent years. Broadly speaking, water models can be classified by three different properties: i) their number of 'sites' (interaction points), ii) whether the model has a fixed geometry or if its flexible and iii) whether the model is polarisable or not. Water models range from 2-site models, like that put forward by Dyer *et al* [63], to 6-site models such as that proposed by Nada *et al* [64] which was developed for the simulation of ice and water near the melting point. These models are all designed to reproduce particular physical properties of water, however no single current model is proficient at reproducing all desired properties and so care must be taken to choose the most appropriate model for a given system. Given that the CHARMM force field parameters have been developed with respect to the TIP3P water model [65], the version which was modified for the CHARMM forcefield [66] is used throughout this thesis. Whilst this water model is computationally inexpensive containing merely 3 sites, it is not without its drawbacks. Analysis of bulk water simulations modelled using the modified TIP3P water model revealed that the first peak in the oxygen-oxygen $g(r)$ is predicted to be too low and the structure beyond the first peak is missing. Additionally, the self-diffusion coefficient is overestimated as compared to experimental data [67].

2.2 Enhanced Sampling Methods

As discussed previously in Section 2.1, MD simulations can be an extremely useful tool for providing insight into molecular systems which exist on moderate length and time scales. MD simulations typically reach nanoseconds, occasionally microseconds

of real time. However many processes such as self-assembly occur on much larger spatial and/or temporal scales than what is achievable within standard MD. To study these processes using standard MD may require orders of magnitude more computing resources than those available. Or equally, the relevant states of the system which one may wish to observe could be separated by large energy barriers, which would realistically never be crossed during the course of a normal MD run, as shown schematically in Figure 2.4a. Enhanced sampling methods can help to alleviate some of these problems, usually by applying some form of external potential to the system to increase the rate at which it samples phase space.

2.2.1 (Well-Tempered) Metadynamics

Metadynamics is an enhanced sampling technique which encourages the system to visit unexplored regions of phase space and sample the entire free-energy landscape by flooding the free-energy minima. This is achieved by applying a history-dependent external bias potential as a function of some carefully chosen, slow moving collective variables. Not only does this technique allow the system to explore the free energy landscape in an accelerated manner, but it also allows the construction of the underlying free energy landscape of the system. This is a very desirable property because it provides a global description of the system and reveals all of the relevant local minima along with the size of the free energy barriers between them. Once this information is obtained, the free energy barriers separating these minima can be used to estimate the transition rates between them. The dynamics of the system are biased by means of a few chosen collective variables, $\mathbf{s}$, which are typically a function of many of the atomic coordinates, i.e $\mathbf{s} = \mathbf{s}(\mathbf{q})$. The external potential applied to the system is composed of small Gaussian hills which are deposited in the CV space over time. The external bias potential as a function of the CVs, $\mathbf{s}$, at

time t is defined as:

$$V(\mathbf{s},t) = \sum_{\mathrm{k}\tau<\mathrm{t}} W(k\tau) \exp\left(-\sum_{i=1}^{d} \frac{(s_i - s_i(q(k\tau)))^2}{2\sigma_i^2}\right) \tag{2.26}$$

where τ is the Gaussian deposition stride, σ_i the width of the Gaussian for the i^{th} CV and $W(k\tau)$ denotes the height of the Gaussian hills. The values of these parameters are somewhat interlinked and must be carefully chosen. For example, if the time interval between Gaussian depositions is short, then the Gaussian width should also be small to avoid placing successive Gaussian hills directly on top of one another. The height of the Gaussian hills should also be chosen carefully and there is a balance to be struck between setting this value too large, which will result in a quickly converging yet coarse free-energy landscape, and setting the height too small which will yield a smooth and detailed but slowly converging free-energy landscape.

The Gaussian functions are repulsive and so they have the effect of making the locations where they are deposited in CV space less favourable. At positions in CV space corresponding to unfavourable system configurations, the system will require little to no external repulsion to escape and the system will diffuse away from states corresponding to these areas with very few Gaussian hills deposited. Conversely, at positions corresponding to highly favourable low energy states in CV space, the system will require a strong external push for this state to become unfavourable, resulting in the large accumulation of Gaussian hills at these locations. In the limit of $t \to \infty$, the external bias potential tends towards minus the free energy plus a constant and is easily recovered:

$$V(\mathbf{s}, t \to \infty) = -F(\mathbf{s}) + C \tag{2.27}$$

In standard metadynamics the height of the Gaussian hills is fixed throughout the entire simulation, this results in the free energy oscillating around the real value after

convergence which imposes an error in the final free energy (see Figure 2.4b). This problem is combated in well-tempered metadynamics [68] by making the Gaussian hill height a decaying function of simulation time:

$$W(k\tau) = W_0 \exp\left(-\frac{V(\mathbf{s}(\mathbf{q}(k\tau)), k\tau)}{k_B \Delta T}\right) \tag{2.28}$$

where W_0 is the initial Gaussian height, k_B is the Boltzmann constant and ΔT is a parameter with the dimension of temperature. In the long-time limit, the bias potential converges smoothly as illustrated in Figure 2.4c. The free energy is recovered from the external bias potential as follows:

$$V(\mathbf{s}, t \to \infty) = -\frac{\Delta T}{T + \Delta T} F(\mathbf{s}) + C \tag{2.29}$$

where T denotes the temperature of the system in the simulation. The parameter ΔT can be used to formulate the quantity, γ, commonly referred to as the "bias-factor" which is the ratio of the temperature of the CVs ($T + \Delta T$) and the system temperature (T):

$$\gamma = \frac{T + \Delta T}{T} \tag{2.30}$$

The magnitude of ΔT (and therefore γ) affects the rate of free energy exploration, with $\Delta T = 0$ corresponding to standard MD and $\Delta T = \infty$ corresponding to standard metadynamics.

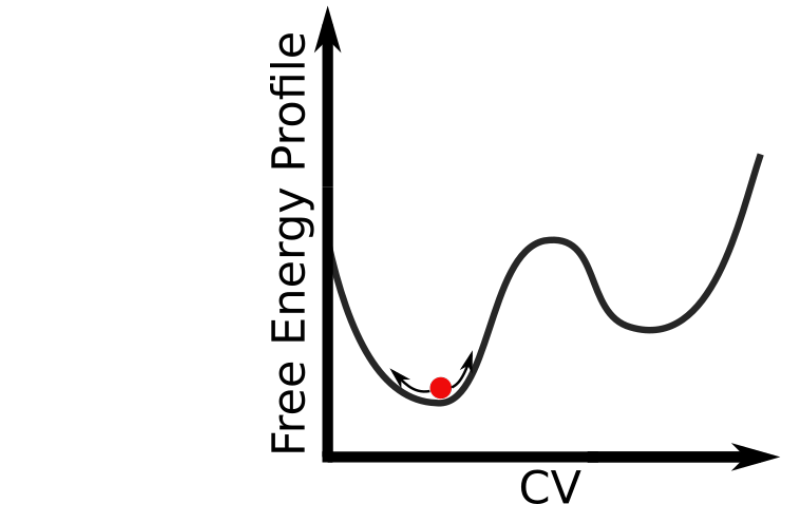

(a) Molecular Dynamics

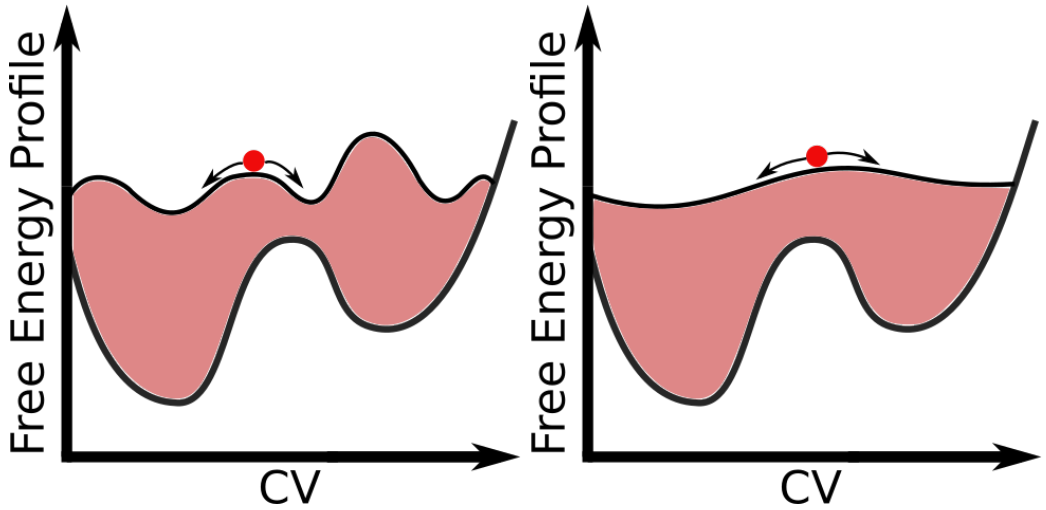

(b) Metadynamics **(c)** Well-Tempered Metadynamics

Fig. 2.4: Schematic diagrams illustrating exploration of the free energy landscape as a function of a single collective variable for a) molecular dynamics, b) metadynamics and c) well-tempered metadynamics simulations. The history dependent external bias potential is depicted by the pink regions in the figures.

Chapter 3

Simulating and Analysing Surfactant Monolayers

In Chapters 4 and 5, results are reported from all-atom MD simulations of surfactant monolayers. The purpose of this chapter is to explain the set-up of the simulated systems, simulation protocol and rationale behind the analysis conducted on these monolayers. For clarity, the setup procedure of the monolayer simulations is described separately for Chapters 4 and 5 in Section 3.1.

3.1 Building Initial Monolayer Systems

3.1.1 Docecyl Sulphate Monolayers with Li^+, Na^+, Cs^+ and NH_4^+ Counterions

Chapter 4 focusses on four different all-atom molecular dynamics (MD) simulations which were used to investigate the structural and interfacial properties of dodecyl sulphate (DS^-) surfactant monolayers at the air/water interface with different counterions (Li^+, Na^+, Cs^+, NH_4^+) present. The monolayer systems are comprised of two monolayer leaflets separated by a 60 Å thick water slab, which ensures that the elec-

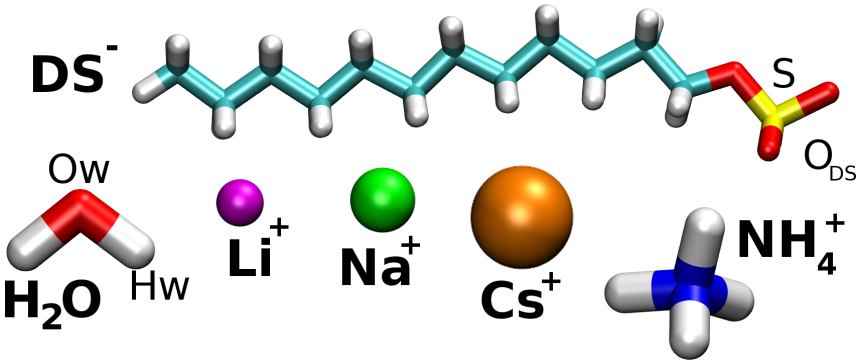

Fig. 3.1: The chemical structures of the molecular species featured in Chapter 4: DS^-, water and counterions. The colours cyan, white, red, yellow and blue are used to represent the elements: carbon, hydrogen, oxygen, sulphur and nitrogen respectively for the non-monatomic species. The monatomic counterions Li^+, Na^+ and Cs^+ are depicted in the colours magenta, green and orange respectively.

trostatic interactions from one monolayer are not felt by the other monolayer. The resulting water slab consists of 9600 water molecules with a density of 1 g/ml. Each monolayer leaflet contains 100 DS^- monomers within a simulation box with $x-$ and $y-$ dimensions of 69.28 Å each such that the area per surfactant is $\sim$ 48 Å^2. The area per surfactant used in the DS^- monolayer simulations is in agreement with the experimentally determined value for SDS monolayers [69] and is used for all reported monolayers so that the system properties can be fairly compared. Periodic boundary conditions were applied in all dimensions, with the $z-$ dimension of the simulation box set to 200 Å to ensure that the monolayers do not interact with one another through the periodic boundary in the z-axis. The centre of mass of each system was constrained to be at the position $z = 0$ throughout the simulation in order to make the analysis of the simulation as easy as possible. The initial configuration for the SDS monolayer system is shown in Figure 3.2 which illustrates the monolayer geometry.

The initial structures of the DS^- monolayers were built using the Packmol software package [51] and were neutralised by the addition of 100 Na^+/NH_4^+ counterions for the SDS/ADS systems per leaflet, which were placed near the headgroup regions of the DS^- molecules. For lithium dodecyl sulphate (LDS) and caesium dodecyl sul-

phate (CDS), the final state of the SDS monolayer after the production simulation was taken as a starting point and the parameters for the point-like counterions were simply modified to represent the appropriate ionic species.

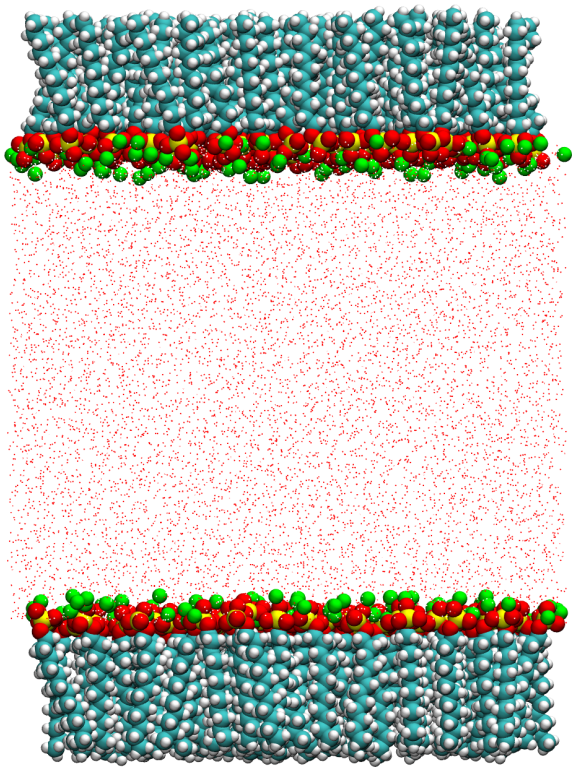

Fig. 3.2: The initial configuration for the SDS monolayer system in Chapter 4. The colours cyan, white, red, yellow and green are used to represent the elements: carbon, hydrogen, oxygen, sulphur and sodium respectively.

3.1.2 Dodecyl Sulphate Monolayers Interacting with Testosterone-Based Compounds

In Chapter 5, the results from MD simulations of three different testosterone-based compounds (testosterone (T), testosterone propionate (TP) and testosterone enanthate (TE)) interacting with monolayers consisting of sodium dodecyl sulphate and ammonium dodecyl sulphate are presented. The chemical structure of each of these drug molecules is shown in Figure 3.3. The final state after the production simulations of the SDS and ADS monolayer simulations, were used as a starting point for

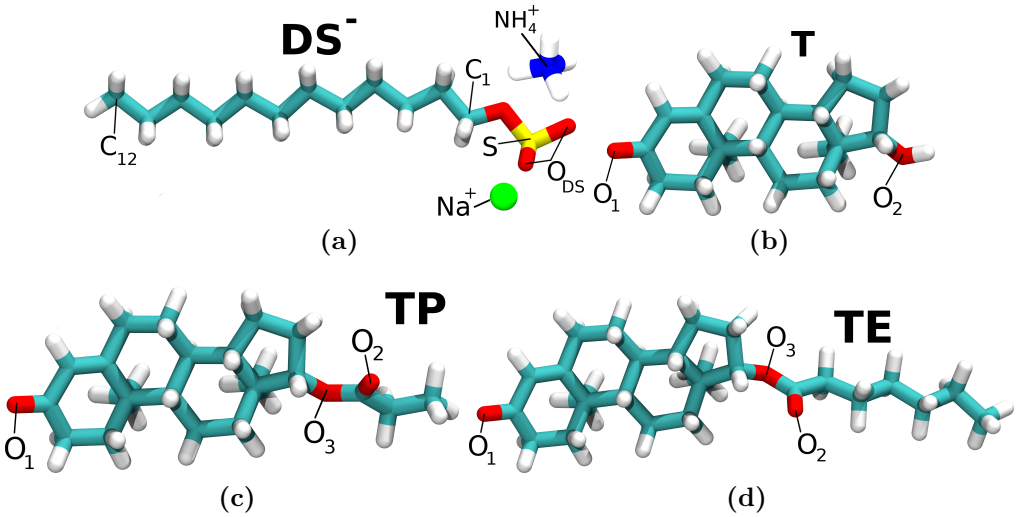

Fig. 3.3: The chemical structures of: a) DS^- with Na^+ and NH_4^+ counterions, b) T, c) TP, d) TE. In these figures, the colours cyan, white, red, yellow, green and blue are used to represent the elements: carbon, hydrogen, oxygen, sulphur, sodium and nitrogen respectively.

the monolayers interacting with testosterone-based compounds. The drug molecules were initially placed randomly in the vacuum regions above and below the top and bottom monolayer leaflets respectively in each system, within 5-10 Å of the hydrocarbon tails and oriented such that they were perpendicular to the z-axis, as shown in Figure 3.4. The placement of the drug molecules in these regions was done in order to mimic the placement of the drugs in the experiments in which n-hexane is used to deliver the drugs onto the hydrocarbon tails of the monolayers.

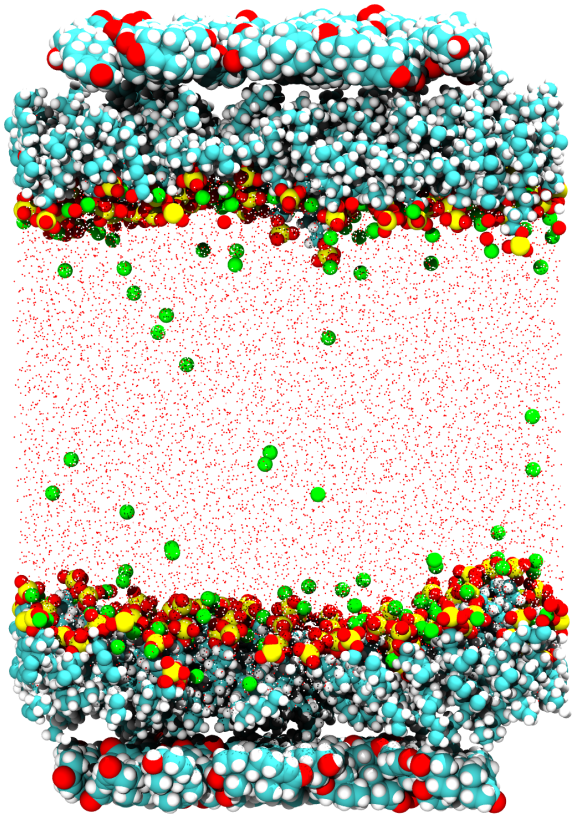

Fig. 3.4: The initial configuration for an SDS monolayer with testosterone molecules presented in Chapter 5. The colours cyan, white, red, yellow and green are used to represent the elements: carbon, hydrogen, oxygen, sulphur and sodium respectively. The testosterone molecules are visible in the vacuum regions both above and below the respective monolayer leaflets.

3.2 Simulation Protocol

Energy minimisations were performed on all monolayer systems using 100000 steps as the maximum number of force/energy evaluations and the minimised states of these systems were then simulated in the constant NVT ensemble for 10 ns for thermalisation. Finally, 50 ns production runs were performed in the NVT ensemble from which the analysis is conducted. All monolayer simulations in Chapters 4 and 5 were performed at T = 300 K using the LAMMPS simulation package [70] with the CHARMM force field [71, 72] for the description of both inter- and intra-molecular interactions of the DS^-, the various counterions and also the testosterone-

based compounds (where applicable) [73, 74]. The TIP3P water model [65], which was modified for the CHARMM forcefield [66], was used to describe interactions involving water. This combination of forcefields has previously been shown to give a good description of SDS micelles [75, 76]. The van der Waals interactions were cut-off at 10 Å whilst the electrostatic interactions were cut-off at 12 Å. The PPPM method [49] was used to compute long-range Coulombic interactions. The equilibration and production runs for all monolayer simulations utilised the Nose-Hoover thermostat [77] to fix the system temperature. A timestep of 2 fs was used in all simulations to ensure stable integration of Newton's equations of motion with the *velocity Verlet* algorithm whilst all hydrogen-containing bonds were constrained using the SHAKE algorithm [56]. The measurements discussed in Chapters 4 and 5 were conducted using the last 10 ns of the production periods obtained, in which the dynamics were deemed to be stable for each simulation.

3.3 Analysis Techniques

3.3.1 Constructing an Intrinsic Surface for a Surfactant Monolayer

Developing a description of the interfacial behaviour and structure of surfactant aggregates is crucial to understanding their function for many different processes. Physical properties such as size, geometry/shape, hydrophobicity and roughness all have an affect on the observed behaviour of aggregates and are largely influenced by the surface properties. It is therefore of vital importance that a thorough and careful treatment of the interfaces of these structures be incorporated into analysis. For a system comprising of two distinct phases, the *intrinsic surface*, denoted by $\xi(\mathbf{R}) = \xi(x, y)$, is defined as the location in which one phase comes in contact with the other. In general, the intrinsic surface is constructed from a finite number of

anchor points: atoms which are deemed to be at the interfacial region. For many liquid systems, determining which atoms are present at the interface at a particular instance is a problem in itself. For example in a system where an oil phase and a water phase meet, it is not immediately obvious how to determine the atoms to use as anchor points. For DS^- monolayers however, the predictable geometry of surfactant monolayers is exploited, specifically the knowledge that the headgroups will be in contact with water. The choice of anchor points for DS^- monolayers is therefore trivial: the sulphur atoms in the DS^- headgroups.

There are a number of different ways to construct the intrinsic surface for liquid interfaces reported in the literature. These include the *intrinsic sampling method* proposed by Tarazona *et al* which constructs a smooth mathematical surface which passes through all of the identified surface anchors while minimising the resulting surface area of the surface [78]. In this method, the surface is constructed from a linear combination of sine and cosine functions and has been applied to a study of surfactant monolayers at water-oil and water-vapour interfaces by Bresme *et al* [79]. Meanwhile, Chandler *et al* utilised a coarse-grained density field approach to establish the interface between water and heterogeneous surfaces. This method involves using a density criteria on a cubic lattice to establish boundaries between phases and thus approximate the intrinsic surface [80]. For computational efficiency, the analysis in Chapters 4 and 5 employs the algorithm proposed by Berkowitz *et al* [81]. In essence, this method is performed by projecting the location of a particle of interest and the anchor points used to define the interface onto the x-y plane. Next, the closest anchor point to the particle of interest within this projected two-dimensional representation is established. Finally, the location of the intrinsic surface for the particle of interest is assigned the value of the z-coordinate of the closest anchor point.

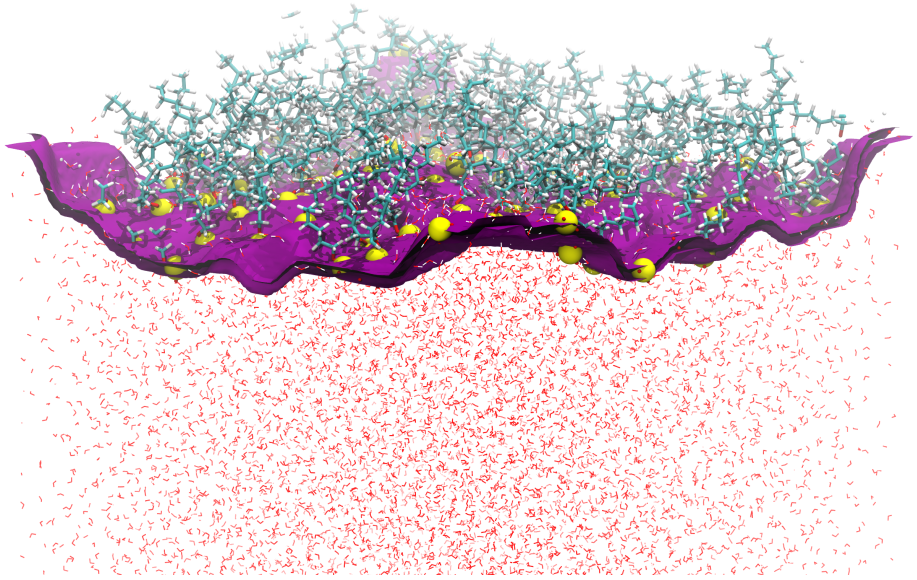

Fig. 3.5: Depiction of the intrinsic surface for one snapshot of an SDS monolayer. The colours cyan, white, red, yellow and blue are used to represent the elements: carbon, hydrogen, oxygen, sulphur and sodium respectively. The intrinsic surface is depicted in purple.

3.3.2 Determination of the Intrinsic Density

In the DS^- monolayer systems, the intrinsic density is used to describe the average density of different atomic species as a function of their distance away from the intrinsic surface. These plots are very useful for building a detailed picture of the interfacial structure with regard to the various different atomic components in the system such as counterions, solvent and drug molecules. The intrinsic density is particularly useful for describing the structure of water molecules in the vicinity of the interface, which is known to strongly impact the ability of solutes to penetrate through the monolayer surface.

The intrinsic density of a given atomic species is defined mathematically as:

$$\widetilde{\rho}(z) = \left\langle \frac{1}{A_0} \sum_{i=1}^{N} \delta(z - z_i + \xi(\mathbf{R_i})) \right\rangle \tag{3.1}$$

where the summation indexed by i runs over all N particles of a given atomic species,

$\xi(\mathbf{R_i})$ represents the *intrinsic surface* for a given configuration, $\mathbf{R_i} = (x_i, y_i)$ is the location of particle i in the x-y plane for a given configuration and A_0 is the cross sectional area of the interface. The z-coordinate of the i$^{\text{th}}$ particle is denoted by z_{i} and z represents the vertical distance from the DS^-/water interface to particle i where values of $z > 0$ and $z < 0$ represent locations within the water slab and towards the vacuum region respectively.

3.3.3 Measurement of Monolayer Structural Properties

A detailed description of the monolayer structure has been achieved through calculating numerous different instructive quantities which are reported in the next two chapters to study how monolayer structure changes when counterion species is varied (Chapter 4), and with the addition of testosterone-based compounds (Chapter 5). In the following paragraphs, these quantities are explained in detail whilst Figure 3.6 shows a pictorial description of each of them.

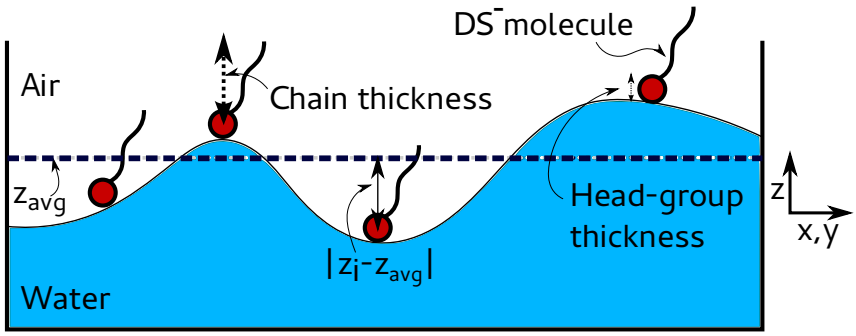

Fig. 3.6: Schematic diagram of the measured structural properties of DS^- monolayers. The thick dashed line represents the average z-coordinate of the DS^- headgroups in a monolayer, from which $|z_i - z_{\text{avg}}|$ is calculated and used to quantify monolayer roughness. Chain thickness and headgroup thickness measurements are also shown.

The instantaneous *monolayer thickness* is a useful property for monitoring how the surfactants arrange themselves within the monolayer. This is calculated by taking the end to end vectors of the surfactant molecules within a monolayer, projecting these onto the z-axis and then taking the average. Ensemble-averaged monolayer

thickness values were calculated by averaging the instantaneous monolayer thickness values over the trajectory. Meanwhile, the instantaneous *thickness of the headgroup region* of the DS^- monolayer is calculated in a similar manner as the full monolayer thickness and can be used to monitor how the head group region is affected as the monolayer composition changes. The thickness of a headgroup in a given DS^- molecule is determined by first establishing the maximum and minimum z-coordinates of the four oxygen atoms in the headgroup, and then taking the difference between the maximum and minimum of these z-values. Then to find the thickness of the headgroup region of a monolayer, this distance is averaged over all DS^- molecules in every snapshot. The *monolayer interfacial roughness* can strongly influence the ability of solutes to penetrate through the monolayer surface. This is described by the root-mean-squared deviation (RMSD) value of the difference between the z-coordinate of an S atom in the DS^- headgroup and the mean value of the z-coordinates of all S atoms present in a monolayer within a given configuration of the trajectory: $|z_i - z_{\text{avg}}|$, as shown in Figure 3.6.

The structure of the monolayers can also be considered in terms of angles formed between different parts of the surfactant molecules by calculating probability distributions of these angles over the course of the trajectory. The surfactant chain tilt angle, θ_t, is defined as the angle between the vectors formed between the C_1 atom (the headgroup carbon) and the C_{12} atom (the carbon of the terminal methyl group) and a unit vector in the z-direction. When this angle is zero, the hydrocarbon tail is parallel to the z-axis and when this angle is 90°, the DS^- molecule is lying in the x-y plane. The surfactant headgroup tilt angle, θ_h, was also investigated for all of the monolayer systems and is defined as the angle between the vector formed between S (the sulphur atom in the DS^- headgroup) and C_1 atoms, and the vector formed between C_1 and C_{12} atoms. When this angle is zero, the entire molecule is aligned linearly and when this angle is 90° the headgroup is oriented such that it is perpendicular to the DS^- hydrocarbon chain.

3.3.4 Position and Orientation of Testosterone Compounds

The preferred position and orientation of drug molecules within surfactant aggregates has profound implications on the nature of their encapsulation properties. These may be affected by the chemical nature of the drug and also the physical characteristics of the surfactant species itself, such as the choice of counterion and hydrophobic tail length. The orientation of drug molecules is described by the cosine of the angle formed between the vector pointing from the O1 atom to the O2 atom (see Figure 3.1) in the drug molecule and the unit vector: (0,0,1) or (0,0,-1) for drug molecules in the top or bottom monolayer leaflets respectively. When $\cos\theta$ is equal to -1, the entire drug molecule is aligned parallel to the z-axis with the O1 atom nearest the vacuum region and the O2 atom nearest the water slab, when $\cos\theta$ is equal to 0 the drug molecule is oriented in the x-y plane and when $\cos\theta$ is equal to 1, the drug molecule is again aligned parallel to the z-axis but with the O2 atom nearest the vacuum region and the O1 atom nearest the water slab.

The location of a drug molecule is used to determine how deep a drug molecule is inserted into the monolayer and is defined as the midpoint of the vector connecting the O1 and O2 atoms. In this case, the orientation distributions are calculated as a function of the distance of the drug molecule away from the intrinsic surface of the monolayer into the hydrocarbon tail region. For clarity, four distinct regions are defined: Headgroup, C_{1-4}, C_{5-8} and C_{9-12}. These regions are determined by assigning a surfactant chain the average surfactant chain tilt angle, as measured over the course of the simulations, and then determining the projection of the coordinates of the chain onto the z-axis. Then the regions are defined based on the location of the relevant atoms, as is shown in Figure 3.7. It should be noted that the size of these regions will vary as the mean surfactant chain tilt angle changes.

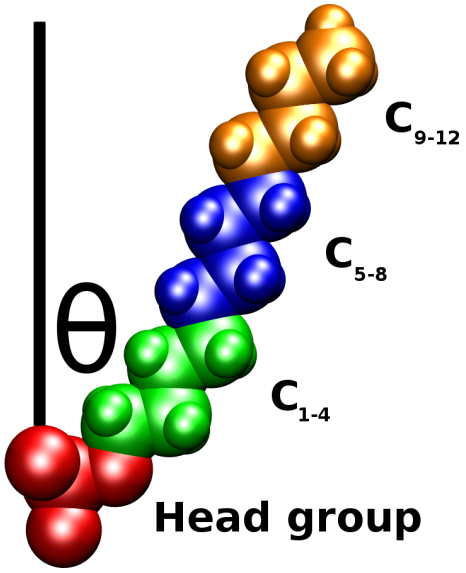

Fig. 3.7: A diagram which illustrates how the position of the drug molecules in the surfactants is determined: as a function of the mean tilt angle of the hydrocarbon tail, θ.

3.3.5 Radial Distribution Functions and Spatial Density Maps

Radial distribution functions (RDFs) are used extensively in this thesis to characterise the interactions between regions of interest in different molecules. RDFs describe the probability, relative to an ideal gas, of finding a neighbour atom at a distance r from a central atom. In Chapter 4, radial distribution functions (RDFs) and spatial density maps (SDMs) are reported in order to describe the interactions between the DS^- headgroups and the ionic solutions in the various systems.

In doing so, molecular axes are decided upon and assigned to all molecules in the system by the addition of pseudoatoms which form an orthogonal basis set, as shown in Appendix A. It is known that DS^- forms hydrogen bonds with water molecules via the ionic oxygen atoms in the headgroup. The simulation parameters are identical for these ionic oxygen atoms and thus it is reasonable to assume that the interaction between any one of them and the surrounding water molecules is the same. For this reason, the molecular axis for the surfactant molecule is chosen such that the z-axis points along the vector connecting the sulphur atom to one

of the ionic oxygen atoms. In this way, the behaviour of water around just one of the ionic oxygen atoms can be studied in a very detailed manner. Similarly, for water/ammonium molecules the z-axis points from the oxygen/nitrogen atom to the hydrogen atom which is involved in the hydrogen bond. Of the four different counterions studied, ammonium is the only species which has an orientation as it is not point-like.

The position of a molecule is given by the pseudoatom which forms the origin of the axis set on that molecule. The position and orientation of any two molecules in the system is described completely by the vector: $(r, \cos\theta_{cm}, \phi_{cm}, \theta_{or}, \phi_{or}, \psi_{or})$, where r denotes the magnitude of the separation between the two molecular axis sets, θ_{cm} and ϕ_{cm} denote the azimuthal angle and polar angle of the neighbouring molecule around the axis of the central molecule, respectively, and θ_{or}, ϕ_{or} and ψ_{or} are the three principal Euler angles of the neighbour molecule relative to the axis of the central molecule. Thus both the position and the orientation of a neighbouring molecule relative to the fixed axis set of a central molecule is completely described by these 6 variables.

Radial distribution functions are used to identify the nearest neighbour distance, which is defined as the distance corresponding to the first minimum in the rdf curves. SDMs of different neighbouring atomic species are produced by plotting points at the observed positions of the neighbouring atoms relative to the central molecule axes $(r, \cos\theta_{cm}, \phi_{cm})$. An isosurface is constructed based upon the density of these points in space. The resulting isosurface represents the most probable spatial region(s) to find a particular nearest neighbour atom and is advantageous over rdf curves as it contains information about three spatial dimensions as opposed to just one. In this way, an intuitive representation of positions of nearest neighbours is constructed around the central molecule.

In addition to SMDs, bivariate probability plots can also be constructed which show the probability of finding a nearest neighbour at a given set of azimuthal and

polar angles ($\cos\theta_{cm}, \phi_{cm}$). These have a direct correspondence with the appropriate SDMs however they reveal the varying probability of neighbours *within* the isosurfaces. If one takes only the data from the maximum region of these bi-variate probability plots then the orientational states of neighbour molecules in a highly localised region of space can be studied by examining the Euler angles adopted by these molecules.

The orientational state of a neighbour molecule relative to the fixed axis of a central molecule can be represented in a 3-dimensional space, where each individual point corresponds to a unique orientation of the neighbouring molecule. The three axes in this space represent the three principal Euler angles. In a similar manner to the SDMs, points are plotted which represent observations of orientations adopted by nearest neighbour molecules within the selected localised region in space. An isosurface can be constructed which forms a trivariate plot. These trivariate plots can then be used to elucidate the most probable orientational states adopted by the neighbour molecule. This is achieved by cutting the trivariate plot at periodic intervals along the axis which has the largest variance. Each slice is a bivariate probability distribution of two of the Euler angles, given a third (determined by where the slice was taken). From each slice, the most probable orientation is determined by the maximum of the resulting 2d histogram.

The radial distribution functions, spatial density maps and bivariate probability plots reported in this thesis were produced by utilising the ANGULA software package which is available for free download (https://gcm.upc.edu/en/members/luis-carlos/angula/ANGULA).

Chapter 4

Effects of Monovalent Counterions on Dodecyl Sulphate Monolayers

This chapter is based on the following publication;
Specific effects of monovalent counterions on the structural and interfacial properties of dodecyl sulfate monolayers. Allen *et al*, (2016) Phys. Chem. Chem. Phys. 18, 30394-30406

4.1 Introduction

The ability of surfactant molecules to adsorb to the air/water interface is crucial in a variety of application areas including the production of pharmaceutical, food and personal care products, mineral separation processes, petroleum recovery and environmental remediation [8–12, 14–16]. As a result, there has been and continues to be a wealth of scientific research using an array of experimental [82–95] and simulation [94–107] approaches in an attempt to understand the behaviour of various surfactant molecules, and the self-assembled structures which they form, at the air/water interface.

In this chapter, dodecyl sulphate has been investigated (DS^-; $C_{12}H_{25}SO_4$, as

shown in Figure 3.1), which is one of the more common anionic surfactants utilised in the various applications listed previously, with several different monovalent counterions (Li^+, Na^+, Cs^+ and NH_4^+, as shown in Figure 3.1). Specifically, this chapter aims to develop an understanding of how the different counterions affect the interfacial properties of the monolayers that form at the air/water interface. This interest is driven by the results of recent experimental work using a combination of density, viscosity and small angle neutron scattering experiments, which showed that ammonium dodecyl sulphate (ADS) micelles solubilised fewer molecules of poorly water soluble testosterone derivatives than sodium dodecyl sulphate (SDS) micelles, although the ADS micelles exhibited a lower level of hydration and formed bigger micelles [32]. Therefore, seemingly this difference in the solubilisation of the drug molecules is due to the change in the interfacial properties of the self-assembled surfactant micelles caused by the various counterions. In this chapter, the interfacial behaviour of the surfactant monolayer is being equated to that of the surfactant micelles. While the interface of a monolayer is less complex than that of a micelle, the two self-assembled structures are in thermodynamic equilibrium with one another and are found to both exist in experimental systems when the concentration of surfactants is in excess of the CMC.

Other studies have been carried out investigating the effect of varying the counterion of anionic surfactants on the ability of the micelles to solubilise molecules. Kim *et al.* found that both the aggregation number of the resulting micelles and the total solubilisation of pyrene in the DS^- aggregates increases as the counterion is changed from Li^+ to Na^+ to NH_4^+ but the number of pyrene solubilised per surfactant molecule is only slightly increased [108]. Cohen *et al.* found that the solubilisation of a corn protein, zein, decreases as the counterion used with a similar anionic surfactant, linear alkylbenzene sulfonate, is changed from Li^+ to Na^+ to K^+ to NH_4^+, with an even larger decrease observed when using the divalent cation Mg^{2+} [10].

The effect that the counterion has on the self-assembly and the structure of DS^- surfactants in aqueous systems, particularly for micellar systems [109–114] has been previously studied using both experimental and simulation methods. Molecular dynamics (MD) simulations of Li^+, Na^+ and NH_4^+ cations with DS^- micelles in aqueous solution by Rakitin and Pack [112] showed that the most compact structure for a micelle occurs with Li^+ cations that penetrate considerably deeper into the micelle than either Na^+ or NH_4^+ cations. Zana and coworkers used fluorescent measurements to determine that the aggregation number of ADS micelles is larger than those for SDS micelles and similar in size to caesium dodecyl sulphate (CDS) micelles [111, 113]. Sammalkorpi *et al.* used MD simulations to show that ionic strength of the solution affects not only the aggregate size of the resulting DS^- micelles but also their structure, where specifically they found that the presence of $CaCl_2$ induces more compact and densely packed micelles than those in the presence of NaCl [114].

In an attempt to gain a clear understanding of the interfacial properties of DS^- surfactant monolayers with different counterions, experimental and simulation studies of monolayer systems have also been carried out. Neutron reflection and surface tension measurements have been used by Lu *et al.* to determine that the area per molecule of DS^- surfactant monolayers and the number of water molecules per headgroup decreases as the counterion is changed from Li^+ to Na^+ to Cs^+ [82]. Using MD simulations Hantal *et al.* found that the distance between the peaks in the density of the cations and the DS^- ions depends on the size of the cation and the surface density of the anionic surfactant using MD simulations of DS^- monolayers with Li^+, Na^+, K^+, Rb^+ and Cs^+ counterions [101]. MD simulations of SDS monolayers in contact with solutions of NaCl, $MgCl_2$ and $CaCl_2$ salts have been carried out by Chen *et al.* from which they found that the sulphate groups are less bridged by ions in the divalent salts and more solvated by water and the alkyl tails become more disordered than for the monovalent salt [107]. While these studies have pro-

vided insight into the specific monolayer systems that were studied, they also reveal more detail into the general phenomena that drive the behaviour of ionic solutions at air/water interfaces which is of significant importance in the colloidal and interfacial science field, as is highlighted by several recent review articles [115–117].

Generally, ion specificity within a wide range of systems is usually referred to as Hofmeister effects, in acknowledgement of the pioneering work done by Franz Hofmeister [118, 119] that systematically classified ions in sequences based on their influence on protein solubility and denaturation (these sequences are now commonly referred to as the Hofmeister series). In the *direct* Hofmeister series, Na^+ is the reference cation, with Li^+ being more kosmotropic (more hydrated) than Na^+ and Cs^+ and NH_4^+ are more chaotropic (less hydrated than Na^+), such that they are ordered like NH_4^+ <Cs^+ <Na^+ <Li^+ [115, 116, 120]. This order will be used as a reference while discussing findings throughout the current chapter.

In this chapter, the results of a series of MD simulations are reported that have been used to determine the specific ion effects of lithium (Li^+), sodium (Na^+), caesium (Cs^+), and ammonium (NH_4^+) counterions with DS^- monolayers. Notably, it has been found that the ability for NH_4^+ cations to form hydrogen bonds directly with the DS^- headgroup leads to a significant dehydration of the headgroups as compared to what is observed with the other monatomic monovalent ions studied. As a result, significant changes are observed in the interfacial properties of the surfactants and the interfacial water in the ADS monolayer systems as compared to that observed in the other monolayers. To the best of the author's knowledge, this study represents the first detailed investigation of the interactions between these monovalent ions and DS^- monolayers.

The details of the monolayer systems, the simulation protocol and the various measurements used to characterise the interfacial properties reported in this chapter are outlined in Chapter 3 of this thesis.

4.2 Results & Discussion

In this section, the results derived from the simulations of DS^- monolayers with four different counterions (Li^+, Na^+, Cs^+ and NH_4^+) are presented. Specifically the effect that the different monovalent counterions have on the structure of the surfactant monolayers, the hydration of the DS^- headgroups, the structure of the water around the headgroup and the binding of the ions with the headgroups are presented below.

4.2.1 Location of Counterions in Relation to the Surfactant/Water Interface

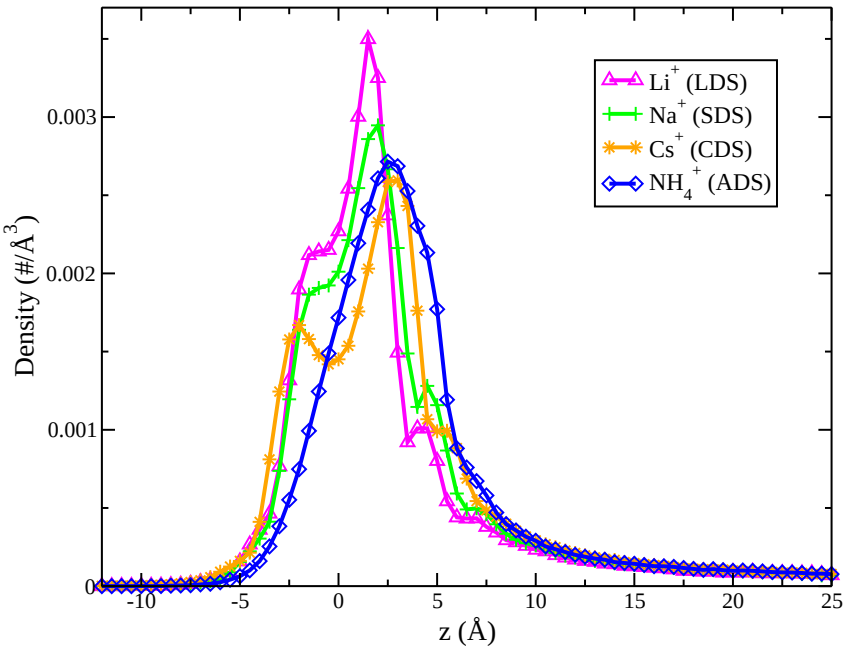

Fig. 4.1: Intrinsic density profiles of the Li^+ (magenta), Na^+ (green), Cs^+ (orange) and NH_4^+ (blue) ions.

Intrinsic density profiles have been used to study the location of the various different atomic species present in the monolayer simulations. Figure 4.1 shows the density of the different counterion species with respect to the monolayer interface. These plots reveal large peaks in the ion density at small positive values of z, which shows that the most probable location of the counterions is on the water side of

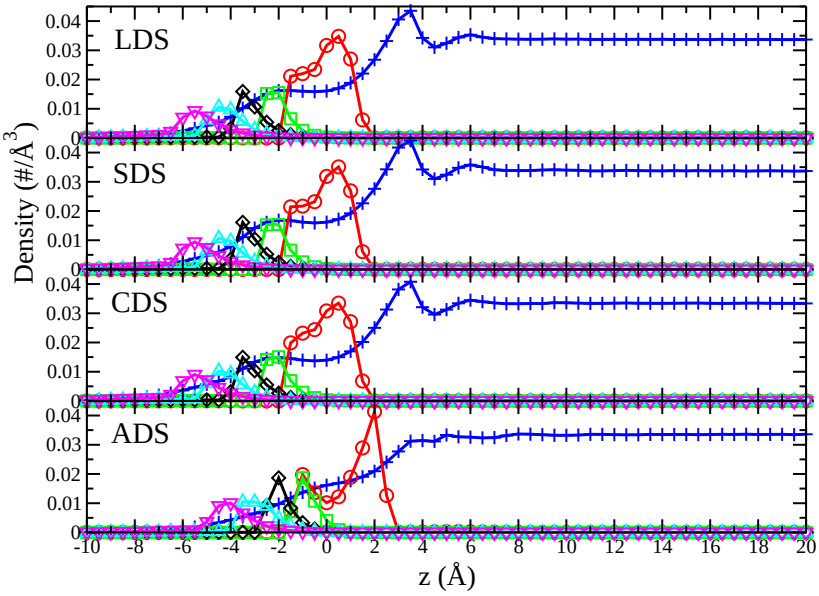

Fig. 4.2: Intrinsic density plots for the monolayer simulations. The colours green, black, cyan and magenta are used to depict the density of DS^- carbons 1-4 respectively. The colours blue and red are used to depict the density of oxygen atoms in water and oxygen atoms in DS^- headgroups respectively.

the surfactant/water interface. The densities of the various counterions tend to zero at positive values of z corresponding to the bulk water region and the intrinsic density curves are coincident at large values of z which suggests that the counterions' behaviour differs around the interface, not in the bulk water.

The Li^+ and Na^+ intrinsic density profiles exhibit 'shelves' on both sides of the main interfacial density peak. The value of the cation density in the shelf within the LDS monolayer is larger than that within the SDS monolayer (values of $z \leq 0$), conversely for the 'shelf' on the other side of the main peak, the Na^+ peak is at a larger density than the Li^+. This is most likely due to the size difference between these ionic species: lithium is smaller and thus more able than sodium to fit into the small spaces between the sulphate headgroups of the DS^- molecules.

Cs^+ ions are larger than Li^+ and Na^+ and have smaller densities for $-3 < z < 0$ than these two ions. This trend is consistent with that reported above where the densities within the monolayer decreases with increasing ion size. The intrinsic

density profile of Cs^+ ions exhibits a minima and a secondary peak within the monolayer rather than a shelf. This minima is located at $z = -0.5$ Å, which is just under the surfactant headgroups. This minima arises due to the larger size of Cs^+ and the many steric interactions resulting from the surfactant headgroup oxygen atoms in this location. Because of these strong interactions, Cs^+ will likely be forced either within the monolayer or to larger z values. Cs^+ exhibits a shelf at $z \sim 5$ Å, a feature which is also present in the intrinsic density profiles for Li^+ and Na^+.

The intrinsic density profile of the nitrogen atoms in the ammonium ions is also plotted in Figure 4.1. Only the nitrogen atom density was calculated so that the total number of atoms used to construct the intrinsic density plots was equal and thus the integral under all of the curves are equal. This ensures that meaningful comparisons of density can be drawn between the different ionic species. The nitrogen atoms in the NH_4^+ ions exhibit the broadest peak of the different counterion species. The position of this peak is situated closer towards the bulk water than the peaks for the Li^+ and Na^+ ions.

For the monatomic ions, there is a trend of decreasing density inside the monolayer as the ionic radii increases. The density of the NH_4^+ ions within the monolayer is lower than any of the monovalent cations. This trend agrees with what is explained in a recent publication by Sivan in which an unified explanation of various interfacial interactions of ions including the phenomena that result in small cations being attracted to hydrophilic interfaces [117].

Additionally, when investigating the intrinsic density of the oxygens in the headgroup and the water near the interface of the monolayers (as shown in Figure 4.2), a difference between the systems with monatomic ions and the system with NH_4^+ ions is observed. Specifically, in the systems with Li^+, Na^+ and Cs^+, a distinctive interfacial peak in the intrinsic density of the oxygens in the water molecules (O_W) occurs at a distance of ~ 3 Å from the intrinsic surface. Also, a broad distribution

of the intrinsic density of the O_W atoms in the surfactant headgroup is seen which is consistently increasing throughout a range of distances from ~ -2 Å to ~ 0.5 Å from the intrinsic surfaces, with a peak at $z \sim 0.5$ Å. However, in the system with NH_4^+ cations, there is no interfacial peak in the intrinsic density of the O_W atoms, which suggests that the water molecules do not pack as well into the same region of space and are therefore less ordered than at the interfaces with the monovalent cations. Additionally, two peaks in the intrinsic density of the O_{DS} atoms of the headgroup are visible, a large peak occurring at ~ 2 Å from the intrinsic surface and a smaller peak at ~ -1 Å from the intrinsic surface. Therefore, the orientation of the headgroups seems to be more constrained when they are interacting with the NH_4^+ counterions than when interacting with the other monatomic counterions.

These plots reveal that the counterions exhibit distinctly different behaviour at the monolayer interface which could have a significant effect on other monolayer structural and interfacial properties such as roughness, interfacial tension and the overall hydration of the monolayers, which will be discussed in the following sections.

4.2.2 Monolayer Structure

The results from the calculations of the monolayer and headgroup thickness for the various systems are presented in Table 4.1 with the standard deviations of the measurements reported as the errors. These results reveal that the monolayer thickness is unchanged by varying the counterion, which is unsurprising as the counterions also have little effect on the surfactant chain tilt angle which is shown in Figure 4.3. The headgroup thickness is also unchanged when the DS^- monolayers are interacting with solutions containing different counterions. These results are consistent with those from recent neutron reflectivity measurements of LDS, SDS and CDS monolayers [82].

Whilst the monolayer and headgroup thicknesses are unchanged with counte-

Table 4.1: Summary of the structural properties for the LDS, SDS, CDS and ADS monolayers.

	LDS	SDS	CDS	ADS
Full Thickness (Å)	10.7 ± 0.2	10.7 ± 0.2	10.7 ± 0.2	10.7 ± 0.2
Head Thickness (Å)	2.2 ± 0.01	2.2 ± 0.01	2.2 ± 0.01	2.2 ± 0.01
Roughness (RMSD) (Å)	2.5 ± 0.2	2.7 ± 0.2	3.4 ± 0.4	2.5 ± 0.2
Hydration water #	7.3 ± 3.3	8.3 ± 3.6	7.3 ± 3.0	6.6 ± 2.8
% ions bound to headgroup	53%	55%	68%	70%

rion species, these measurements contain no information regarding roughness of the surfactant-water interface: a property which could be pivotal in determining local water structure and thus the ability of an aggregate to effectively operate as a solubilising agent. The roughness of the LDS and ADS monolayers are the same with RMSD values of (2.5±0.2) Å. The fluctuations of surfactants in the SDS monolayers reveal slightly larger values with an RMSD of (2.7 ± 0.2) Å. The CDS monolayers however are significantly more rough with a RMSD value of (3.4 ± 0.4) Å. This may be due to stacking of adjacent surfactant headgroups due to the large size of the caesium ions. See Table 4.1 for a summary of all of the structural properties of the various monolayers.

4.2.3 Dehydration of Cations

To gain a better understanding of how dehydrated the ions are as they interact with the DS^- headgroups, the hydration of the counterions was calculated as a function of distance from the intrinsic surface of the monolayers. The nearest neighbour distances found from the $g(r)$'s for the interaction between each cation and the O_W atoms were used as the metric to determine whether a given water molecule was hydrating an ion or not. The average number of hydration water molecules around a given ion was determined by averaging the number of water molecules that are within the nearest neighbour distance from the $g(r)$, taking precautions not to double count any water molecules around a single ion.

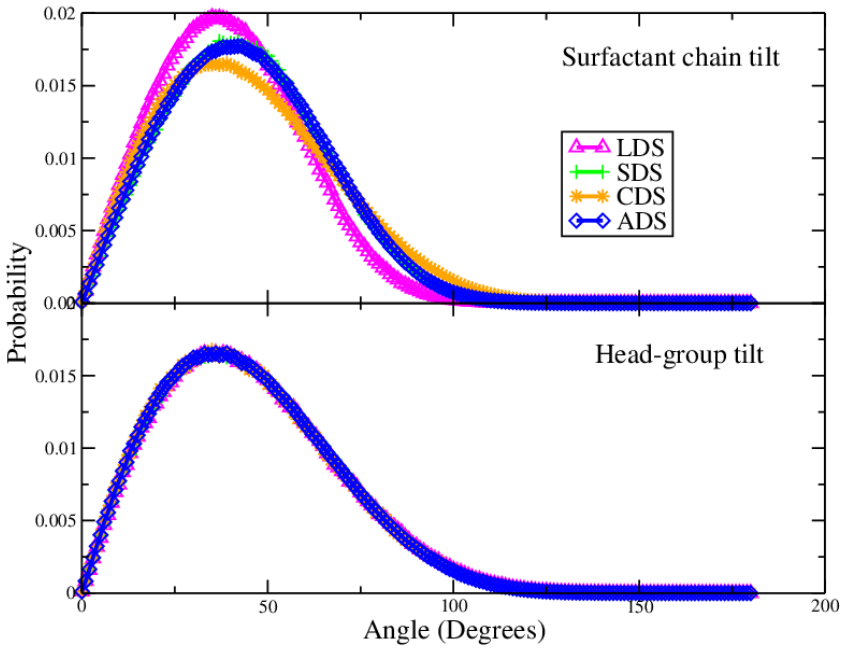

Fig. 4.3: Surfactant chain tilt and head tilt angle distributions. Lithium, sodium, caesium and ammonium are shown in the colours magenta, green, orange and blue respectively.

Figure 4.4 shows the mean hydration number of the different counterion species as a function of their distance to the interface, z. For all of the different counterions it is clear that the hydration number is always at a maximum in the bulk water (at large values of z) as one might expect. The hydration numbers of the various ions in the bulk water region are in good agreement with those measured using various simulation methods elsewhere: Li^+ (4.2 ± 0.4) [121], Na^+ (5.8 ± 0.4) [122], Cs^+ (9.6 ± 1.3) [123] & NH_4^+ (4.9 ± 1.4) [124]. This agreement between the results obtained using the non-polarisable CHARMM force field and the more rigorous *ab initio* methods reported in the preceding references is remarkable. Such an agreement suggests that the Hofmeister effects are adequately described by classical force fields, through varying the effective ionic radius and dispersion interaction strength via the Lennard-Jones interaction parameters.

All systems exhibit a decrease in the mean hydration number around the cations as they approach the monolayer/water interface ($z \sim 5 - 6$ Å). In this region, the

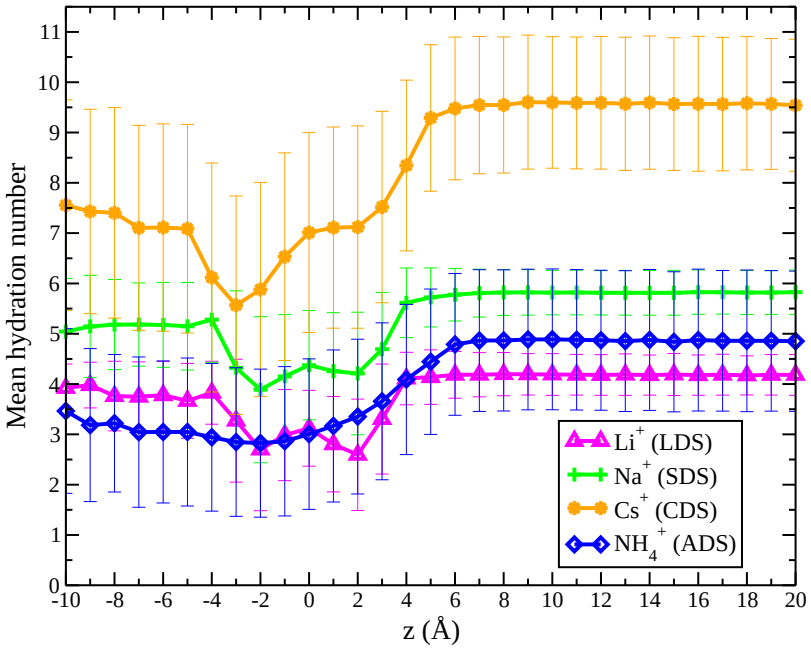

Fig. 4.4: The mean hydration number of the different counterions as a function of distance from the intrinsic surface of the monolayer, z.

DS^- headgroups will start to compete with neighbouring water molecules for the interaction with the cations and therefore result in a decrease in the average number of hydrating waters within the first hydration shell of the cations.

Beyond the interface, into the hydrocarbon tails ($z < -2$ Å), the mean hydration number increases and converges at a value which is less than that in the bulk for the monatomic counterions. This increase is due to the fact that there are less atoms (O_{DS}) in this region that will compete with the water molecules for interactions with the ions and so they interact more with the ubiquitous water molecules.

In the case of the NH_4^+ ions, a dehydration of the cations is observed starting at $z \sim 6$ Å. The decrease in hydration is then more or less monotonic until $z \sim -2$ Å, at which point the average number of hydrating water molecules plateaus. This would suggest that in general in this region, the NH_4^+ ions are interacting in a similar way with the DS^- headgroups and surrounding water molecules, and as has been seen in the intrinsic density plots, there is a continually decreasing number of ions in this region. It seems that the motion of these ions is restricted by their desire to

form hydrogen bonds with the O_{DS} atoms in the surfactant headgroups.

For the point-like ions, at all values of z, the average number of hydrating water molecules increases with the ionic radii of the ion. The ions which are most dehydrated by the interface are the Cs^+ and NH_4^+ ions as they both lose $\sim 40\%$ of their hydration shell when interacting with the DS^- headgroup. Meanwhile, the Na^+ and Li^+ ions only lose $\sim 30\%$ of the water molecules within their hydration shell. This trend in the dehydration of the ions agrees well with the Hofmeister series, which states that the Cs^+ and NH_4^+ ions are the most weakly hydrated of the four that were simulated and therefore the easiest to dehydrate, while Na^+ and Li^+ are more strongly hydrated.

4.2.4 Hydration of DS^- Headgroups

Radial distribution functions have been calculated to quantify the interactions between the DS^- headgroup and the water molecules. Figures 4.7a and 4.7b show the rdf, $g(r)$, curves for interactions between the ionic oxygen atoms in the surfactant headgroups O_{DS} and the oxygen atoms in the water molecules O_W, and the O_{DS} atoms and the hydrogen atoms in the water molecules H_W. The nearest neighbour distances obtained from $g(r)$ plots for all systems are shown in Table 4.2.

The O_{DS}–H_W $g(r)$ shows very little change as the counterion is changed. However, the $g(r)$'s for O_{DS}–O_W show slight differences in both peak amplitude and the curve shape. These differences arise from the effect that the different cations have on the structure of the interfacial water molecules, which will be discussed in greater detail in the following sections.

Using the nearest neighbour distances between sulphur atoms in the DS^- headgroup, S_{DS}, and the O_W atoms for each system ($d_{S,O_W} = 4.95$ Å), the number of hydration water molecules around a surfactant headgroup was determined by counting the number of nearest neighbour water molecules. Precautions were taken not

to double count any water molecules around the headgroups, such that any given water molecule was only counted as hydrating one surfactant molecule at any instance in time. The values reported in Table 4.1 are determined by averaging over every surfactant molecule and over every configuration in the production trajectory. The mean values of the number of hydration waters per headgroup are ordered as follows: NH_4^+ (6.6) < Li^+, Cs^+ (7.3) < Na^+ (8.3). A similar trend has been reported in a previous simulation study of LDS, ADS and SDS micelles in solution [112].

Histograms were constructed using all snapshots from the production simulations for the different systems and are shown in Figure 4.5. All of these histograms show broad distributions with hydration numbers per surfactant molecule ranging from 0 to 22 (in the case of SDS). ADS has the smallest value for the average number of hydrating water molecules and also the smallest spread of values in the histogram. CDS has the same average hydration number as LDS with a slightly smaller standard deviation.

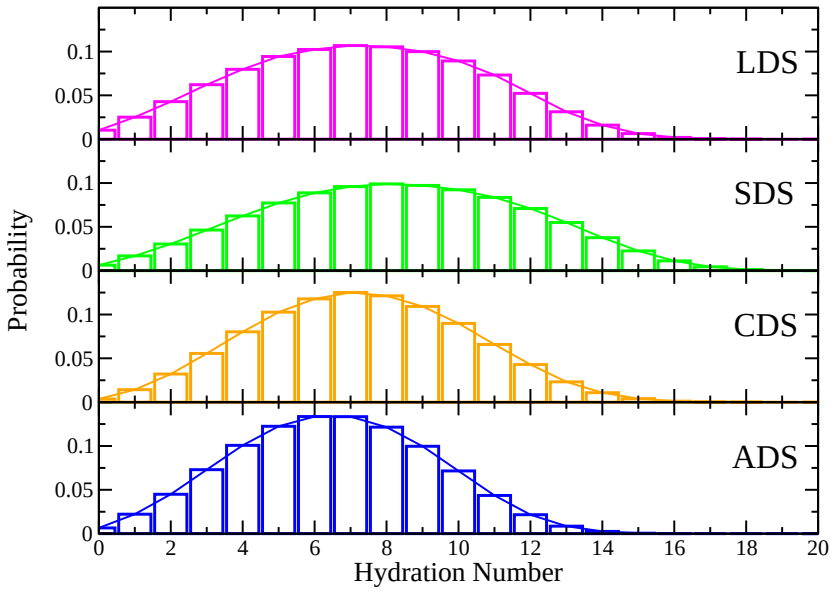

Fig. 4.5: Histograms showing the probability of a surfactant headgroup having a given hydration number in the monolayer simulations. The mean and standard deviation for each system is as follows: LDS – 7.3 ± 3.3, SDS – 8.3 ± 3.6, CDS – 7.3 ± 3.0 and ADS – 6.6 ± 2.8.

4.2.5 Interfacial Water Orientation

Using the methods described in Section 3.3.5, the orientational states of water molecules located within the small region of the O_W SDM corresponding to the most probable location to find a water molecule hydrogen bonded to a DS^- headgroup were studied.

The least probable water orientation at this particular point in space, as shown in Fig. 4.6a, shows the water molecule is oriented such that one H_W atom is forming a hydrogen bond with a O_{DS} atom and the other is oriented such that it points away from the air/water interface and into the bulk water region. On the other hand, the most probable water orientation at this point in space, Fig. 4.6b, is one in which the water molecule is oriented with one H_W atom is forming a hydrogen bond with a DS^- headgroup and the other H_W atom is directed toward the air/water interface such that it maximises hydrogen bonding between water and surfactant headgroups. This most probable water configuration is in agreement with the configuration of the water observed in recent sum-frequency generation spectrum studies of SDS monolayers [93, 95].

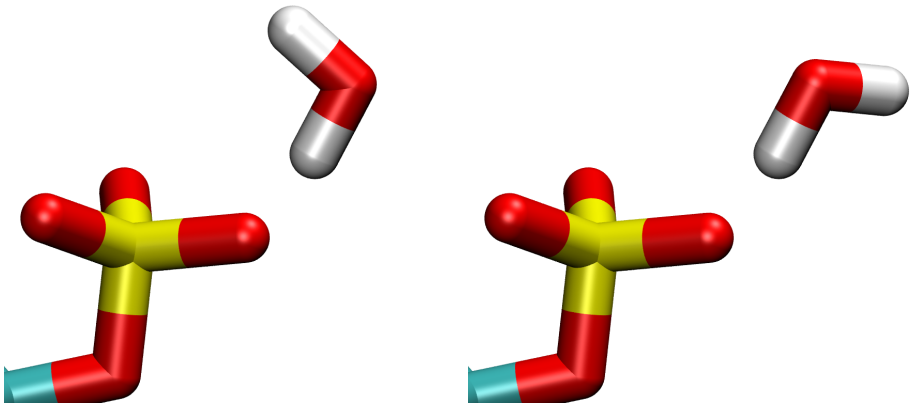

(a) **(b)**

Fig. 4.6: Representative snapshots of the least (a) and most probable (b) orientations of a bound water molecule within a small region of space around the DS^- headgroup from the CDS simulation.

Table 4.2: Nearest neighbour distances from the $g(r)$ curves between the O_{DS} atoms and the different atomic species in the water molecules and counterions.

	LDS	SDS	CDS	ADS
O_W	3.55	3.75	3.25	3.25
Li^+	2.65	-	-	-
Na^+	-	3.05	-	-
Cs^+	-	-	3.95	-
$N_{NH_4^+}$	-	-	-	3.55
$H_{NH_4^+}$	-	-	-	2.35

4.2.6 Counterion – DS^- Headgroup Interactions

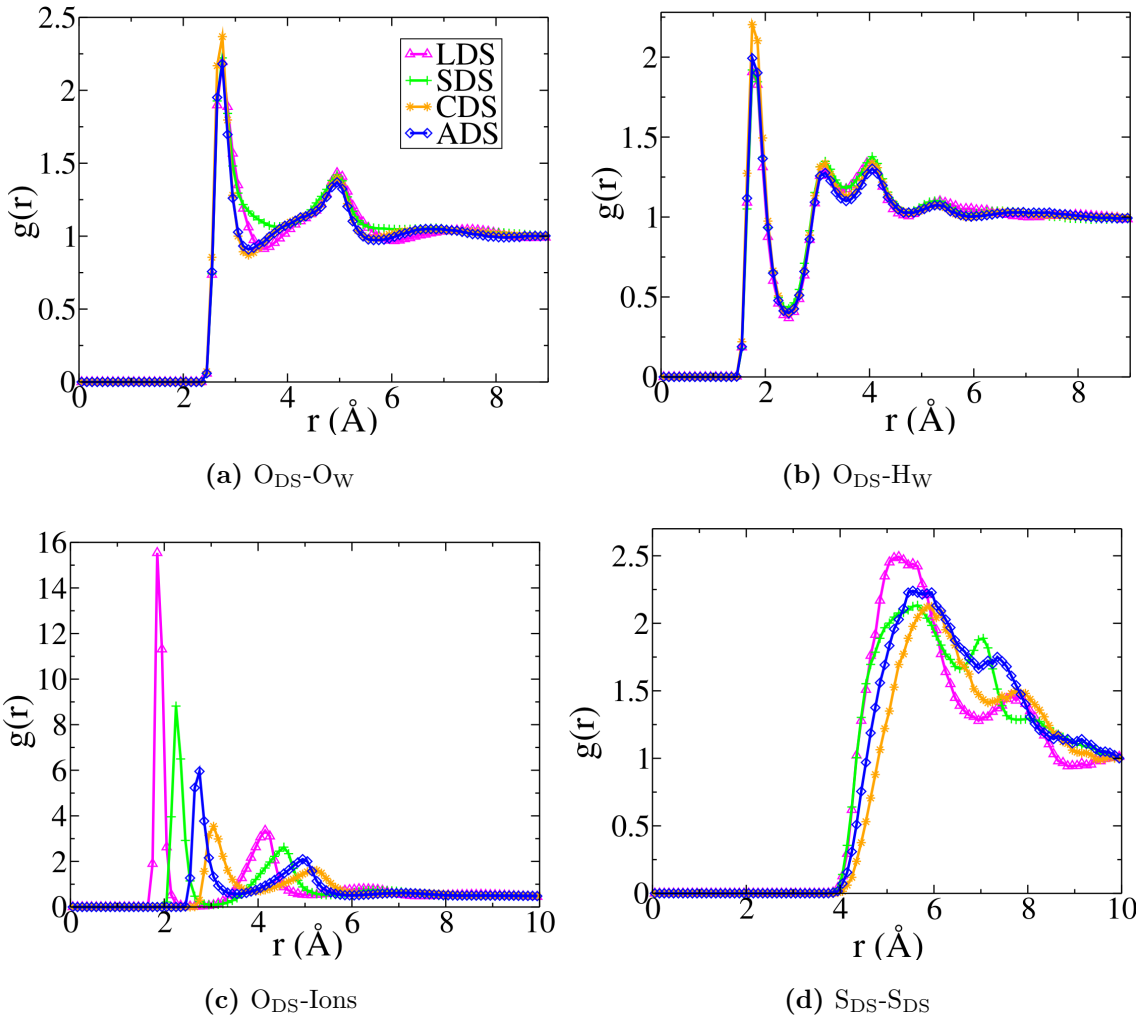

(a) O_{DS}-O_W **(b)** O_{DS}-H_W

(c) O_{DS}-Ions **(d)** S_{DS}-S_{DS}

Fig. 4.7: Radial distribution functions ($g(r)$s) for the (a) O_{DS} – O_W, (b) O_{DS} – H_W, (c) O_{DS} – counterion and (d) S_{DS} – S_{DS} interactions.

Fig 4.7 shows $g(r)$'s for the O_{DS} atoms and the counterions in the various systems. The nearest neighbour distances for each O_{DS} – counterion interaction are also summarised in Table 4.2. These values and the $g(r)$'s reveal that both the separations between ions in direct contact with the sulphate headgroups (first peaks) and the separations between hydrated ions and the sulphate headgroups (second peaks) increase in the series $Li^+ < Na^+ < NH_4^+ < Cs^+$, which is consistent with the trend of their respective ionic radii. Also, this is consistent with a previous simulation study of similar counterions with DS^- micelles [112].

SDMs of water molecules and counterions were produced for all of the monolayer systems and are shown for LDS, SDS, CDS and ADS in Figures 4.8a, 4.8b, 4.8c and 4.8d respectively. The SDMs produced for all of the monolayer systems reveal that the oxygen and hydrogen atoms in nearest neighbour water molecules occupy a region of space which is donut-shaped. The region representing the H_W atoms is nearer the O_{DS} than the region representing the O_W atoms, which is consistent with what was observed from the $g(r)$'s for these systems. Additionally, the diameter of the donut-shaped region for H_W atoms is smaller than that for the O_W atoms. Combining these two observations indicates that the water molecules in the first hydration shell are hydrogen bonded to the O_{DS} atoms in the headgroup, and this provides an explanation for the two donut-shaped SDMs when taking into account that the $OH_{water} \cdots O_{DS}$ angle would need to be no larger than 30°.

The SDMs also reveal that the point-like counterions (Li^+, Na^+, Cs^+) have a strong preference to reside behind the O_W atoms in the nearest neighbour water molecules. The Li^+ and Na^+ SDMs exhibit a very localised interaction with the DS^- headgroups, in which they both occupy circular-shaped regions behind the O_W SDMs. The SDM for Cs^+ differs somewhat from those of Li^+ and Na^+, as it exhibits larger clouds which suggest that the position of Cs^+ is less localised in relation to the surfactant headgroup. It appears then that the point-like counterion SMDs are located elsewhere in space from the SDMs representing water molecules. From this

it is deduced that none of the monatomic counterions (Na^+, Li^+ and Cs^+) are likely to displace a water molecule which is hydrogen bonded to the DS^- headgroup.

Meanwhile, the NH_4^+ ions show very different behaviour to the point-like ions. The SDMs for nitrogen and hydrogen atoms in NH_4^+ ions around the O_{DS} atoms are coincident with the SDMs for O_W and H_W atoms respectively, as can be seen by the blue and pink SMD in Figure 4.8d. This suggests that the NH_4^+ ions are able to displace interfacial water molecules from the DS^- head-groups which explains why the mean hydration number of the ADS surfactant headgroups are significantly less than for the other systems. The NH_4^+ ions are directly competing with the water molecules for hydrogen bonding partners within the DS^- headgroups, and are therefore forming stronger interactions with the headgroup than the other monatomic cations.

The SDMs show an isosurface of the most probable regions in space to find different atomic species depicted in Fig. 4.8, however the probability within these SDMs varies with some regions within the clouds being more probable than others. To elucidate the variance in probability within different regions of the SDMs, bivariate plots are exploited which show the probability as a function of the polar angles $\cos\theta_{cm}$ and ϕ_{cm}. The bivariate plots for the water molecules which are hydrogen bonded to the DS^- headgroups are similar for all systems. The donut-shaped SDMs of the O_W and H_W atoms in the water molecules materialise as donut-shaped rings on the bivariate plots, as shown for O_W atoms in Fig. 4.9a. These rings show a little variance in probability. There is a region of lower probability within the distribution of O_W atoms, centred at approximately $\cos\theta_{cm} = 0.3$, $\phi_{cm} = 100°$, which corresponds to a region of space between the DS^- headgroups and the hydrocarbon tails of the surfactant molecules. Within this same region, one finds the most probable location of the nitrogen atoms in the NH_4^+ ions, indicated by the sharp red region in Fig. 4.9b. This suggests that the ammonium ions dislodge water molecules in this region of space in order to favourably interact with the headgroups.

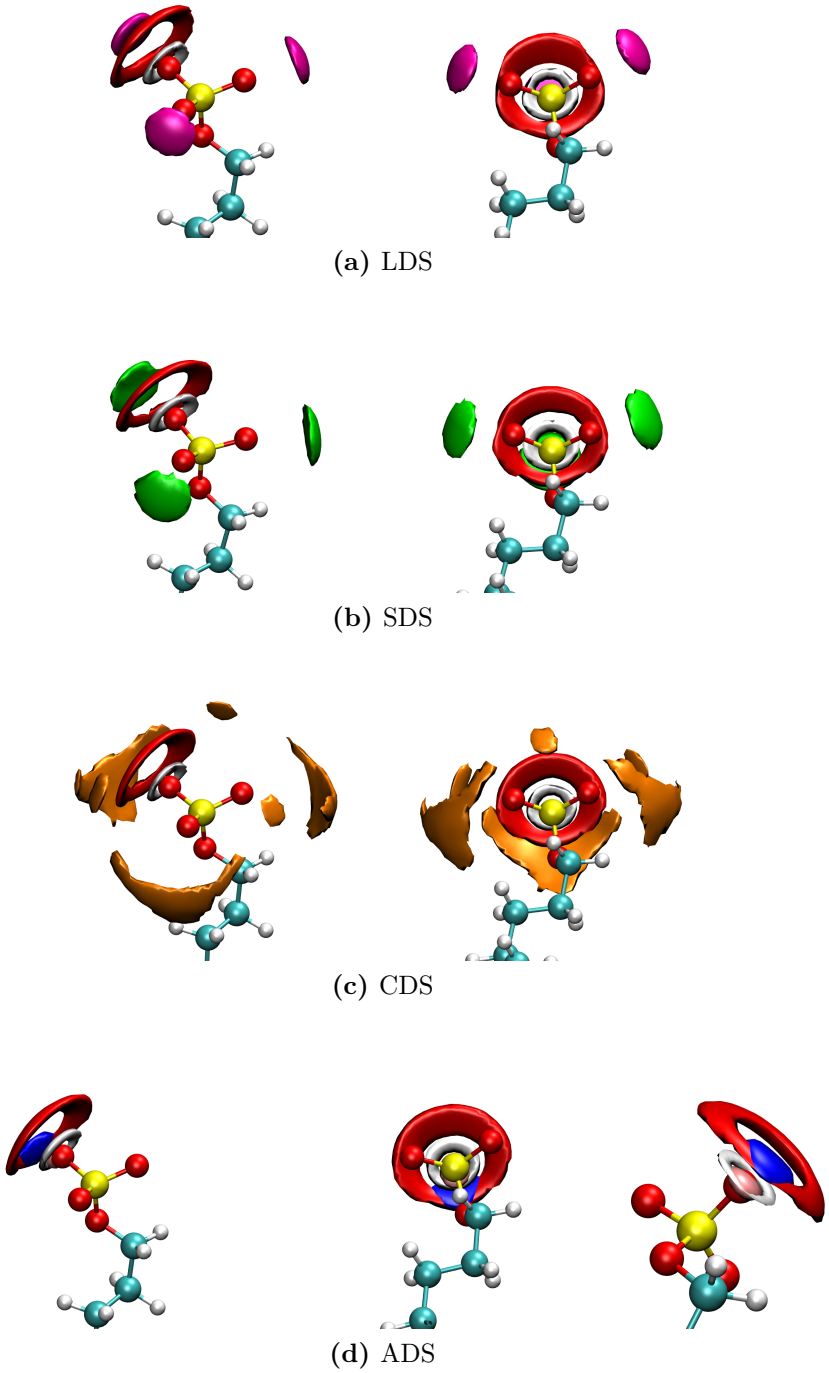

(a) LDS

(b) SDS

(c) CDS

(d) ADS

Fig. 4.8: Spatial density maps of the DS^- headgroups with the O_W (red SDMs), H_W (grey SDMs) and the (a) Li^+ ions (magenta SMDs), (b) Na^+ ions (green SDMs), (c) Cs^+ ions (orange SDMs) and (d) the N (blue SDMs) and H (pink SDMs) atoms in the NH_4^+ ions.

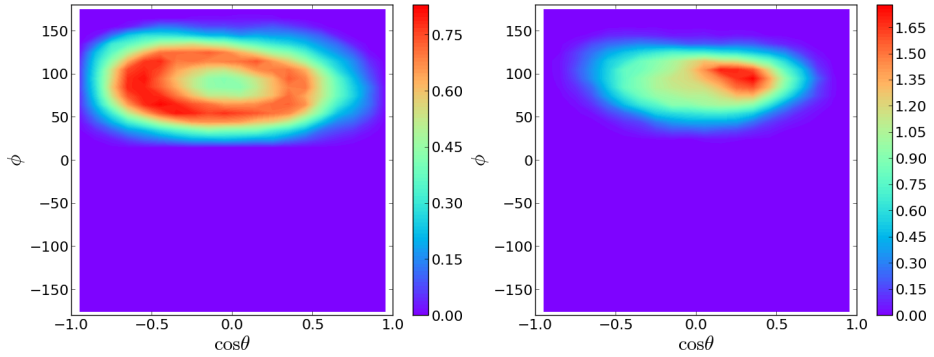

(a) Ow **(b)** N (NH_4^+)

Fig. 4.9: Bivariate probability density distributions of oxygen atoms in water molecules (a), and nitrogen atoms in ammonium ions (b) around the DS^- molecular axis. The contour scale bars in both plots represent probability density.

4.2.7 Salt Bridging of DS^- Headgroups

In order to quantify the number of counterions around a surfactant headgroup, the $g(r)$ between S_{DS} and counterions was measured and then the nearest neighbour distance was obtained in the same way as for the water molecules. In contrast to the hydration calculations, ions which are simultaneously interacting with multiple surfactants are of interest. This is an effect referred to as 'salt-bridging' in the literature.

The percentage of ions bound to the headgroup of the surfactant molecules p_{bound}, has been determined which can be used to find the degree of ionisation α by just calculating $1-(p_{\text{bound}}/100\%)$. The values of α found for the various systems reported are 0.3 (ADS), 0.32 (CDS), 0.45 (SDS) and 0.47 (LDS), which agree very well with those determined from electrical conductivity measurements of micellar solutions of similar systems, with the one exception in which the value for the LDS system reported here is slightly smaller than the experimental value (0.63 ± 0.07) [108]. Meanwhile, the α values found do not agree as well with the electrical conductivity measurements by Benrraou *et al.*,[111] but they do follow the same trend observed within their measurements ($\alpha(\text{CDS}) < \alpha(\text{SDS})$).

Salt-bridging was investigated by constructing histograms of the probability of

each different counterion species being bound to n surfactant headgroups through the duration of the production simulation runs, see Figure 4.10. For LDS and SDS, the probability of an ion interacting with n surfactants is monotonically decreasing with n. The corresponding histograms for CDS and ADS are distinctly different. First, a larger majority of the counterions in these systems are bound to at least one surfactant which is clear from the sharp decrease in $n = 0$ compared to the corresponding histograms for LDS and SDS. The probability of the Li^+, Na^+, Cs^+ and NH_4^+ ions being bound to at least one surfactant headgroup is 0.53, 0.55, 0.68 and 0.70 respectively. Second, there is an almost equal probability of a Cs^+ or NH_4^+ ion being bound to one or two surfactants. In fact, in the case of ADS, it is more probable for an ion to be interacting with two surfactant molecules than one. Additionally, ADS and CDS are approximately twice as likely to be bound to 3 surfactant headgroups as either LDS or SDS. There is also a non-negligible proportion of ions which are bound to 4 surfactant headgroups in all simulations. LDS has the smallest probability of this at 0.006, followed by SDS (0.02), CDS (0.03) and ADS (0.04). This indicates that salt-bridging is more prominent in the CDS and ADS systems than in LDS and SDS, which was also observed in the simulation study of LDS, SDS and ADS micelles carried out by Rakitin and Pack [112]. While the area per surfactant molecule has been kept constant in each of the simulated systems, this trend is consistent with the various studies that have found that the area per surfactant of ADS and CDS systems is smaller than those found for SDS and LDS systems [82, 83].

It has been established that all of the different counterion species exhibit salt bridging with ions bound to different numbers of surfactant headgroups with ranging probabilities. To see how this process changes for varying numbers of bound headgroups, if at all, distributions of Δz were calculated, that is the difference in the z-components of the position vectors of the counterion and S_{DS} atoms. The S_{DS}-Ion-S_{DS} angles were also calculated in conjunction with Δz to build a more detailed

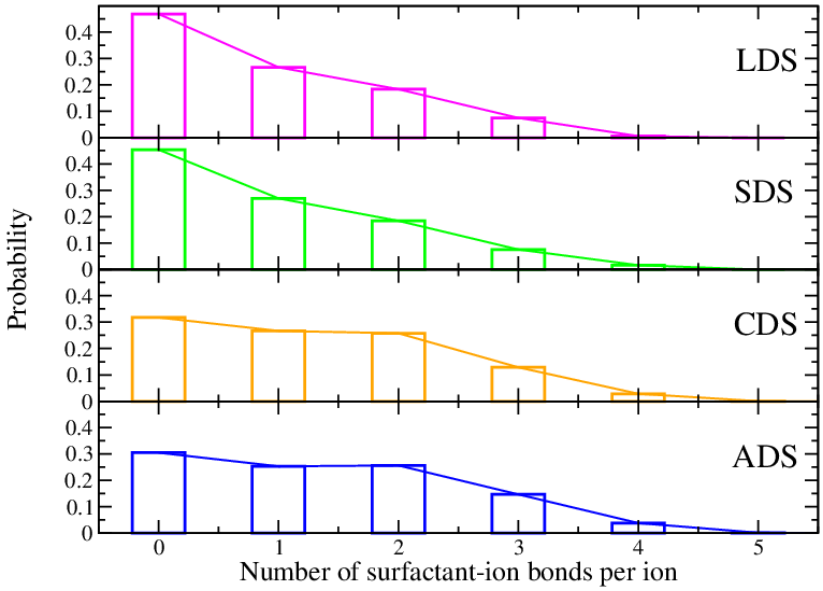

Fig. 4.10: Histograms showing the probability of an ion being bound to a given number of different DS^- headgroups.

picture of the salt bridging process. These distributions are shown in Figure 4.11.

For all simulations, there is a slight tendency for the Δz distributions to shift towards smaller values as the number of bound headgroups increases. This implies that for bridging events involving larger numbers of surfactant headgroups, the ion involved in the event is more likely to be situated level with the headgroups, with respect to the z direction, as opposed to being located towards the hydrocarbon tail region away from the bulk water. The S_{DS}-Ion-S_{DS} angle distributions are directly related to Δz and thus it follows that the observed shift in Δz towards smaller values results in a shift of the S_{DS}-Ion-S_{DS} angles towards smaller angles also. It must be emphasised that this is a very slight affect.

Figure 4.12 shows an example of an ammonium ion from the ADS simulation involved in a bridging event between three surfactant headgroups. The snapshot provides visual evidence that the NH_4^+ ions form hydrogen bonds with the O_{DS} atoms in the DS^- headgroup, which was also suggested by the SDMs that have been calculated (Figure 4.8).

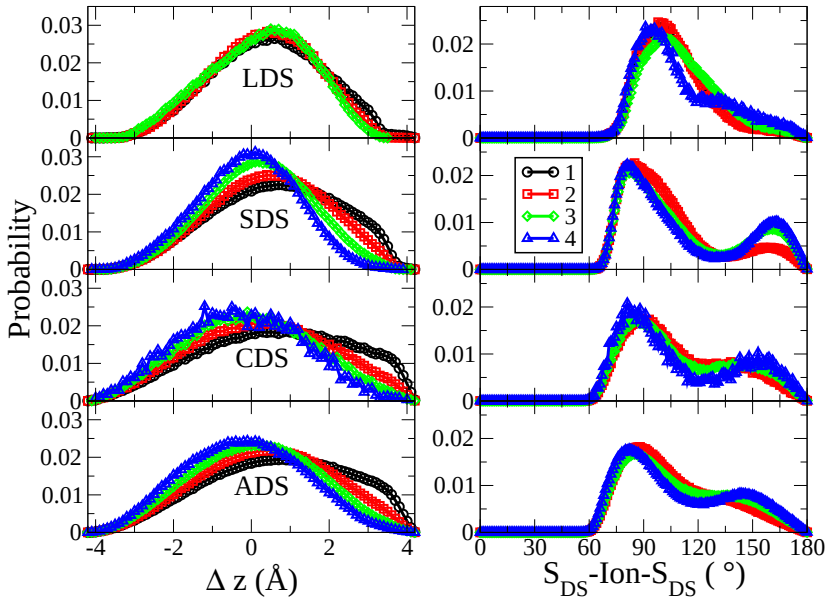

Fig. 4.11: Left: Probability distributions for Δz between sulphur atoms in DS^- and the counterions. Right: Probability distributions of the S_{DS}-Ion-S_{DS} angles. The colours black, red, green and blue are used to represent distributions obtained from salt bridging events involving 1,2,3 and 4 DS^- headgroups, respectively.

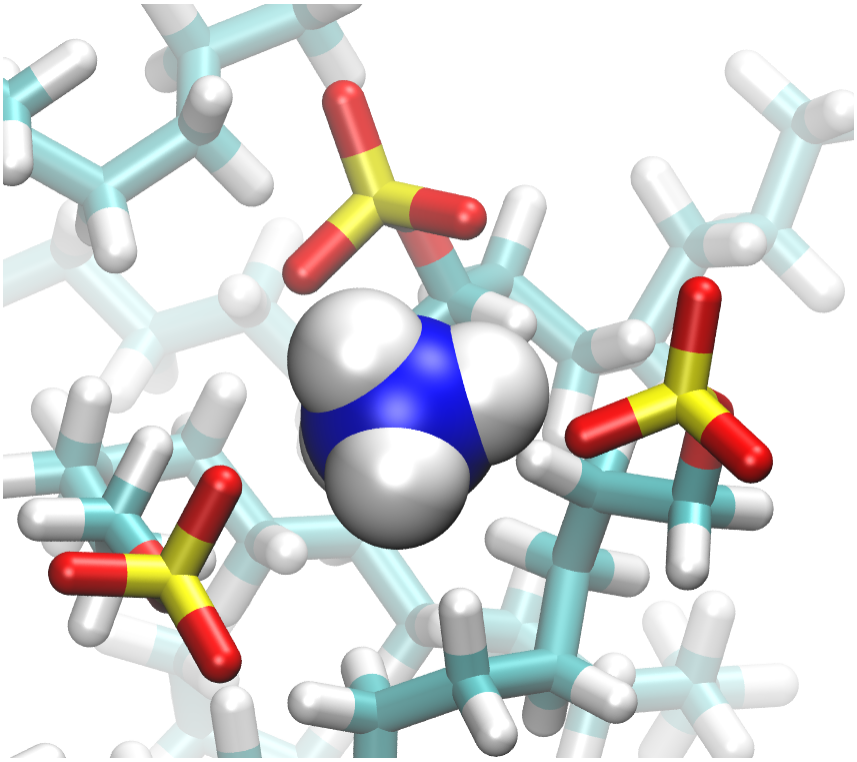

Fig. 4.12: Snapshot from the ADS simulation of a NH_4^+ ion bound to three different DS^- headgroups at one time. The colours cyan, grey, red, yellow and blue are used to represent the elements: carbon, hydrogen, oxygen, sulphur and nitrogen, respectively.

4.3 Conclusions

All-atom molecular dynamics simulations of DS^- surfactant monolayers at the air/water interface have been conducted with four different monovalent counterion species (Li^+, Na^+, Cs^+, NH_4^+) in order to determine how the structural and interfacial properties of the monolayers were affected.

In general, very little effect on the structure of the DS^- monolayers is observed from varying the counterion. However, significant differences are seen in the interfacial properties of the monolayers in the presence of the different counterions. When taking all of the results compiled in this chapter, the trend of the hydration of the DS^- headgroups in the presence of the various counterions can be explained via the following underlying mechanisms. In the ADS monolayers, the NH_4^+ ions directly compete with the hydrating water molecules for hydrogen bonds with the headgroup and in doing so cause these monolayers to be the least hydrated. In the case of the CDS system, the Cs^+ ions are strongly bound to the headgroup and are weakly hydrated, such that they would prefer to displace water in the DS^- hydration shell to interact with the headgroup. In the case of the Li^+ ions, they interact almost as strongly with the DS^- headgroups as the Na^+ ions, but are generally less hydrated than the Na^+ ions and therefore they bring less water to the monolayer interface than the Na^+ ions. There is a 1 water molecule difference in both the number of hydrating waters per cation and per DS^- headgroup in the two systems, so this seems to be the difference.

The variations in the interfaces that result from using the different counterions with the DS^- surfactants undoubtedly have significant implications on their ability to encapsulate solutes. One example of this is, as was mentioned in the Introduction, the results of some recent experimental work which show that ADS micelles have a poorer solubilisation capacity for encapsulating testosterone derivatives than SDS micelles, despite the fact that the ADS micelles have a larger aggregation number

and lower hydration [32]. Taking into account the results presented in this chapter, this could be due to strong interactions between the surfactant headgroups and the ammonium counterions. These interactions are strong enough to displace water molecules from the interface because of the ability of ammonium ions to form hydrogen bonds with the surfactant headgroups. Additionally, a significant increase in the salt bridging between the DS^- headgroups is seen when NH_4^+ ions are present than when Na^+ ions are, which would result in a stronger association between the headgroups at the micelle's surface.

The chemical structure of the poorly soluble molecule also plays a role in the ability to be solubilised within certain surfactant aggregates. For example, Kim *et al.* found that the solubilisation of pyrene in DS^- aggregates increases with increased aggregation numbers as the counterion is changed from Li^+ to Na^+ to NH_4^+ but the number of pyrene solubilised per surfactant molecule is only slightly increased [108]. Therefore in the next two chapters, a variety of different testosterone-based compounds interacting with SDS and ADS monolayers are investigated using molecular dynamics and well-tempered metadynamics simulations.

Chapter 5

Interaction of Testosterone-Based Compounds with Dodecyl Sulphate Monolayers at the Air-Water Interface

5.1 Introduction

In the previous chapter, dodecyl sulphate monolayers at the air/water interface were simulated in the presence of different counterions to investigate how the different counterions affect their interfacial properties. It was observed that ammonium counterions interact with the surfactant head groups via hydrogen bonds and this has a significant effect on the monolayer interfacial water structure. In this chapter, results are presented from both SDS and ADS monolayers interacting with three different testosterone-based compounds (testosterone (T), testosterone propionate (TP) and testosterone enanthate (TE)). For each distinct surfactant-drug pairing, numerous simulations have been performed varying the number of drug molecules present at each monolayer. The purpose of this work is to study the interaction of

these drugs with surfactant monolayers and also how the physical properties of the monolayers are affected by the presence of drug molecules. In particular, an understanding is developed of how the system behaviour is affected by: i) changing the counterion species, ii) changing the chemistry of the drug molecule and iii) changing the number of drug molecules present within the monolayer.

Whilst monolayers and micelles adopt planar and spherical geometries respectively, the knowledge gained through studying the interaction of testosterone-based compounds with surfactant monolayers is applicable to micelles as well as both of these aggregate structures provide a barrier between aqueous and nonpolar environments. Moreover, since monolayers and micelles coexist in dynamic equilibrium it is reasonable to equate the processes which occur within each structure.

5.1.1 Summary of Simulations

Results from twenty different simulations of surfactant monolayers are presented within this chapter, the technical details of which are explained in Chapter 3. The rationale behind the choice of the number of drug molecules, present in each system is as follows. Each surfactant-drug combination has been simulated with a single drug molecule present at each monolayer, this is to study how the drug interacts with the monolayer and affects physical properties in the absence of any neighbouring drug molecules. Additionally, monolayer systems have been simulated such that the ratio of the number of drug molecules, D, to the number of surfactant molecules, S: #D/#S, present is approximately equal to the composition of the corresponding micelle systems, as determined by neutron scattering experiments. Finally, monolayers have been simulated in which #D/#S is double that in the micelle systems, as determined by neutron scattering experiments. Therefore there are three different monolayer systems for each distinct surfactant-drug combination, with the exception of the combination of SDS and TE. The aggregation numbers obtained

from the micelle of this composition revealed a significantly larger #D/#S compared to the other SDS monolayer compositions. Therefore, two more simulations were performed with SDS and TE at one and two times the #D/#S value for the SDS monolayer with TP so that sensible comparisons could be drawn between the different systems.

In the remainder of this chapter, the monolayers are referred to by a systematic naming scheme which consists of the surfactant, followed by the drug, followed by the number of drug molecules present per monolayer. For example, the ADS monolayer interacting with 14 TP molecules is labelled as "ADS-TP-14".

5.2 Results

In this section, results are presented from a variety of different surfactant monolayers interacting with different testosterone-based compounds. The results of the properties which are explained in detail in Chapter 3 are summarised in Table 5.1 for all of the monolayer simulations.

Table 5.1: A table displaying average monolayer structural properties for all the surfactant monolayers reported. All quoted errors are standard deviations.

System	θ_t (°)	θ_h (°)	d_{tail} (Å)	d_{head} (Å)	Roughness (Å)	Hydration	n_{H_2O} (#/Å^{-2})
SDS-T-1	44.3 ± 20.8	44.8 ± 23.2	7.8 ± 0.2	2.2 ± 0.04	2.7 ± 0.2	8.3 ± 3.6	0.16
SDS-T-17	37.1 ± 19.4	41.8 ± 22.1	9.0 ± 0.2	2.2 ± 0.04	2.6 ± 0.2	8.0 ± 3.6	0.13
SDS-T-34	30.4 ± 16.5	38.4 ± 20.8	9.9 ± 0.2	2.2 ± 0.04	2.3 ± 0.2	7.7 ± 3.5	0.11
SDS-TP-1	39.5 ± 18.8	44.8 ± 23.1	7.9 ± 0.2	2.2 ± 0.03	2.7 ± 0.2	8.3 ± 3.6	0.15
SDS-TP-17	33.2 ± 16.3	41.8 ± 21.7	9.0 ± 0.2	2.2 ± 0.03	2.4 ± 0.2	7.9 ± 3.5	0.12
SDS-TP-34	26.4 ± 14.5	38.0 ± 20.4	10.1 ± 0.2	2.2 ± 0.03	2.5 ± 0.2	7.6 ± 3.5	0.10
SDS-TE-1	43.9 ± 20.8	44.8 ± 23.1	7.8 ± 0.3	2.2 ± 0.03	2.6 ± 0.2	8.2 ± 3.6	0.15
SDS-TE-17	35.1 ± 17.5	41.0 ± 21.3	9.2 ± 0.2	2.2 ± 0.03	2.4 ± 0.2	7.8 ± 3.6	0.11
SDS-TE-34	27.0 ± 14.7	36.6 ± 19.8	10.4 ± 0.2	2.2 ± 0.03	2.5 ± 0.2	7.5 ± 3.5	0.10
SDS-TE-41	24.2 ± 13.9	34.9 ± 19.4	10.8 ± 0.2	2.2 ± 0.03	2.6 ± 0.2	7.4 ± 3.5	0.09
SDS-TE-82	26.0 ± 20.0	32.3 ± 18.7	11.0 ± 0.4	2.2 ± 0.1	5.0 ± 0.5	7.6 ± 3.5	0.09
ADS-T-1	44.1 ± 20.7	44.7 ± 23.1	7.9 ± 0.2	2.2 ± 0.03	2.5 ± 0.2	6.5 ± 2.7	0.10
ADS-T-8	41.0 ± 20.2	43.3 ± 22.6	8.3 ± 0.2	2.2 ± 0.03	2.5 ± 0.2	6.4 ± 2.7	0.09
ADS-T-16	37.6 ± 19.2	42.1 ± 22.2	8.9 ± 0.2	2.2 ± 0.03	2.4 ± 0.2	6.3 ± 2.7	0.08
ADS-TP-1	43.7 ± 20.8	44.4 ± 23.0	7.9 ± 0.2	2.2 ± 0.03	2.6 ± 0.2	6.5 ± 2.8	0.10
ADS-TP-14	38.3 ± 18.7	42.4 ± 22.0	8.7 ± 0.2	2.2 ± 0.03	2.3 ± 0.2	6.2 ± 2.7	0.07
ADS-TP-28	31.6 ± 16.1	39.1 ± 20.6	9.7 ± 0.2	2.2 ± 0.03	2.3 ± 0.2	6.2 ± 2.8	0.05
ADS-TE-1	43.9 ± 20.8	44.7 ± 23.2	7.9 ± 0.2	2.2 ± 0.03	2.5 ± 0.2	6.5 ± 2.7	0.10
ADS-TE-22	32.6 ± 16.4	39.6 ± 20.7	9.6 ± 0.2	2.2 ± 0.03	2.3 ± 0.2	6.1 ± 2.7	0.06
ADS-TE-44	23.3 ± 13.4	34.2 ± 19.1	11.2 ± 0.2	2.2 ± 0.03	2.4 ± 0.2	5.7 ± 2.6	0.04

5.2.1 Monolayer Structure

The addition of testosterone-based compounds has an appreciable effect on the structural properties of surfactant monolayers. By developing a detailed understanding of this, the rationale behind enhancing the solubility of poorly soluble drug compounds within surfactant aggregates can be improved for formulations in the future.

The thickness of the monolayer headgroup region, d_{head}, was calculated for all systems and is found to be equal to 2.2 Å in all instances. This suggests that neither changing the counterion species, nor the presence of testosterone-based compounds has any effect on the conformation of the headgroups. Likewise, this result would indicate that the drug molecules are not interacting strongly with the headgroup regions. The monolayer chain thickness, d_{tail}, was calculated and plotted as a function of time. These plots (not shown) show small fluctuations around the mean values, illustrating that the monolayers were well equilibrated prior to the production simulations. The mean values of d_{tail} are shown in Table 5.1 and reveal the consistent trend without exception of increasing monolayer thickness with increasing number of drug molecules. Considering that as more drug molecules are added to the monolayer hydrocarbon tail regions within a fixed surface area, there is less area per molecule. Therefore the surfactant tails are restricted to more rigid configurations which results in an increase of the effective tail length.

The roughness was also quantified for all systems by calculating RMSD values, as described in Chapter 3, which for the most part yielded values in the range of 2-3 Å. This shows that the addition of testosterone-based compounds to the monolayers does not significantly compromise structural stability. The exception to this is SDS-TP-82 which is significantly more rough with an RMSD value of 5 Å. This monolayer is densely packed with TP molecules which has a severe effect on its structural integrity, as can be seen from visual inspection from the snapshot in Figure 5.1.

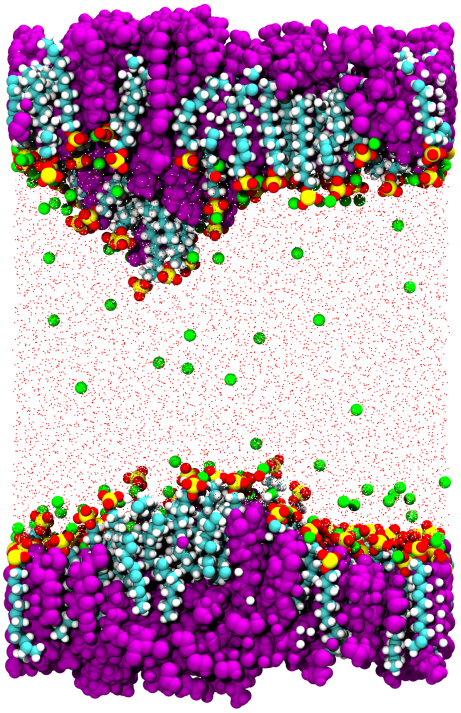

Fig. 5.1: A snapshot from the SDS-TE-82 production simulation illustrating the extreme roughness of this monolayer. The colours cyan, white, red, yellow and green are used to represent the elements: carbon, hydrogen, oxygen, sulphur and sodium respectively. The TE molecules are depicted in purple to distinguish them from the surfactants.

The surfactant chain tilt angle, θ_t, and headgroup tilt angles, θ_h, were calculated for all monolayer systems and their probability distributions are shown in Figure 5.2. From these plots it is clear that the addition of drug molecules causes the angle distributions to shift towards smaller angles for both θ_t and θ_h. This trend is also confirmed by the monotonically decreasing mean values of these distributions with the addition of more drug molecules as shown in Table 5.1. The behaviour of θ_t is easily explained as a result of spatial constraints restricting the flexibility of the surfactant chains. Similarly, the surfactant headgroups preferentially orient themselves towards the polar solvent medium and the reduction of area per molecule in the monolayer seems to restrict the fluctuations of this angle as well. The only exception to this trend is SDS-TE-82, which exhibits an increase in mean value of θ_t. The high packing density of molecules within the x-y plane results in increased mono-

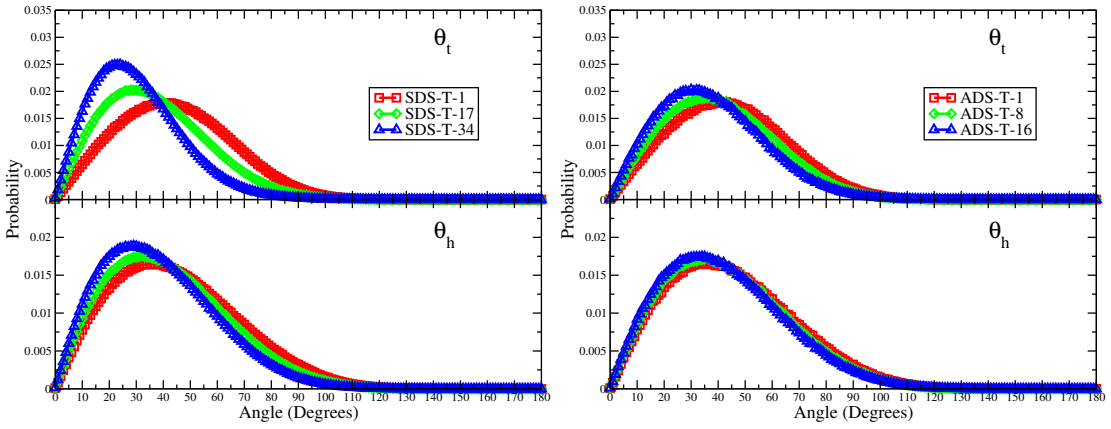

(a) SDS-T

(b) ADS-T

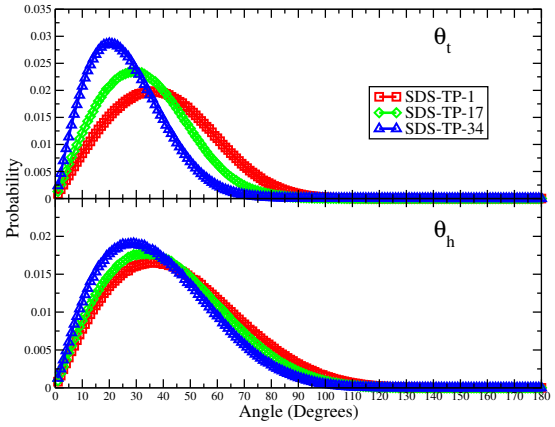

(c) SDS-TP

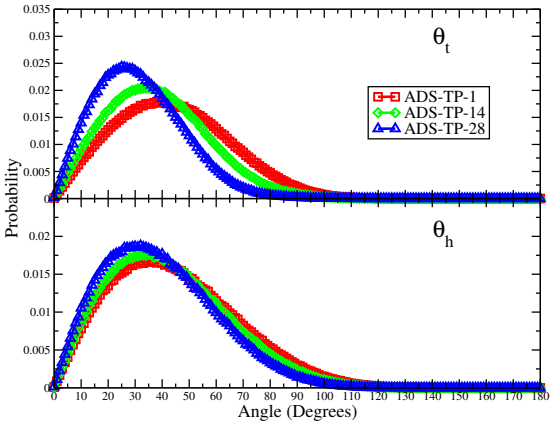

(d) ADS-TP

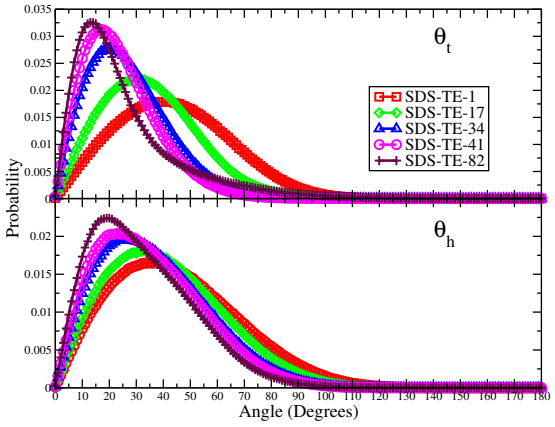

(e) SDS-TE

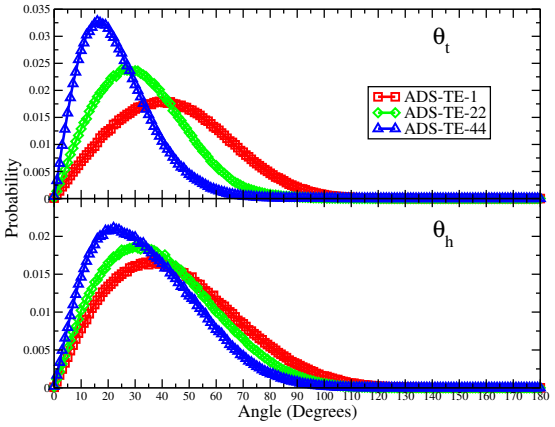

(f) ADS-TE

Fig. 5.2: Plots showing probability distributions of surfactant chain tilt, θ_t, and head-group tilt, θ_h, angles for all monolayer simulations. The plots correspond to the various different monolayer simulations reported, as described by the legends.

layer roughness, as seen from the RMSD values. This increased roughness causes the position of the surfactants to be more broadly distributed across the z-axis, effectively increasing the volume available to each surfactant tail. This seemingly permits slightly larger fluctuations in θ_t than for the SDS-TE-41 monolayer.

5.2.2 Monolayer Intrinsic Density

Intrinsic density profiles are useful for comparing monolayer structure for the various different systems presented in this chapter. In particular, they enable the detailed characterisation of the interfacial water structure and the location of testosterone-based compounds within the monolayers. The comprehension of these properties permit the understanding of interactions in atomic detail.

Intrinsic density profiles were calculated for all of the monolayer simulations using a resolution of 0.5 Å and are shown in Figure 5.3. One significant distinction between these plots for SDS and ADS monolayers is the density profiles of oxygen atoms in water molecules, O_W, as shown by the blue curves in Figure 5.3. At large values of z, corresponding to regions in the bulk water, the density of O_W atoms converges to 0.033 Å^{-3} in all systems which is equal to the target bulk density of water at 1 g/mL. At smaller values of z, corresponding to the monolayer interfacial region, the SDS monolayers exhibit two distinct density peaks. The largest peak is situated at $z = 3.5$ Å whilst the smaller peak is located at $z = 6$ Å which indicates that there are interfacial water layers in the SDS headgroup region. For the ADS monolayers, the structure of water molecules in the interfacial region is quite different. Rather than exhibiting peaks, the density of O_W atoms remains constant at the bulk value and it begins to decrease monotonically from the headgroup region, some distance inside the monolayer hydrocarbon tail region ($z < 0$). This suggests that the water is less ordered at the ADS monolayer interface than SDS. This is consistent with the results presented in Chapter 5 where monolayers with different

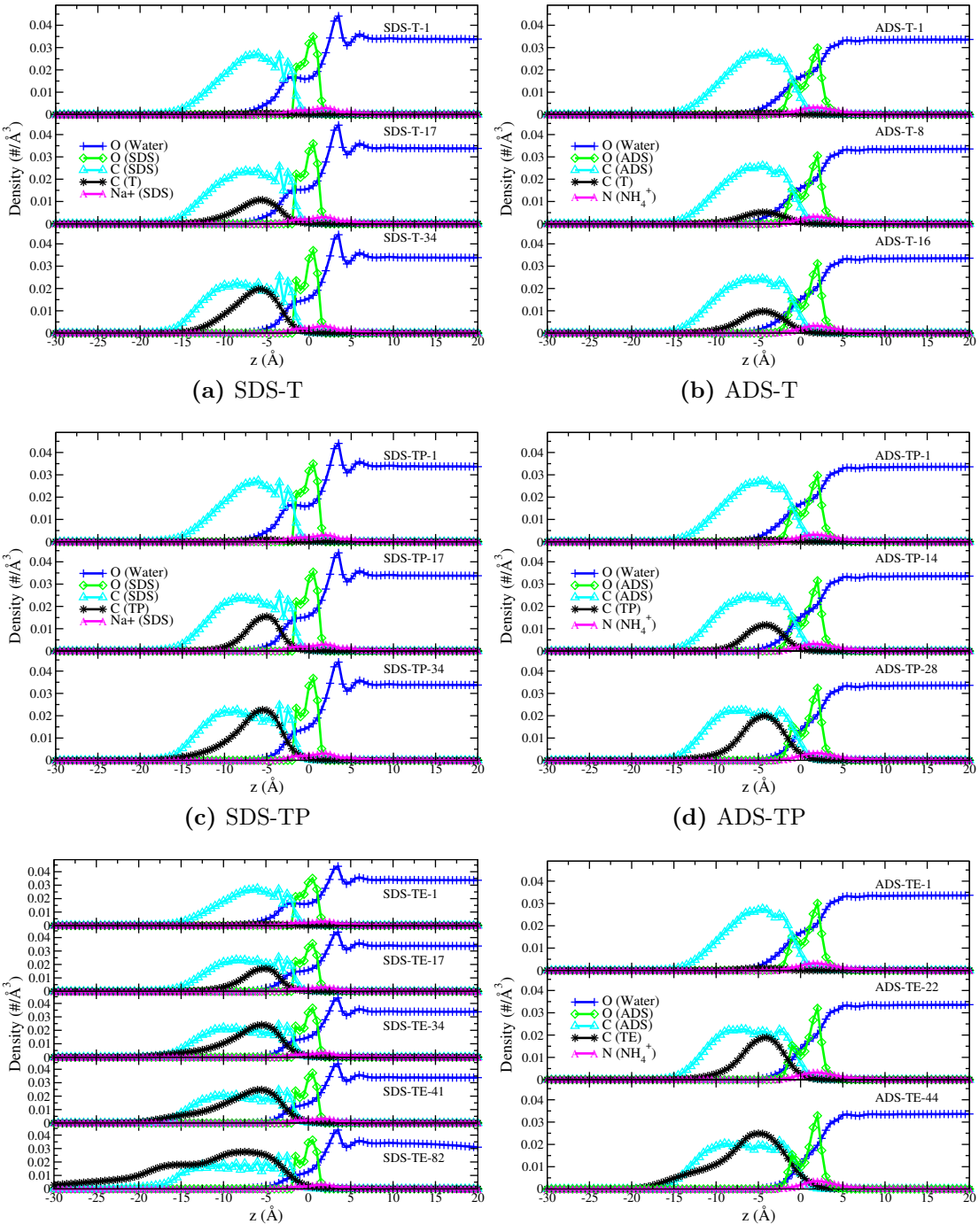

(a) SDS-T **(b)** ADS-T

(c) SDS-TP **(d)** ADS-TP

(e) SDS-TE **(f)** ADS-TE

Fig. 5.3: Intrinsic density profiles for the monolayer simulations. The colours green, blue and magenta are used to depict the density of DS^- elements: oxygen, carbon, and sodium/nitrogen in the counterions respectively. The colours blue and black are used to depict the density of oxygen atoms in water and carbon atoms in the testosterone-based molecules respectively.

counterions were compared in the absence of drug molecules. The effect of changing the testosterone-based compound, or the number of drug molecules present within the monolayers has negligible effect on the interfacial water density compared to changing the counterion species which has a very large effect. This provides further support that the drug molecules seldom interact with the surfactant headgroups in any of the simulations.

Within the monolayer hydrocarbon tail region, $z < 0$, the water density decays and eventually reaches zero in all systems. For the SDS monolayers with 1 drug molecule present, there is a small peak in the density of the O_W atoms located at approximately $z = -3$ Å. For the SDS systems, this water density peak within the monolayer becomes less prominent as more drug molecules are present, suggesting that the addition of drug molecules results in the expulsion of water from the monolayer tail region. None of the ADS monolayers seem to have appreciable density peaks for O_W atoms within the monolayers which could mean that there is less water present within the ADS monolayers in general. To quantify this, the property n_{H_2O} was calculated for all systems by integrating the intrinsic density of O_W atoms over z from $-\infty \rightarrow 0$, leading to a measure of the average number of water molecules contained within the monolayer interior per unit area. The values for n_{H_2O} are shown in Table 5.1 and reveal that as the number of drug molecules present per monolayer increases, the value of n_{H_2O} decreases for all surfactant-drug pairings. As the monolayers become more densely packed by the addition of drug molecules, water is forced into the bulk water slab where it can form more favourable interactions than in the monolayer tail region. The ADS monolayers do in fact contain significantly less water within their tail regions. For example, the values of n_{H_2O} for SDS-T-1 and ADS-T-1 are 0.16 Å^{-2} and 0.10 Å^{-2} respectively. Similarly, comparing SDS-TP-1, SDS-TE-1 and ADS-TP-1, ADS-TE-1 reveals n_{H_2O} values of 0.15 Å^{-2} and 0.10 Å^{-2} for SDS and ADS respectively. Therefore by changing the counterions from sodium to ammonium, the water contained within the monolayer decreases

by 33% which is significant. The amount of water contained within the interior of surfactant aggregates could have a profound effect on their resulting solubilising ability.

The intrinsic density profiles of the sodium and ammonium counterions are shown by the magenta curves in Figure 5.3 and exhibit a single broad density peak around the monolayer interface ($-5 < z < 5$) in all systems. This suggests that they are situated in the vicinity of the interfacial region, which is also confirmed from visual inspection of the simulation trajectories.

The green curves in Figure 5.3 show the intrinsic density of oxygen atoms in DS^- molecules, O_{DS}, for all of the monolayers. For the SDS monolayers with a small number of drug molecules present, these distributions exhibit a peak located at $z = 0$ Å, and a shelf located just beneath the monolayer surface at $z \sim -1$ Å. As the number of drug molecules is increased, this density distribution splits into two distinct peaks, the largest of which corresponds to the three ionic oxygen atoms in the surfactant head group, whereas the second smaller peak arises due to the oxygen atom which is bonded to the C_1 and S atoms in the surfactant molecules. As more drug molecules are added, the dynamics of the head groups becomes restricted which results in the increased prominence of the two density peaks of O_{DS} atoms. In the ADS monolayers, the O_{DS} intrinsic density profiles show even sharper peaks than those in SDS, however unlike the SDS monolayers, these peaks are unchanged by the addition of more drug molecules. This also suggests that the counterion species is the predominant factor in determining the structure of the monolayer interface, as opposed to the details of the testosterone-based compounds such as the species and the number of drug molecules present.

The intrinsic density profiles of carbon atoms in DS^- molecules, C_{DS}, are shown by the cyan curves in Figure 5.3 and represent the surfactant hydrocarbon chains. These density profiles are non-zero in the region from the monolayer interface ($z \sim 0$) to approximately $z = -15$ Å for all of the SDS and ADS monolayer simulations

except SDS-TE-82 due to the extreme packing of TE within the monolayer, resulting in the increased thickness as discussed above. There is no significant change in the C_{DS} intrinsic density profiles as the counterion species is changed, however as the number of drug molecules present in the monolayer increases, the C_{DS} density profile flattens out to some extent. This effect is most clearly illustrated in the SDS-TE simulations as the number of TE is increased from 1 to 82. This is a direct result of the shift in the distributions of θ_t towards smaller angles which is discussed earlier in this section.

Given that the majority of the testosterone-based compounds molecular weight consists of carbon atoms, it seems reasonable to describe the position of these drug molecules in the monolayers by calculating the intrinsic density of these carbon atoms: C_T, C_{TP} and C_{TE} for T, TP and TE respectively. The intrinsic density profiles of the carbon atoms in the testosterone-based compounds are shown by the black curves in Figure 5.3 and show that these molecules are located amid the DS^- hydrocarbon tails and not at the interface. As more drug molecules are added, the density peaks remain in approximately aroud the same value of $z \sim -5$ Å whilst the magnitude of the peaks increase slightly to accommodate the additional drug molecules present. The SDS-TE-82 simulation is useful for examining extreme over packing of drug molecules within a monolayer and in this case, the C_{TE} density in the hydrocarbon tail and vacuum regions increases. This suggests that the preferable place for TE to reside in the monolayer gets saturated and any additional drugs added are expelled to the vacuum region rather than into the bulk water.

5.2.3 Orientation and Position of Testosterone-Based Compounds in Monolayers

The intrinsic density plots reveal that the testosterone-based compounds are generally situated within the DS^- hydrocarbon tail region. However they do not contain

any information about the orientation of these molecules at different positions within the monolayer, nor do they provide any specific detail about the drug location in reference to the surfactant molecules. The intrinsic drug orientation was described earlier in Chapter 3 with the aid of Figure 3.7, which clearly shows the Headgroup, C_{1-4}, C_{5-8} and C_{9-12} regions of the monolayer. These distributions are presented in Figure 5.4 and show the drug orientation distributions as a function of distance from the intrinsic surface for the monolayer simulations. One prominent difference between these distributions is that T appears to sample a wider range of orientations compared to TP and TE, as shown by the relatively flat distributions across $\cos\theta$ in Figures 5.4a and 5.4b. Additionally, the T molecules occupy both the C_{1-4} and C_{5-8} regions in the monolayers with just a single T molecule. However, as more T molecules are added to the monolayers, the C_{5-8} region becomes more densely populated and the drug molecules also tend to reorient themselves such that their O2 and O1 atoms are nearest the vacuum region and water slab, respectively.

The TP molecules strongly populate the C_{1-4} region of the monolayers, with a distribution centred at $cos\theta \sim 0.3$ which corresponds to the TP molecules being oriented approximately in the x-y plane within this part of the monolayer. This is shown clearly by the prominent green curves in Figures 5.4c and 5.4d. For both the SDS-TP and ADS-TP monolayers, as more TP molecules are introduced to the system, the C_{5-8} region becomes more populated and exhibits peaks at $\cos\theta = 0.9$ corresponding to the TP molecules reorienting themselves such that their O1 atom is in contact with water in a similar way as for the T molecules.

The TE molecules also occupy the C_{1-4} region and exhibit the same shift of population to the C_{5-8} region as the number of TE per monolayer is increased sufficiently. The SDS-TE-41 and SDS-TE-82 systems show examples of monolayers which are extremely packed with TE, which results in an even larger population shift from the C_{1-4} to C_{5-8} regions than that for T and TP. Furthermore, SDS-TE-82 shows a non-negligible occupancy of the C_{9-12} region, with a probability

distribution which is heavily skewed towards large values of $\cos\theta$ as is observed for the C_{5-8} region.

The rationale of these results comes from considering the competing forces at play within these monolayers. For the testosterone-based molecules with an ester functional group, and therefore highly polar interaction sites at both ends of the molecule (TP and TE), orientations with the drug molecule being parallel to the x-y plane will be preferable. This ensures that hydrogen bonds can be formed between water molecules and these polar sites within the drug molecule. For these hydrogen bonds to be formed, the drug molecule must have some contact with water molecules which explains why they sit in the C_{1-4} region which is close to the headgroups and ensures some contact with water, but also allows for the drugs to form hydrophobic contacts. As more drug molecules are packed into the monolayers within a fixed surface area, they are forced to reside in the monolayer regions further away from the surfactant/water interface and reorient themselves towards a configuration in which they are approximately parallel to the z-axis. The mechanism behind this reorientation is two-fold: first, the steric interactions become significant as packing increases. Second, reorienting the drug molecules in this manner permits favourable interactions between the water molecules and the O1 atom in the drug molecules, whilst the nonpolar carbon chain in the ester functional group (containing the O2 and O3 atoms) is situated away from the water slab towards the vacuum region.

5.2.4 Effect of Testosterone-Based Compounds on Interfacial Hydration Properties

To investigate how the presence of testosterone-based compounds affects the hydration of the DS^- head groups, distributions of the surfactant hydration number were produced (as explained in Chapter 3). The histograms of the average hydration number for each monolayer simulation exhibit unimodal distributions centred

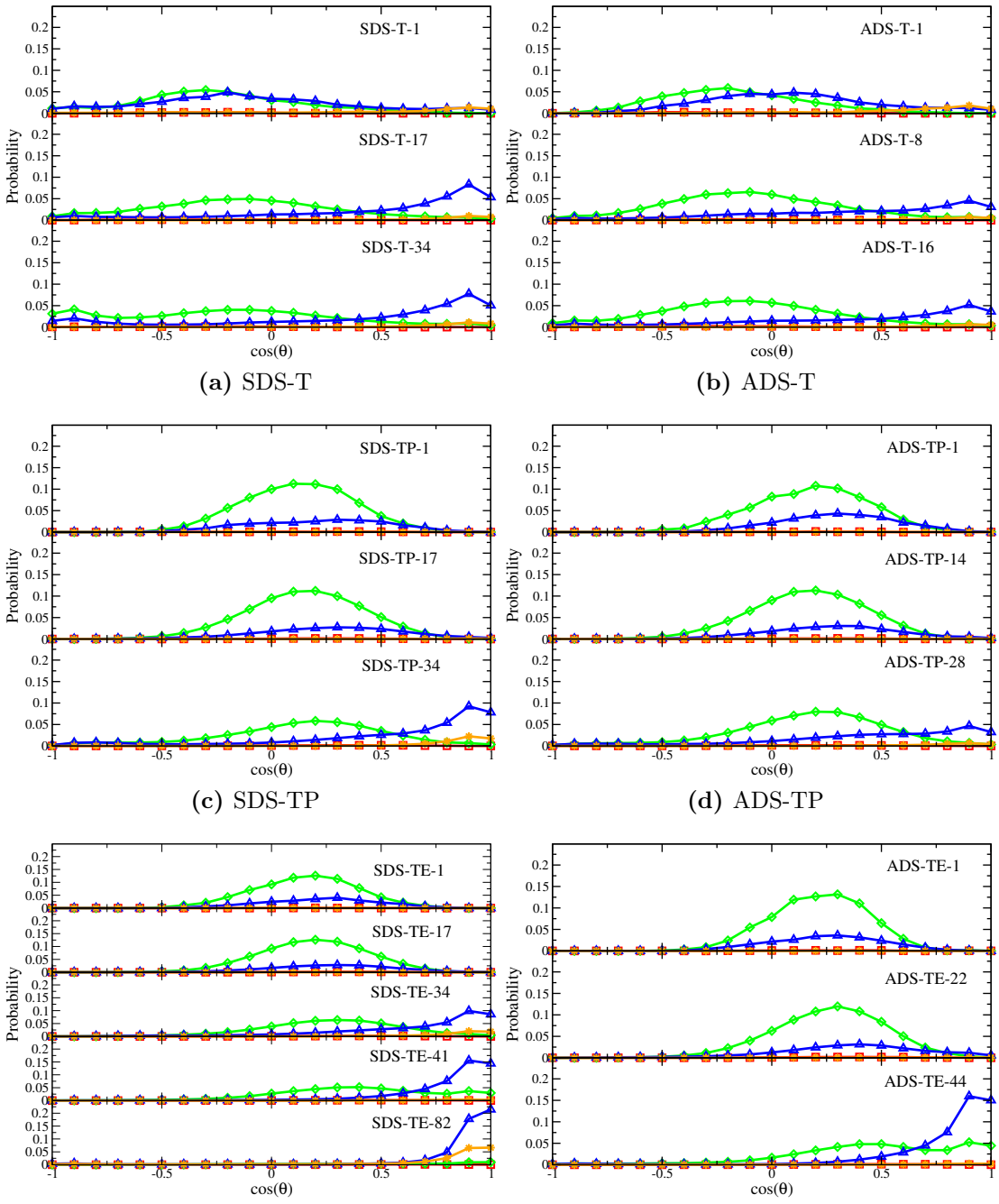

(a) SDS-T **(b)** ADS-T

(c) SDS-TP **(d)** ADS-TP

(e) SDS-TE **(f)** ADS-TE

Fig. 5.4: Intrinsic drug orientation distributions for the various different monolayer simulations. The monolayer system is labelled in each subplot. For all plots, the colour scheme is consistent with the diagram in Figure 3.7 in that the colours red, green, blue and orange represent the Headgroup, C_{1-4}, C_{5-8} and C_{9-12} regions respectively.

around the mean value (not shown). The mean hydration number of each monolayer simulation is shown in Table 5.1. Comparing these values reveals that the SDS monolayers are more hydrated than ADS, for example in the simulations with a single drug molecule present the hydration decreases from ∼8.3 H_2O/molecule for SDS, to 6.5 H_2O/molecule for ADS systems. The probability distributions do not change drastically when the number of drug molecules per monolayer is varied, however the mean hydration number does decrease slightly as the number of drug molecules per monolayer is increased, except for the case of SDS-TE-82 which has a larger mean hydration number than SDS-TE-41. This is attributed to the increased monolayer roughness which results in an increase of the surface area of surfactant head groups exposed to the solvent. Once again, the counterion species seems to be the dominant factor in determining hydration.

5.3 Conclusions

In this chapter, results have been reported from MD simulations of both SDS and ADS monolayers interacting with three different testosterone-based compounds (testosterone (T), testosterone propionate (TP) and testosterone enanthate (TE)) with varying numbers of these drug molecules present in the monolayers. The purpose of these simulations is to gain an understanding as to how the structural and interfacial properties of the monolayer are affected by changing the number of drug molecules present per monolayer, and the chemical nature of the surfactant counterions and the testosterone-based compounds.

The hydration of the surfactant headgroups was investigated by calculating the probability distributions of the surfactant hydration number. These revealed that the SDS monolayers are significantly more hydrated than the ADS monolayers, a feature which could be responsible for the observed disparity in the encapsulation ability of SDS and ADS micelles, the latter exhibiting poorer encapsulation ability

compared to the former despite the comparable size of these micelles. Additionally, these distributions showed that the surfactant hydration numbers decrease slightly as the number of drug molecules present per monolayer is increased.

Measuring the monolayer structural properties revealed that the monolayer headgroup thickness, d_{head}, remains constant in every monolayer system reported. The thickness of the hydrocarbon tail region, d_{tail}, increases as more drug molecules are added to the monolayer due to packing constraints but does not differ significantly as the testosterone-based compound is changed. Furthermore, the roughness measurements were found to decrease slightly with the addition of a small number of drug molecules, due to the increased monolayer ordering, however further addition of drug molecules induces an increase in the monolayer roughness, an effect which is particularly prominent in SDS-TE-82. Distributions of the surfactant chain tilt, θ_t, and headgroup tilt angles, θ_h, shift towards smaller values as more drug molecules are added to the monolayers, an effect which is coupled with the observation of increased monolayer thickness.

The intrinsic density profiles revealed that there is a distinctly different interfacial water structure for the SDS and ADS monolayers, with the former exhibiting ordered interfacial water layers whilst the latter shows a density profile which decays monotonically into the monolayer hydrocarbon tail region. Moreover, the SDS monolayers contain approximately 50% more water than the ADS monolayers as revealed from the $n_{\text{H}_2\text{O}}$ values, which also decrease slightly as more drugs are added into the monolayers. The intrinsic density profiles also reveal that the testosterone-based compounds are located within the hydrocarbon tail regions, predominantly within the C_{1-4} region. The intrinsic drug orientation distributions show that as more drugs are added, the population of drug molecules begins to shift higher up in the monolayer tails. The drug molecules located in the C_{5-8} and C_{9-12} regions reorient themselves such that they are approximately parallel to the z-axis in order to form hydrogen bonds between their O1 atoms and water molecules. This effect

is more pronounced for TP and TE due to the ester functional group, than for T.

The intrinsic drug orientation distributions are useful for gaining a rough idea of the orientation behaviour of the testosterone-based compounds at different positions in the monolayers, however they are limited by the sampling available during the simulation time period. In the next chapter, results are presented from metadynamics simulations of testosterone-based compounds interacting with SDS monolayers. From these simulations, the free energy landscape is constructed as a function of the drug orientation, and depth of insertion into the monolayer to build a more detailed picture of these interactions.

Chapter 6

Free Energy Surface of Testosterone-Based Compounds Interacting with Sodium Dodecyl Sulphate Monolayers

6.1 Introduction

In the previous chapter, the interaction of testosterone-based compounds within surfactant monolayers was investigated using classical molecular dynamics simulations. The intrinsic drug orientation and intrinsic density profiles revealed that all three of the testosterone-based compounds preferentially reside within the surfactant tail regions of the monolayers. The locations of the drug molecules remained stable throughout the simulation trajectories which suggests that they were located at a local minimum in the system's free energy surface (FES). As was discussed earlier in Chapter 2, MD simulations are usually unable to sample rare events due to the challenges in obtaining sufficiently long trajectories for large molecular systems. The implication of this is that a system modelled in MD will likely only sample a small

range of its FES, as it may be unable to cross free energy barriers between stable free energy states. It is desirable to understand the global FES associated with the interaction between the testosterone-based compounds and the monolayers, which cannot be sampled in regular MD simulations. Even though the drug molecules were found to be stable at a local minimum within the monolayers, it may be that they could lower their free energy further if they were able to overcome an energy barrier and reach the global minimum. Furthermore, the preferred location of the different testosterone-based compounds within the monolayers could be the same whilst the depth of the corresponding free energy wells differ, resulting in varying stability of these drugs within monolayers which is not easily measured from MD simulations for the reason of limited sampling as described above.

There are instances in the literature of free energy calculations concerning the formation of surfactant micelles [125, 126] and one example of a study of the free energy of penetration of both a methane molecule and a water molecule into an SDS micelle as a function of the radial distance to the micelle centre of mass using the thermodynamic integration method [127]. However, there are currently no published studies of the free energy of hydrophobic solutes interacting with surfactant monolayers specifically. There are studies of the permeation of solutes into lipid bilayers using methods such as well-tempered metadynamics, adaptive biasing force [128] and umbrella sampling [129, 130] in the literature. However, these study the interaction as a function of the distance from the centre of mass of the solute to the centre of the bilayer which once again does not take capillary wave fluctuations into account, and thus provides a smeared description of the permeation process.

In this chapter, well-tempered metadynamics simulations are reported which estimate the free energy of permeation of testosterone-based compounds within SDS monolayers, thus gaining further insight into the interactions between testosterone-based compounds and SDS monolayers which were studied in the previous chapter (in the systems SDS-T-1, SDS-TP-1 and SDS-TE-1).

6.2 Methods

Metadynamics calculations have been performed to obtain the FESs of SDS monolayers in the presence of three different testosterone-based compounds: testosterone (T), testosterone propionate (TP) and testosterone enanthate (TE). These systems will be referred to as T, TP and TE throughout the remainder of this chapter. The initial system configurations for these calculations were provided from the final state of SDS monolayer MD simulations in the presence of a single testosterone-based compound, which were reported in the previous chapter. In addition to the convenience of using these configurations that did not require any time to build, another reason why these configurations were used is that they provide low energy states from the end of their respective production simulations as starting states, which did not require any energy minimisation.

All metadynamics simulations were performed using the LAMMPS simulation package [70] patched with the PLUMED2 metadynamics plugin [131]. These simulations were conducted in the NVT ensemble at T = 300 K with the CHARMM force field [71, 72] for the description of both inter- and intra-molecular interactions of the SDS molecules, the sodium counterions and also the testosterone-based compounds [73, 74]. The TIP3P water model [65], which was modified for the CHARMM force-field [66], was used to describe interactions involving water. The van der Waals interactions were cut-off at 10 Å whilst the electrostatic interactions were cut-off at 12 Å. The PPPM method [49] was used to compute long-range Coulombic interactions. The monolayer simulations utilised the Nose-Hoover thermostat [77] to fix the system temperature. A timestep of 2 fs was used in all simulations to ensure stable integration of Newton's equations of motion with the *velocity Verlet* algorithm whilst all hydrogen-containing bonds were constrained using the SHAKE algorithm [56].

The dynamics of the systems were biased as a function of two collective variables

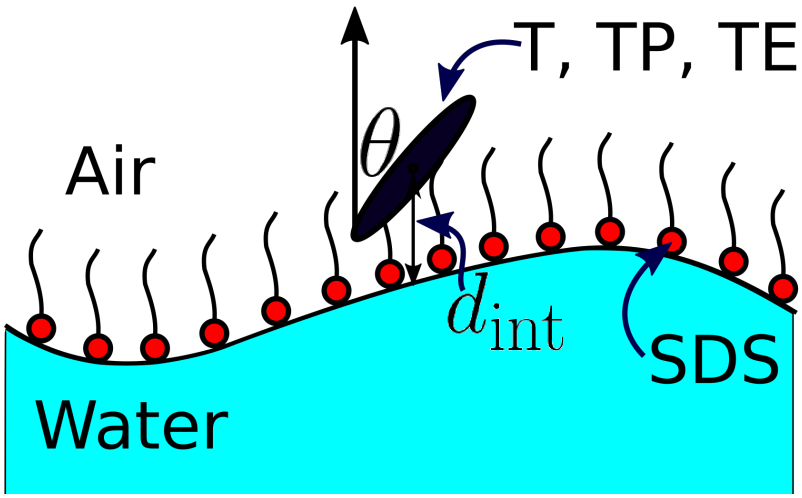

Fig. 6.1: A schematic diagram illustrating the collective variables used in the well-tempered metadynamics simulations reported in this chapter: d_{int} and $\cos\theta$. The z-axis is labelled, with which the angle, θ, is measured in reference to. The surfactant head groups and a testosterone-based compound are depicted in the colours red and blue respectively.

(CVs) (shown schematically in Figure 6.1): i) the orientation of the drug molecule with respect to the z-axis, $\cos\theta$ and ii) the distance from the centre of mass of the drug molecule to the monolayer intrinsic surface, denoted by d_{int}. It should be noted that positive and negative values of d_{int} correspond to the drug molecule being situated in the bulk water phase and within the monolayer tail region respectively. The first CV is straightforward to calculate and is naturally periodic. If the vector pointing from the O1 atom to the O2 atom in a drug compound is denoted by $\mathbf{V}^{\mathrm{ori}} = (\mathbf{V}^{\mathrm{ori}}_x, \mathbf{V}^{\mathrm{ori}}_y, \mathbf{V}^{\mathrm{ori}}_z)$, then the cosine of the angle between this vector and a unit vector in the z-direction is given by $\cos\theta = \mathbf{V}^{\mathrm{ori}}_z/|\mathbf{V}^{\mathrm{ori}}|$, namely the z-component of the vector divided by the magnitude of the vector. When $\cos\theta$ is equal to -1, the entire drug molecule is aligned parallel to the z-axis with the O1 atom nearest the vacuum region and the O2 atom nearest the water slab, when $\cos\theta$ is equal to 0 the drug molecule is oriented in the x-y plane and when $\cos\theta$ is equal to 1, the drug molecule is again aligned parallel to the z-axis but with the O2 atom nearest the vacuum region and the O1 atom nearest the water slab.

Previously in Chapters 4 and 5, the intrinsic surface of a monolayer sheet was

calculated using the method of Berkowitz *et al* [81] as this has been shown to give consistent results with other methods. This surface description cannot be used in metadynamics calculations however as it produces a discontinuous function. Specifically, when one moves in the $x-y$ plane to a position which is equidistant between two anchor points, the surface height jumps very suddenly from the z-coordinate of one anchor to that of the other. Therefore in metadynamics, an interpolation between anchor points must be used. A weighted average of the z-coordinate of the surface anchor points (the sulphur atoms in surfactant head groups) has been used in this work. The anchor points are again projected into the $x-y$ plane and the distance from the centre of mass of a testosterone-based compound to the intrinsic surface of the monolayer is given by:

$$d_{\text{int}} = r_z - \frac{\sum_{i=1}^{N} \exp\left[-\lambda(\Delta x_i^2 + \Delta y_i^2)\right] \cdot \Delta z_i}{\sum_{i=1}^{N} \exp\left[-\lambda(\Delta x_i^2 + \Delta y_i^2)\right]} \tag{6.1}$$

where r_z is the z-coordinate of the centre of mass of the drug molecule, $\Delta x_i, \Delta y_i$ and Δz_i are the x, y and z components respectively of the vector connecting the i^{th} anchor point to the centre of mass of a drug molecule, the summation runs over all N anchor points used to construct the surface and λ is a free fitting parameter which determines how smooth the fitted surface is. For example, when $\lambda = 0$ the exponents in Equation 6.1 will also be equal to 0 and thus the weighting factors will be equal to 1. Then the intrinsic surface will simply be given by the mean value of the z-coordinates of the anchor points, which is uniform in the $x-y$ plane. Such a function has a vanishing derivative for all (x, y) and therefore is a flat plane which constitutes a poor description of the monolayer/water interface. As the value of λ is increased, the surface function will become progressively less smooth but will pass through an increasing number of anchor points. As $\lim_{\lambda\to\infty}$, the surface function will tend towards a Voronoi diagram where the height of the surface at point

(x, y) takes the value of the z-coordinate of the closest anchor point in the $x - y$ plane. The value of λ is chosen such that the surface produced will pass through the anchor points, but not have large gradients at any point which ensures that the collective variable doesn't jump discontinuously from one value to a drastically different one between time-steps in the dynamics calculations. By visual inspection of the intrinsic surface constructed, one can assess how well a particular value of λ describes the monolayer/water interface by considering the criteria outlined above. After experimentation, it seems that $\lambda = 0.75$ provides a good fit of the surface to the anchor points, without the presence of discontinuities in the surface function, for the monolayers presented in this chapter. The value of λ could be determined systematically by calculating the $g(r)$ curve between anchor points in the x-y plane and then defining λ in terms of the nearest neighbour distance, d_{nn}, obtained from the $g(r)$ curve: $\lambda = 1/d_{\mathrm{nn}}^2$.

The initial height of the Gaussians was set to 0.3 kJ/mol whilst the stride at which the Gaussian hills were deposited was set to once every 500 integration time steps. The widths of the Gaussian hills for each CV, σ, were chosen systematically by calculating the absolute value of the change in the CVs, Δd_{int} and $\Delta \cos\theta$, within the time period $t \rightarrow t + \mathrm{stride}$. These calculated quantities were used to produce probability histograms as shown in Figure 6.2. The mean values of $|\Delta d_{\mathrm{int}}|$ and $|\Delta \cos\theta|$ were calculated from these distributions and were taken to correspond to 2σ. Therefore, the σ values used in the metadynamics simulations for d_{int} and $\cos\theta$ were 0.2 Å and 0.32 respectively. Upper and lower walls were set on the d_{int} CV at the values of 20 Å and -30 Å respectively to prevent the drug molecules from sampling irrelevant regions of the simulation box, such as those in the vacuum region or at large distances away from the monolayer interface which can be considered to be bulk water. The restraining potential begins to act on the system when the value of the CV is greater (in the case of upper walls) or lower (in the case of lower walls) than a certain threshold, a_i, minus an offset, o_i. This is achieved in practice by

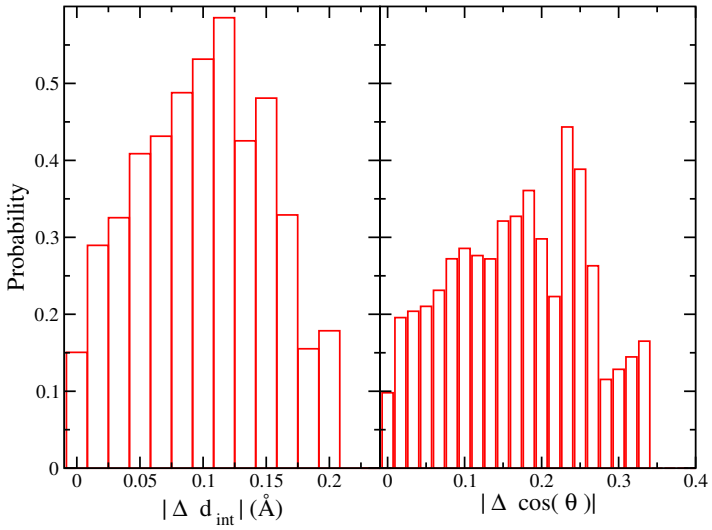

Fig. 6.2: Probability histograms of the absolute difference between the two CVs, d_{int} and $\cos\theta$, in the time period: $t \rightarrow t + \text{stride}$

applying an external potential of the form:

$$U^{\text{Wall}} = \sum_i k_i \left(\frac{(x_i - a_i + o_i)}{s_i} \right)_i^{e_i} \tag{6.2}$$

where the summation indexed by i runs over the CVs, k_i is an energy constant, and x_i is the value of the i^{th} CV. The rescaling factor, s_i, and the offset o_i were set to 0 whilst the exponent, e_i, was set to 2.

The bias factor for the well-tempered metadynamics was set to 15 to ensure a smoothly converging free energy surface. Simulation trajectories of 160 ns were obtained for the T and TP systems whilst a trajectory of 130 ns was obtained for the TE system. The simulation procedure outlined above allows the system behaviour to be studied as a function of both the location and the orientation of a drug molecule within a monolayer.

6.3 Monitoring Convergence

The ability to monitor convergence of metadynamics calculations is imperative to establish when the CV space has been adequately sampled. There are various different ways to assess convergence. One way is to calculate estimations of the FES

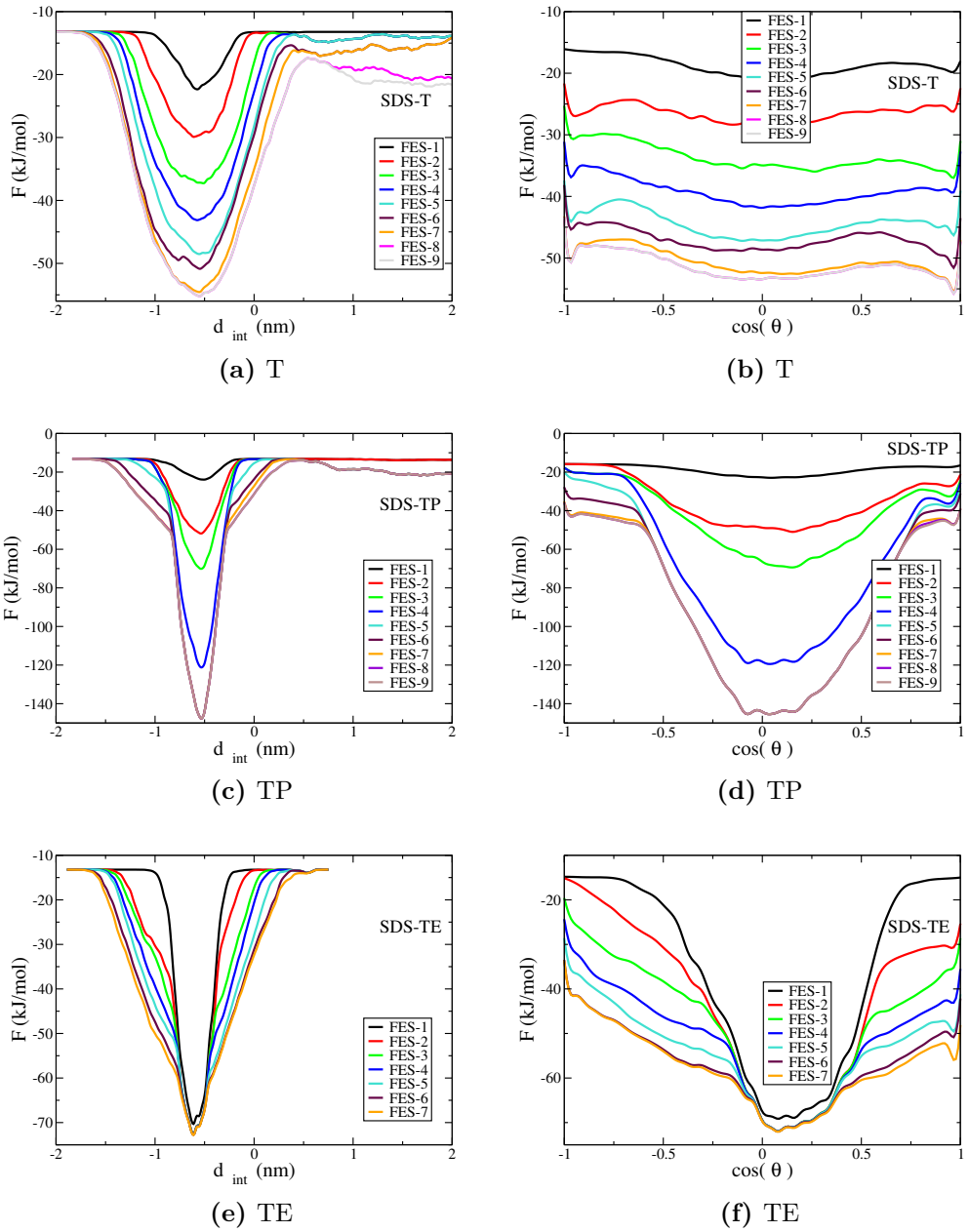

(a) T **(b)** T

(c) TP **(d)** TP

(e) TE **(f)** TE

Fig. 6.3: The left column shows the projected free energy as a function of d_{int}, as a function of time for T, TP and TE. The right column shows the projected free energy as a function of $\cos\theta$, as a function of time for T, TP and TE.

as a function of time throughout the simulation trajectory. When convergence is reached, consecutive free energy landscapes will be similar in shape, however they may differ by a constant offset in the free energy estimate. The metadynamics calculations reported in the current study involve biasing two CVs in the system and therefore the resulting FESs are also two-dimensional. This makes it challenging to visualise the differences between two free energy landscape estimates. Instead, the two-dimensional FES is projected to a one-dimensional potential of mean force (PMF), by integrating over the Boltzmann weighted free energy of each of the CVs separately:

$$F(x) = -k_B T \ln\left(\int e^{\frac{-F(x,y)}{k_B T}} dy\right) \tag{6.3}$$

where x and y represent CVs, k_B is the Boltzmann factor and T is the temperature at which the system dynamics were performed. Figure 6.3 shows free energy estimates for all three of the different metadynamics calculations, separately as a function of d_{int} and $\cos\theta$ every 20 ns. The free energy is shown as a function of d_{int} and $\cos\theta$ in the left and right columns respectively.

Figure 6.3a shows estimates of the free energy of the T system as a function of d_{int}, throughout the simulation trajectory. This plot reveals a large free energy well located at $d_{\text{int}} = -0.55$ nm, which is filled up in the period of the simulation trajectory corresponding to FES-9 and the system escapes. This is deduced from the difference in the free energy of $0.8 < d_{\text{int}} < 2.0$ in FES-8 and FES-9, indicating that the system sampled the bulk water region at the end of the simulation rather than the well. As the final two FES estimates in Figure 6.3a differ by more than a constant offset, it is concluded that this simulation has not completely converged however the free energy landscape has been well sampled. Figure 6.3b shows free energy estimates throughout the trajectory as a function of $\cos\theta$ and reveals increasing well depth for successive FESs, however the final two FES estimates are coincident indicating that the free energy calculation has converged for the $\cos\theta$ CV, if not for

d_{int}.

Conversely, it seems that the TP simulation has reached full convergence based upon the results from Figures 6.3c and 6.3d. The final two free energy estimates of the TP system as a function of d_{int} are coincident, whilst the final three free energy estimates of the TP system as a function of $\cos\theta$ are coincident. This finding, along with the observation that the T simulation has converged with respect to $\cos\theta$ but not to d_{int}, suggests that $\cos\theta$ is a faster converging CV than d_{int} and this highlights another advantage of integrating out one of the CVs and studying the resulting one dimensional PMFs: In addition to aiding comparisons between different free energy landscape estimates, this method also highlights the time taken for different CVs to converge which is a useful property to know when choosing CVs in the future.

For the TE simulation, Figures 6.3e and 6.3f show the free energy estimates over the course of the trajectory as a function of d_{int} and $\cos\theta$ respectively. These free energy estimates suggest that this system is very close to convergence, however there are differences between the last two free energy landscape estimates for both CVs. The global minimum for d_{int} is situated at -0.61 nm and the well depth remains unchanged after the FES-2 free energy estimate in Figure 6.3e. This suggests that the global minimum was filled relatively quickly and the regions in CV space around this were filled once the system escaped from the large well.

An alternative, more quantitative method of estimating convergence in metadynamics calculations is to plot the free energy difference between the global minimum of the system and a select number of other values of a CV as a function of time throughout the course of the trajectory. When convergence is reached, the difference between the free energy at the global minimum and at a given value of the CV will remain approximately constant through time. The free energy difference between the global minimum in d_{int} and the points: d_{int} =-1.0 nm, -0.8 nm, -0.2 nm, 0.2 nm, 1.0 nm, were chosen as they span the CV space well and represent states where the drug molecules are deep within the monolayer tails, near the monolayer

interface and in the bulk water. For $\cos\theta$, free energy differences between the global minimum and the points: $\cos\theta$=-1.0, -0.5, 0.0, 0.5 and 1.0 were chosen as they correspond to a wide range of orientations of the drug molecules. The difference between the free energy at the minima and at the selected values of the CVs stated above were calculated every 2 ns.

The plots in Figure 6.4 show the difference between the global minimum of the free energy and the various different CV values stated in the preceding paragraph, as a function of d_{int} and $\cos\theta$ in the left and right columns respectively. The convergence for d_{int} in the T system is shown in Figure 6.4a. All of the curves exhibit fluctuations in the free energy difference for the majority of the trajectory. The system appears to escape the free energy well at around FES-73, as fluctuations occur only at $d_{\text{int}} = 1$ nm after this showing that the free energy wells have been sampled thoroughly. These fluctuations do suggest that this CV has not reached convergence across the entire free energy surface, despite the fact that it appears to be levelling out which hints at imminent convergence. As for $\cos\theta$ (Figure 6.4b), these curves exhibit relatively small fluctuations because the free energy does not appear to change drastically across $\cos\theta$. All of the curves in Figure 6.4b remain at constant values at the end of the simulation suggesting that the orientational CV has indeed converged.

For the TP simulation, the convergence for d_{int} and $\cos\theta$ are shown in Figures 6.4c and 6.4d respectively and both reveal constant values for the difference in free energy between the test values and the global minima. This provides more concrete evidence of convergence to accompany the results from the FES estimates in Figures 6.3c and 6.3d.

For TE, the convergence for d_{int} and $\cos\theta$ are shown in Figures 6.4e and 6.4f respectively. It is clear from these figures that the calculation has not yet fully converged as there are still slight fluctuations in the curves at the end of the simulation. In particular, the curves in Figure 6.4e are on a downward trend which is ongoing

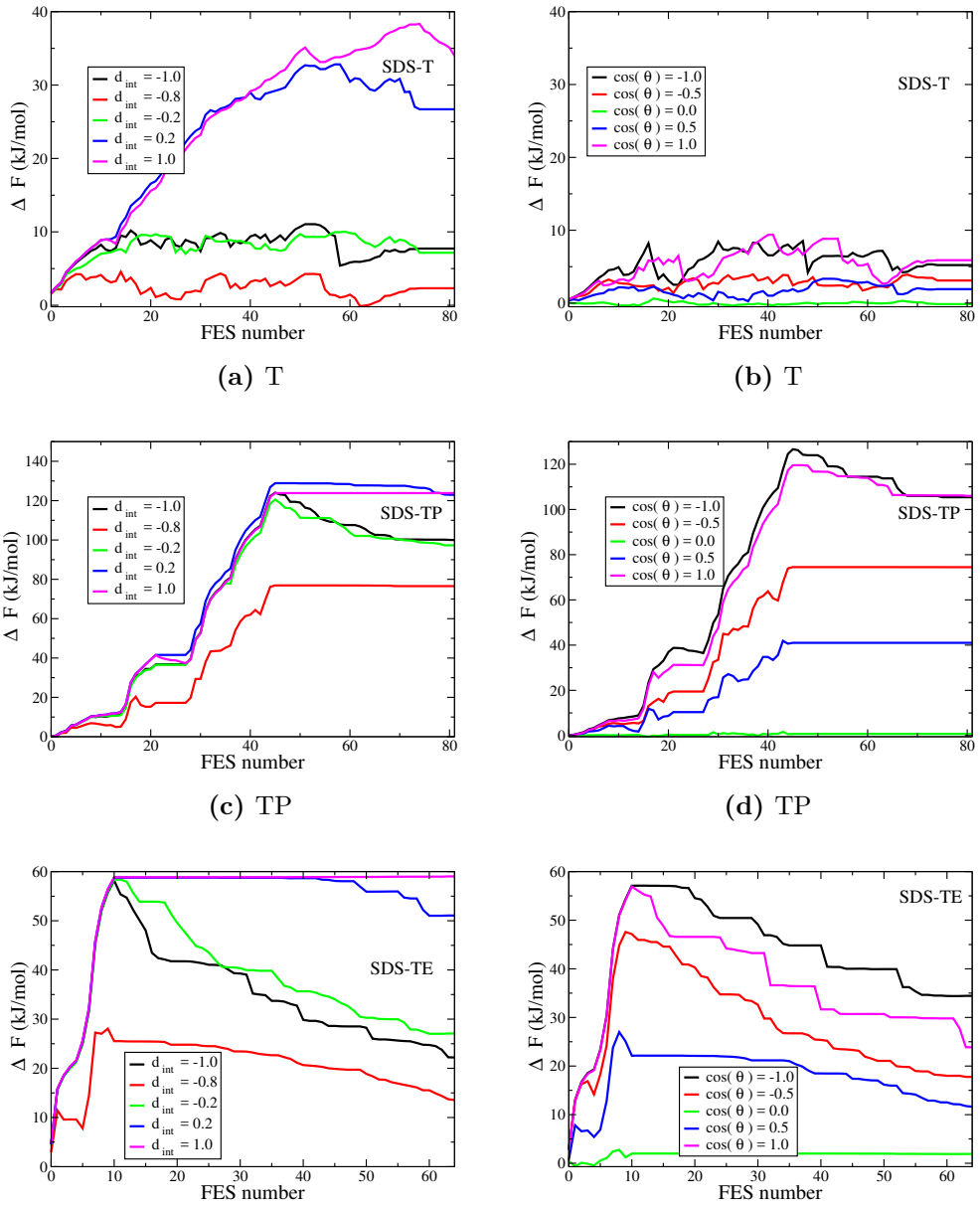

(a) T **(b)** T

(c) TP **(d)** TP

(e) TE **(f)** TE

Fig. 6.4: The figures on the left column show the difference between the free energy at a minimum and selected points along the CV as a function of d_{int}, as a function of time for T, TP and TE. The figures in the right column show the difference between the free energy at a minimum and selected points along the CV as a function of $\cos\theta$, as a function of time for T, TP and TE.

even at the end of the obtained trajectory for the TE system.

6.4 Results and Discussion

In this section, the results from the well-tempered metadynamics simulations described in Section 6.2 are presented and discussed. Figure 6.5 shows the FES estimates of the surfactant monolayer systems as a function of the collective variables d_{int} and $\cos\theta$. First, the results for the TP system are discussed given that this simulation has converged whereas the T and TE systems did not.

6.4.1 TP

The FES for the TP system is shown in Figure 6.5b. At $d_{\text{int}} = 0.5$ nm, corresponding to the TP molecule being situated in a region of the water phase in the vicinity of the monolayer interface, the free energy is at its largest value indicating that this is the least energetically favourable state of a TP molecule in the system. The free energy decreases either side of this peak, indicating that there is a small energy barrier of size ~ 10 kJ/mol which must be overcome by the TP molecule in order to insert into the SDS monolayer. Physically, this energy cost corresponds to the process of disrupting the ordered interfacial water structure which was discovered at SDS monolayer interfaces in the previous two chapters from intrinsic density plots. It should be noted that the system free energy has very little dependence on the $\cos\theta$ CV at large distances from the monolayer interface. This is because the TP molecule is surrounded by water molecules in all directions, which means that the chemical environment (and therefore the free energy) is essentially unaffected by changing the TP orientation in this region of the simulation box.

As the value of d_{int} decreases and the TP molecule approaches, and then penetrates through the monolayer interface, the free energy decreases consistently towards a single free energy minimum located at $d_{\text{int}} = -0.5$ nm, $\cos\theta = 0$. This

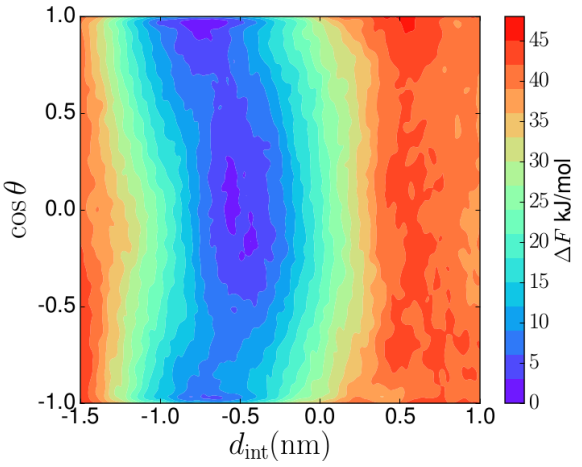

(a) T

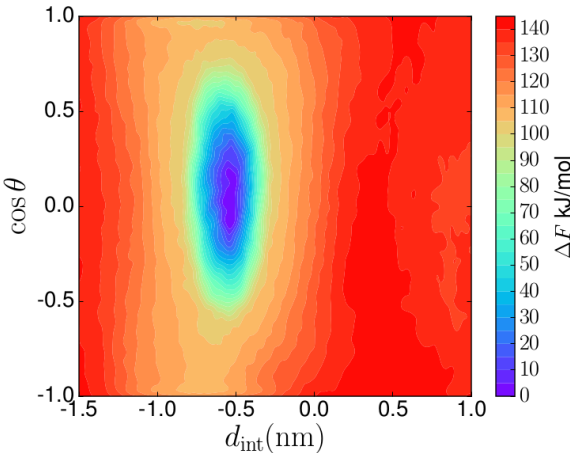

(b) TP

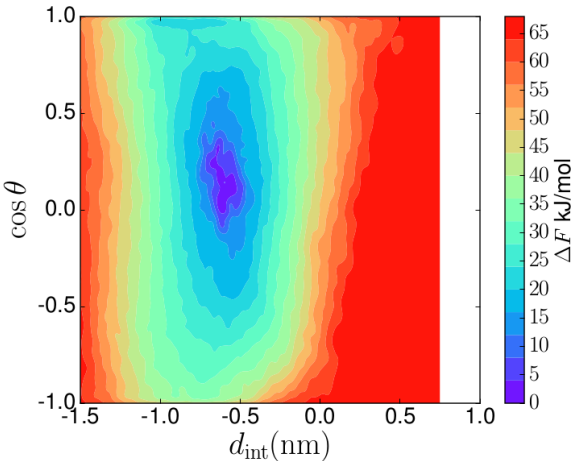

(c) TE

Fig. 6.5: Two dimensional free energy surface estimates for the a) T, b) TP and c) TE monolayer systems as a function of the collective variables d_{int} and $\cos\theta$. The colour bar on the right side of each plot shows the free energy difference between a given point and the global free energy minimum in each landscape.

means that the global free energy of a TP molecule interacting with an SDS monolayer corresponds physically to a state in which the TP molecule is located within the hydrophobic tail region, oriented such that it is perpendicular to the z-axis. The difference in free energy between the TP molecule situated at the global minimum and in the bulk water is 130 kJ/mol. The position of this free energy minimum is in direct agreement with the results obtained from the intrinsic drug orientation distributions for the SDS-TP-1 system in Chapter 5. The elliptical shape of this free energy minimum reveals that the FES has a stronger dependence upon d_{int} than $\cos\theta$ as the free energy well is more broad across $\cos\theta$ than d_{int}. The orientational preference is still very prominent however as comparing the free energy at the points (d_{int}=-0.5 nm, $\cos\theta$=0) and (d_{int}=-0.5 nm, $\cos\theta$=1.0) shows $\Delta F = 100$ kJ/mol. A possible explanation for this $\cos\theta$ free energy dependence is as follows. When TP is oriented parallel to the z-axis, a hydrogen bond between water molecules and either the O1 or the O2 atom in TP will likely be broken, at the same time a larger portion of the nonpolar TP aromatic carbon rings will be exposed to the water molecules located within the monolayer near the surfactant headgroups.

The free energy increases as d_{int} becomes more negative, until $d_{\text{int}} = -1.4$ nm at which point the free energy is comparable with that in the bulk water region. The position $d_{\text{int}} = -1.4$ nm corresponds to TP being located in the vacuum region, based upon the monolayer thickness measurements conducted in the previous two chapters. The free energy of the system increases when TP is situated in the vacuum region because of the decreased number of energetically favourable van der Waals interactions between the TP molecule and the surfactant tails.

6.4.2 T

The free energy surface for T is shown in Figure 6.5a. At large values of d_{int}, the free energy appears to resemble the corresponding behaviour that was observed for

TP in that there is a small free energy barrier to insertion of the drug molecule when approaching the monolayer interface from the bulk water region. In the case of T, the barrier is discontinuous across $\cos\theta$ which suggests that the simulation is slightly undersampled and that a longer simulation is required for convergence of the landscape, as discussed previously. However even at this stage, the simulatiom is informative about the existence of this interfacial barrier. As the value of d_{int} decreases from $d_{\text{int}} = 0.5$ nm to $d_{\text{int}} = 0$ nm, so too does the free energy as this corresponds to the T molecule being located in the vicinity of the monolayer interface. The free energy continues to decrease as d_{int} decreases further, up to a free energy minimum situated at approximately the same location as the global minimum in the TP system: $d_{\text{int}} = -0.5$ nm, $\cos\theta = 0$. This free energy minimum corresponds to a state in which the T molecule is located within the hydrophobic tail region and oriented such that it is perpendicular to the z-axis, much in the same way as the global minimum for TP.

Despite these very similar minimum free energy states in the FESs of TP and T, there are several distinct differences between the FES estimates. First, T appears to exhibit three minima whereas TP has merely one, global minimum. These additional minima for T have the same free energy value as the minimum located at $d_{\text{int}} - 0.5$ nm, $\cos\theta 0$ (~ 0 kJ/mol) and correspond to states where the drug molecule is oriented approximately parallel to the z-axis. The additional minima are located at (d_{int}=-0.7 nm, $\cos\theta = 1$) and (d_{int}=-0.7 nm, $\cos\theta = -1$) showing that the T molecule inserts deeper into the monolayer when adopting parallel orientations with respect to the z-axis. This is presumably to ensure that the molecule is contained within the monolayer tail region, which will require the centre of mass of T to be situated at a more negative value of d_{int} than for the perpendicular orientation. Another difference between the FESs is that there is a much weaker free energy dependence on $\cos\theta$ for T than for TP. This is clearly evident by visual inspection of Figures 6.5b and 6.5a, the FES for T has a blue strip spanning the monolayer tail region indicating

that all of these states are low in free energy as compared to the bulk water, over the entire range of $\cos\theta$. As postulated in Chapter 5, this is most likely due to the motivation of TP to adopt a parallel orientation with respect to the z-axis so that all oxygen atoms within TP are in contact with water, forming energetically favourable hydrogen bonds. The T molecule has one less oxygen atom than the TP and TE molecules and therefore forms fewer hydrogen bonds with water molecules at the monolayer headgroup region. This means that T is readily able to adopt a variety of different orientations, not merely one in which it is perpendicular to the z-axis, as is the case for TP and TE. The orientational behaviour of T and TP, as inferred from two corresponding FESs shown in Figures 6.5a and 6.5c, is consistent with the intrinsic drug orientation distributions for the SDS-TP-1 and SDS-T-1 simulations presented in Chapter 5. One additional way in which the FES plots for TP and T differ significantly is that the free energy minima in the T landscape are 40 kJ/mol deep, which is much shallower than the 130 kJ/mol free energy minimum in the TP landscape. This difference in the free energy well depths for T and TP indicates that a TP molecule is significantly more energetically stable within the monolayer tail region, compared to a T molecule. This is in agreement with the findings of Saaka [32], namely that SDS aggregates encapsulate a greater amount of TP than T.

6.4.3 TE

Figure 6.5c shows the free energy surface for a TE molecule interacting with an SDS monolayer. At large values of d_{int}, the free energy is at its maximum and once again there is no $\cos\theta$ dependence on the free energy of a TE molecule in the bulk water region. As d_{int} becomes less positive, there is no energy barrier to the insertion of TE into the monolayer observed. This is most likely due to lack of sampling in larger values of the d_{int} CV, as shown in Figure 6.3e. Given that TE is the largest of

the testosterone-based compounds it seems unlikely that there would be no energy barrier to disrupting the interfacial water layer upon transit from the bulk water region to the monolayer interface. At the monolayer interfacial region, $d_{\text{int}} \sim 0$, the free energy decreases as the TE molecule moves into the monolayer tail region much in the same way as for TP and T. The specific value of d_{int} where the free energy begins to decrease at the interface, from the value in the bulk water, is a function of $\cos\theta$. The most likely reason why this feature is observed for TE and not for TP is as a result of the extended ester chain in TE. When $\cos\theta$ = -1, the O2 atom in TE is closest to the water phase and the majority of the molecule is located within the monolayer tail region. Conversely, when $\cos\theta = 1$ the O1 atom in TE is closest to the water phase whilst the ester chain is in the vacuum region, effectively dragging the centre of mass location of the TE molecule away from the monolayer interface to more positive values of d_{int}. This is a subtle feature of the TE FES which surely would have been missed using a distance metric without a thorough treatment of the monolayer intrinsic surface (such as those employed in [128–130]).

As d_{int} decreases further and becomes negative, corresponding to the TE molecule being situated in the monolayer tail region, the FES is reminiscent to that of TP in that there is a single global minimum located at almost the same location in CV space but at a slightly larger value of $\cos\theta$: $d_{\text{int}} \sim -0.5$ nm, $\cos\theta \sim 0.1$, again corresponding to a state in which the TE molecule is located within the hydrophobic tail region, oriented such that it is perpendicular to the z-axis. The similarities in form of the FES estimates for the TE and TP systems are unsurprising considering the similarities between these two compounds in both their chemistry, and their intrinsic drug orientation profiles presented in Chapter 5. The depth of the free energy well in Figure 6.5c is $\sim$ 65 kJ/mol which is significantly shallower than that of TP. This observed discrepancy in the free energy well depth of TE and TP could possibly be due to the increased size of TE, which may experience larger steric barriers within the monolayer tail region.

6.5 Conclusions

In this chapter, results from well-tempered metadynamics simulations of testosterone-based compounds interacting with SDS monolayers have been presented in which the depth of penetration of drug molecules, along with their orientation with respect to the z-axis were biased and used as collective variables. The free energy surface of the TP system was determined to have reached full convergence based upon the criteria outlined in Section 6.3. Even though the calculations for T and TE did not reach full convergence within the simulations conducted, the analysis in Section 6.3 suggests that they are close to converging. Moreover, the free energy wells in both the T and TE simulations were successfully flooded and the drug molecules explored the majority of the other relevant regions in their respective CV space. Given that the relevant free energy minima were flooded, reliable estimates of the depth of the free energy wells were obtained. This permitted quantitative comparisons of the relative stability of the different testosterone-based compounds within the monolayer hydrocarbon tail regions by comparing the depth of their respective free energy minima. It was revealed that TP is by far the most stable drug molecule within the SDS monolayer, able to lower its free energy by $\sim$ 130 kJ/mol by transitioning from the bulk water phase into the monolayer hydrocarbon tail region. T and TE are only able to lower their free energy by $\sim$ 40 kJ/mol and $\sim$ 65 kJ/mol, respectively for the same transition. This is a result which is qualitatively consistent with the experimental observation that TP is more effectively encapsulated within SDS aggregates than T or TE. Additionally, the depth of the free energy wells for the simulations performed in this chapter are comparable to those found in a study by Jämbeck *et al* [130] in which the free energy of permeation of both ibuprofen and aspirin molecules within a lipid bilayer system were estimated and found to be 70 kJ/mol and 60 kJ/mol respectively. These molecules are comparable in size to the testosterone-based compounds studied in this chapter and the similarity in the

free energy well depths between the compounds in the current study and that of Jämbeck *et al* is encouraging.

In this chapter, the insight obtained into the orientational behaviour of the testosterone-based compounds are consistent with the MD simulations performed on the same systems in Chapter 5. Additionally, the depth of insertion of the testosterone-based compounds was rigorously quantified by incorporating the intrinsic surface into the definition of the distance CV, d_{int} which uncovered subtle interfacial features in the free energy surface of the TE system. The simulation protocol utilised in this chapter can easily be applied to study the permeation of solutes within arbitrary surfactant monolayer and lipid bilayer systems and should therefore be useful to the wider biomolecular simulation community.

In the last three chapters, surfactant monolayers have been investigated thoroughly using both molecular dynamics and well-tempered metadynamics simulations, with and without the presence of testosterone-based compounds. The following two chapters focus on SDS micelles which are modelled using molecular dynamics simulations with and without TP molecules with the aim of studying the solubilisation process of the surfactant-drug pairing which has been identified as being the most effective encapsulation system.

Chapter 7

Simulating and Analysing Surfactant Micelles

In Chapter 8, results are reported from all-atom MD simulations of two distinct surfactant micelle systems. In this chapter the design and protocol of these simulations is explained and the analysis techniques conducted on them is described in detail.

7.1 Simulation Protocol

All-atom MD simulations have been used to investigate how the presence of TP affects the structural and interfacial properties of a SDS micelle in an aqueous solution. In order to do so, two systems were simulated, one with only SDS and water and the other with SDS, TP and water (these systems will be referred to as SDS and SDS+TP, respectively, throughout the remainder of this thesis). In each case the results of neutron scattering experiments were used to determine the number of molecules within the micelles which have been simulated. The SDS simulation was used to study an SDS micelle containing 80 surfactant molecules alone in an aqueous solution. The surfactant molecules were pre-assembled into a spherical aggregate using the Packmol software package [51], which was then minimised using a

conjugate gradient minimisation algorithm. Then the system was thermalised using an NVT simulation in which the temperature was held constant at 300 K for 240 ps. After the thermalisation stage, the aggregate was placed into the centre of a 126 Å × 126 Å × 126 Å simulation box with 64,083 water molecules, which results in the concentration of the SDS in the solution being the same as that used in the neutron experiments (3 g/100mL). The simulation approach applied here is similar to a previous study of surfactant micelles in the presence of oil molecules [132]. Then the structure of the hydrated SDS micelle was minimised in order to remove any clashes between water molecules and SDS molecules. The system was subsequently thermalised by employing an NVT simulation for 20 ps. Finally, the pressure within the system was equilibrated to 1 atm using the NPT ensemble for 20 ns.

The second system was built so a TP containing SDS micelle could be studied. First, a micelle containing 76 SDS monomers was pre-assembled using the Packmol software package [51] in a similar fashion as the first system. The micelle was then minimised and thermalised *in vacuo* in an identical manner as was used for the SDS micelle system. Next the thermalised micelle was placed within a box of water large enough to make the resulting concentration of SDS to be 3 g/100mL (same as in neutron experiments). Another energy minimisation was performed on the solvated micelle system, after which the system was thermalised at 300 K using a NVT simulation which was 400 ps in duration. After allowing the micelle to form the initial intermolecular interactions that stabilise it in solution, the TP molecules were introduced into the system. In order to minimise disruption to the interfacial water layer, the SDS aggregate and all water molecules within 5 Å of the aggregate interface were kept from the final configuration of the thermalisation simulation. Then, 13 TP molecules were placed just outside the interfacial water layer, ensuring that they were within the interaction cut-off radius of 10 Å from the micelle surface. Water molecules were re-inserted into the simulation box to ensure that the total number of water molecules in the system was equal to that of the system before

the addition of TP. The resulting system was subjected to an energy minimisation simulation, followed by three further equilibration stages. First, a simulation was carried out in order to equilibrate the pressure of the new system to 1 atm using the NPT ensemble for 2 ns. Next, the temperature was equilibrated at 300 K by running a NVT simulation for 100 ps. Finally, a NPT simulation was performed for 20 ns.

The resulting SDS micellar and SDS+TP micellar systems were used to carry out the production simulations, which were performed using the NPT ensemble at a temperature of 300 K, atmospheric pressure and run for 80 ns. All simulations were performed using the LAMMPS simulation package [70] with the CHARMM force field [71, 72] for the description of both inter- and intra-molecular interactions of the SDS and TP. The TIP3P water model [65], which was modified for the CHARMM forcefield [66], was used to describe interactions involving water. The van der Waals interactions were cut-off at 10 Å whilst the electrostatic interactions were cut-off at 12 Å. The PPPM method [133] was used to compute long-range Coulombic interactions. The LAMMPS implementation [134–137] of the Nosé-Hoover thermostat [59] was used to fix the system temperature in all simulations, while the system pressure was controlled using a Nosé-Hoover barostat [60] in the NPT simulations. A timestep of 2 fs was used in all production simulations to ensure stable integration of Newton's equations of motion with the velocity Verlet algorithm whilst all hydrogen-containing bonds were constrained using the SHAKE algorithm [138]. The measurements discussed in Chapter 8 were conducted using the entirety of the 80 ns production periods for both simulations in which the systems were deemed to be stable throughout, based upon stability of the eccentricity and solvent accessible surface area measurements.

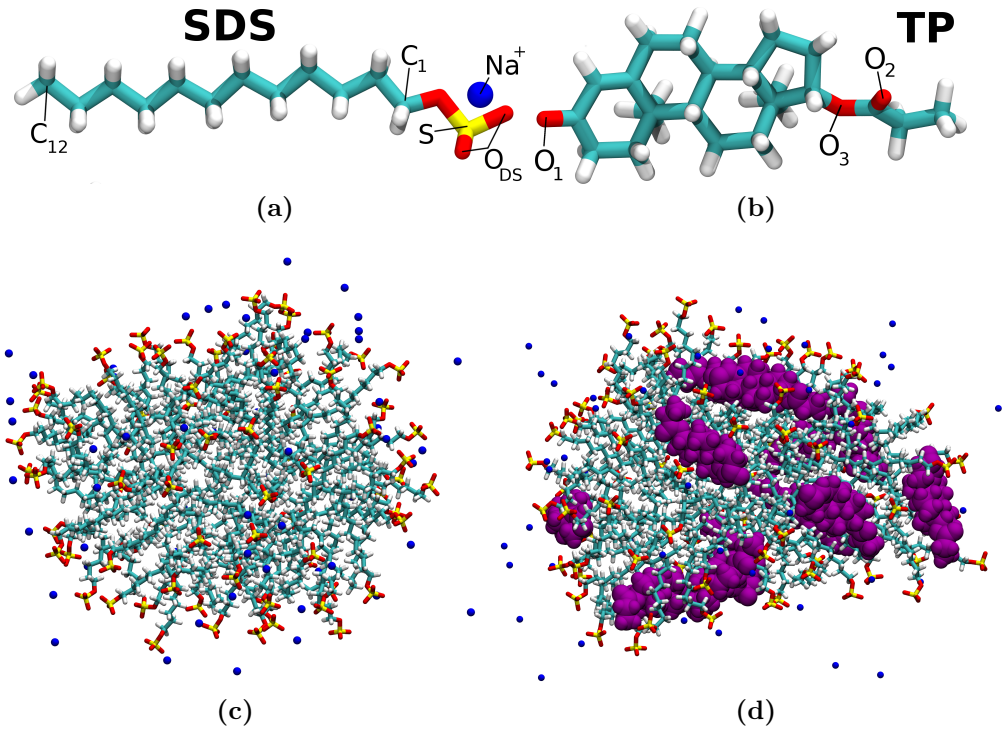

Fig. 7.1: The chemical structures for SDS and TP molecules are shown in a) and b) respectively with labels for key atoms shown which are referenced in the analysis. The images in c) and d) show representative snapshots of typical configurations of the SDS and SDS+TP micelles respectively from the production simulations.

7.2 Analysis Techniques

7.2.1 Micelle Shape and Structure

The ability to describe the shape and structure of micelles is imperative to understanding their behaviour. This can often prove to be challenging due to the chaotic and dynamic nature of these aggregates. In Chapter 8, a variety of different physical quantities and distributions are presented to describe the structure of the micelles that are observed in the simulations described in Section 7.1.

7.2.1.1 Micelle Surface Area

First, it must be established whether the micelle system has equilibrated before steady-state properties can be calculated. The solvent accessible surface area (SASA)

[139, 140] is a common method employed to calculate the surface area of complex molecular geometries and can be instructive in monitoring system equilibration. The SASA is calculated by rolling a spherical probe, which is given a radius 1.4 Å to approximate a water molecule, over the van der Waals surface of the micelle and estimating the surface area as shown in Figure 7.2a. The Voronoi tessellation method, implemented in the Voro++ software library that is integrated into LAMMPS [141], has also been employed to estimate the micelle surface area for means of comparison to the SASA. This method constructs cells around the atoms, where the segments of the Voronoi cell are all the points in the plane that are equidistant to the two nearest sites (Figure 7.2b). The Voronoi vertices are the points equidistant to three (or more) sites and the surface area of the micelle can be estimated by summing up the area of the Voronoi cell faces which are on the boundary between an atom in the micelle and an atom in the solvent.

7.2.1.2 Eccentricity

In addition to the surface area, the micelle eccentricity, η, provides an alternate description of the micelle geometry and is also useful for monitoring equilibration. This is defined as:

$$\eta = 1 - \frac{I_{min}}{I_{avg}} \tag{7.1}$$

where I_{min} and I_{avg} denote the minimum and average moments of inertia of the micelle, respectively. When $\eta = 0$, the micelle is perfectly spherical and as $\eta \to 1$ the micelle tends towards being infinitely oblong in shape. The eccentricity can also be used as a metric for micelle equilibration, when the micelle shape stabilises the eccentricity will converge and exhibit small fluctuations around a constant value.

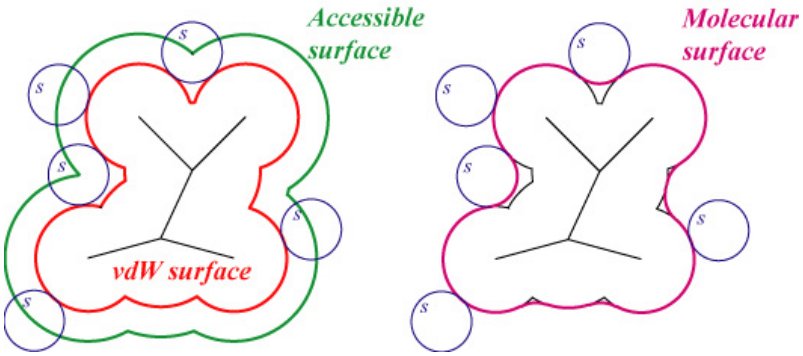

(a)

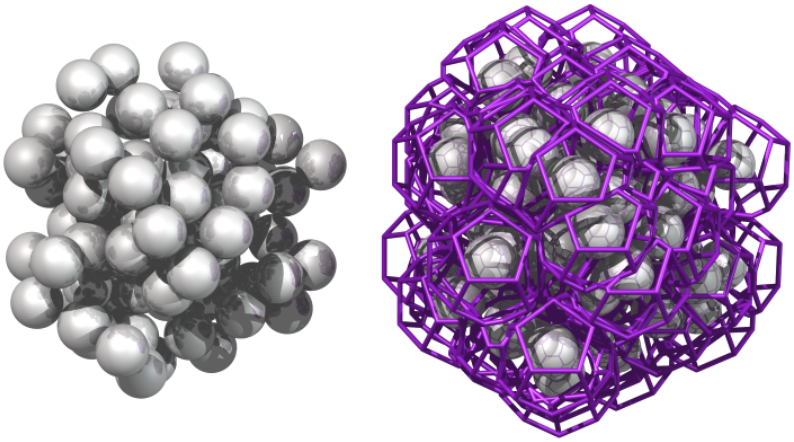

(b)

Fig. 7.2: a) A schematic diagram of how the solvent accessible surface area is calculated from the van der Waals surface (image taken from http://csb.stanford.edu/~koehl/ProShape/protsurf.php) b) An example of the voronoi cells for an arbitrary molecular system (image taken from http://math.lbl.gov/voro++/examples/irregular/irregular_l.png)

7.2.1.3 Radial Density

A more detailed description of the internal micelle structure is obtained by measuring the density of various atomic species at a given displacement from the micelle centre of mass, d_{cm}. These distributions characterise the extent to which the density of atomic species fluctuates along the micelle radial axis and they also provide some insight into the penetration depth of water, counterions and drug molecules into the micelle core. The radial density is determined by calculating the distance of selected atoms from the micelle centre of mass in every snapshot and counting the number of atoms in 1 Å thick concentric shells around the micelle centre of mass.

The effect of water penetrating into the micelle core is of particular relevance when studying encapsulation of hydrophobic solutes in micelles. In order to establish how much contact there is between the hydrocarbon tails and water molecules, a shell region within the micelle is defined in accordance to the method used by Bruce *et al.*[142]. From the radial density profiles, the difference between the value of d_{cm} where the density of water reaches 10% of its bulk value, and the value of d_{cm} where the density of carbon atoms in the surfactant molecules decays to 10% of its peak value is determined. The value of this difference gives an indication of how much overlap exists between the water molecules and the hydrophobic surfactant tails. By comparing the size of this shell region from the two micelle simulations, the effect that the presence of TP molecules has on water penetration into the micelle core can be realised.

7.2.1.4 Micelle Intrinsic Surface

The importance of providing a detailed description of surfactant aggregate interfaces is discussed in Section 3.3.1 of Chapter 3. The complex interfacial structure of micelles in MD simulations is typically neglected, instead the micelle is approximated to be a well defined geometric shape (e.g. sphere, cylinder) in analyses such as the radial density. This is a coarse aproximation which will have a negative effect on measurements related to the interfacial properties of these systems that play a key role in so many of their applications. The determination of the intrinsic surface will provide a more complete picture of the interfacial structure of micelles, as they do for surfactant monolayers.

In order to determine the intrinsic surface of the micelles studied within this thesis, a new method has been developed which provides a continuous representation of the surface and is calculated as follows. In an analogous way to many intrinsic surface constructions for surfactant monolayers [78, 79, 81, 143], the choice of anchor points is a trivial one: the sulphur atoms in the DS^- headgroups. When calculating

the distance from an atom, j, to the micelle interface, let the vector pointing from $\mathbf{c}_\mathrm{m}$ to the position of j be denoted as $\mathbf{r}_j$. Similarly, let the vector pointing from $\mathbf{c}_\mathrm{m}$ to sulphur atom i, be denoted by $\mathbf{s}_i$. A continuous description of the micelle intrinsic surface is desired and so this must be well defined at any given $\vec{r_j}$. Moreover, the surface function should be smooth and continuous, absent of abrupt jumps in micelle depth like those present in [144]. To produce an intrinsic surface definition inclusive of the desired attributes stated above, the surface is calculated as a continuous function of all of the anchor points in the micelle. The magnitudes of the vectors $\{\mathbf{s}_i\}$ provide an indication of the micelle depth at each anchor point. A weighted average is employed to determine the micelle depth at any given point, $\mathbf{r}_j$, such that the influence of anchor points is a decaying function of the angle between vectors $\mathbf{r}_j$ and $\mathbf{s}_i$, denoted by θ_{ij} (see Fig. 7.4). The distance to the intrinsic micelle surface d_int from any point $\mathbf{r}_j$, is defined mathematically as follows:

$$d_\mathrm{int}(\mathbf{r}_j) = |\mathbf{r}_j| - \frac{\sum_{i=1}^{N} \exp\left[-\lambda\theta_{ij}^2\right] \cdot |\mathbf{s}_i|}{\sum_{i=1}^{N} \exp\left[-\lambda\theta_{ij}^2\right]} \tag{7.2}$$

where N is equal to the number of anchor points present in the micelle, θ_{ij} denotes the angle in radians between the vectors $\mathbf{s}_i$ and $\mathbf{r}_j$ and λ is a free parameter which determines how smooth the resulting intrinsic surface is. As $\lambda \to 0$, the intrinsic surface tends towards a perfect sphere, the radius of which is equal to the average micelle radius, i.e. the average over the magnitudes of $\{\mathbf{s}_i\}$. As $\lambda \to \infty$, the surface tends towards that of a Voronoi polygon where the micelle depth at $\mathbf{r}_j$ is equal to the depth of the anchor point which subtends the smallest angle θ_{ij}. This produces a discontinuous surface, reminiscent of that presented in [144]. Images of the intrinsic surface for small λ ($\lambda = 0$) and large λ ($\lambda = 1000$) are shown in Fig. 7.3. Clearly, the value of λ should be chosen to produce a surface for which the micelle depth is close to the value of $|\mathbf{s}_i|$ in the vicinity of anchor point i, yet

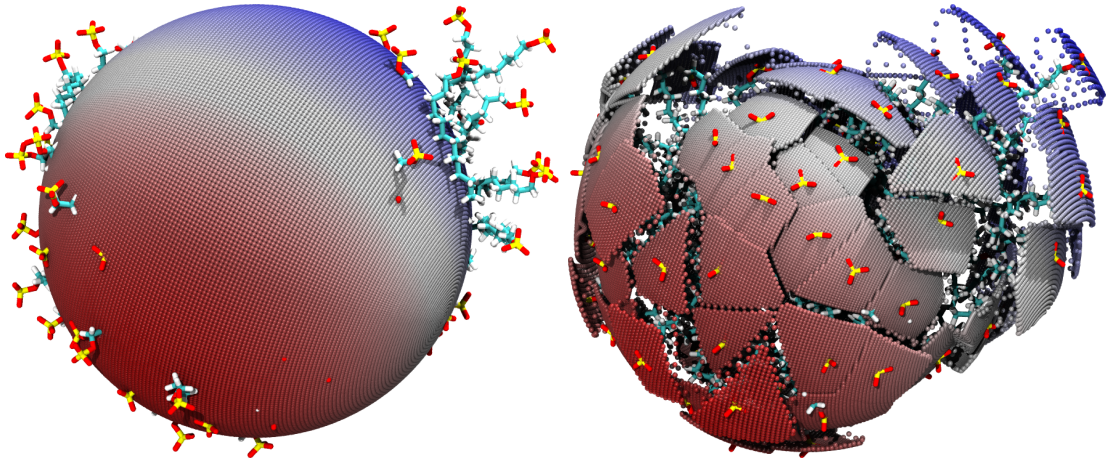

(a) $\lambda = 0$ **(b)** $\lambda = 1000$

Fig. 7.3: Images of the intrinsic surface constructed for the SDS micelle with λ values set to a) 0 and b) 1000. The micelle has the same orientation in both images, which shows the contrast in the resulting surfaces. These images highlight the dependence of the resulting surface on the choice of λ. Note that TP molecules have been omitted from these images for clarity.

changes smoothly and continuously in regions between anchors. The value of λ can be systematically chosen by establishing the typical angle between the vectors $\{\mathbf{s}_i\}$ of nearest neighbour anchor points throughout the trajectory, $\bar{\theta}$, and then use this angle to determine λ for a specific system: $\lambda = 1/\bar{\theta}^2$. In this way, the decay constant of the function is in the order of the typical separation of nearest neighbour anchors. This method yielded the choice of $\lambda = 15$ for the system in the SDS+TP micelle and was used for all analysis performed.

Another complicating phenomena when trying to identify the surface of soft interfaces is the protrusion of individual molecules further into the water phase. By choosing λ as discussed above, it is ensured that a protruding surfactant molecule does not especially influence the local definition of the micellar surface. This value of λ ensures that the micelle depth in the vicinity of a dislodged surfactant will be heavily influenced by the other anchor points, which will effectively drag the surface back towards the rest of the micelle, as illustrated on the right hand side of Fig. 8.7b, as opposed to creating discontinuities in the surface like those in Fig. 7.3b.

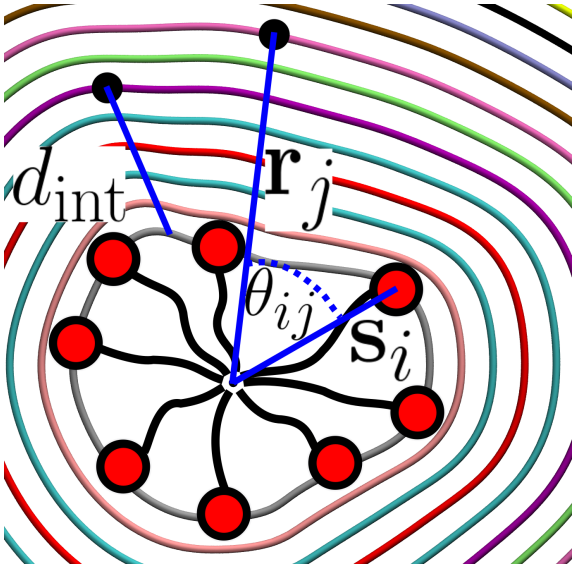

Fig. 7.4: A schematic diagram showing various quantities discussed in the text: Coloured rings represent isovalues of d_{int} for a particular micelle configuration, the distance d_{int} is shown along with the vectors $\mathbf{s}_i$, $\mathbf{r}_j$ and the angle θ_{ij}.

7.2.1.5 Intrinsic Density

To determine the intrinsic density, the procedure is very similar to that for the radial density (which is outlined above in Section 7.2.1.3), except that the density is expressed in terms of d_{int} rather than d_{cm}. One ramification of this variable change is the increased complexity of determining the volume of the spatial intervals used in the intrinsic density calculation. When measuring the radial density, the volume of a spatial interval centred at r is calculated by evaluating the integral over the spherical surface:

$$V(r) = \int_{r-dR/2}^{r+dR/2} \int_0^{2\pi} \int_0^{\pi} r'^2 \sin\theta d\theta d\phi dr' \tag{7.3}$$

where r', θ and ϕ are spherical polar coordinates and dR is the width of the spatial interval. From this, an analytic expression for the volume of a spatial interval centred at r is obtained: $V(r) = \frac{4}{3}\pi[(r + \frac{dr}{2})^3 - (r - \frac{dr}{2})^3]$, where r denotes the distance between $\mathbf{c}_{\text{m}}$ and the centre of the spatial interval. For the intrinsic density, the volume of the spatial intervals can in principal be calculated by evaluating a similar

triple integral over the intrinsic surface as the one presented in Eq. 7.3. However, in this instance, r' is a function of θ and ϕ (i.e $r' = r'(\theta, \phi)$), therefore this integral cannot be solved analytically and to solve it numerically for each spatial interval at every snapshot would be a laborious task. Instead, the volume is estimated as follows. First, the simulation box is divided up into a 3-D grid with a specified grid width, d_{g} (which should be no larger than the width of the spatial interval). The volume of a spatial interval is then estimated by summing up the volume of each grid element, d_{g}^3, which resides within the spatial interval. The average intrinsic density is obtained by dividing the number of atoms located within a spatial interval by the instantaneous volume of the spatial interval, and averaging over many snapshots taken from a stable part of the simulation trajectory.

7.2.1.6 Water Orientation

The encapsulation process of TP molecules within an SDS micelle is affected not only by the properties of the micelle itself, but also by the structure of the water molecules surrounding the micelle. An instructive way to study this is through orientation profiles of water molecules. The dipole vector of a water molecule is defined, $\hat{\mathbf{p}}$, as a unit vector pointing from the Ow atom to the geometric centre of the two Hw atoms in a water molecule. Then the orientation of this vector is compared with $\hat{\mathbf{r}_j}$, that is a unit vector pointing from $\mathbf{c}_{\mathrm{m}}$ to Ow. The dot product of these vectors describes the orientation of a water molecule: $\cos(\theta)$. When $\cos(\theta) = 1.0$, the water molecule is oriented such that its dipole vector is in perfect alignment with $\mathbf{r}_j$, when $\cos(\theta) = -1.0$, the water molecule is oriented such that its dipole vector forms a 180° angle with $\mathbf{r}_j$. Probability density distributions can be constructed which describe the likelihood of observing a water molecule with a particular orientation

at a given value of the distance:

$$\rho_d(\cos(\theta)) = \left\langle \frac{1}{N_d} \sum_{j=1}^{N_{\text{wat}}} \delta(d - d_j)\delta(\cos(\theta) - \cos(\theta_j)) \right\rangle \tag{7.4}$$

where $\rho_d(\cos(\theta))$ is the probability density of finding a water molecule with an orientation, $\cos(\theta) = \hat{p} \cdot \hat{r_j}$, for a given value of distance d. N_d is the instantaneous number of water molecules located at d, the summation indexed by j runs over all N_{wat} water molecules in the system, and δ denotes the Dirac delta function.

The radial water orientation profile is obtained by calculating the function defined in Eq. 7.4 using d_{cm} as the distance and thus describes the orientation of water molecules as a function of their distance away from $\mathbf{c}_{\text{m}}$. Alternatively, the intrinsic water orientation profile is produced by calculating the function defined in Eq. 7.4 using d_{int} as the distance, which describes the orientation of water molecules as a function of their distance away from the micelle intrinsic surface.

7.2.1.7 Gaussian Curvature

In order to characterise the curvature of the micelle surface, the coordinates of the molecules in the micelle first need to be translated such that the $\mathbf{c}_{\text{m}}$ is positioned at the origin. Then the micelle's intrinsic surface can be expressed by a vector in Cartesian coordinates, $\mathbf{r}$, as a function of the azimuthal and zenith angles, θ and ϕ respectively:

$$\mathbf{r}(\theta,\phi) = \frac{\sum_{i=1}^{N} \exp\left(-\lambda \arccos\left[\hat{\mathbf{s}}_i \cdot (\sin\theta\cos\phi, \sin\theta\sin\phi, \cos\theta)\right]^2\right) \cdot |\mathbf{s}_i|}{\sum_{i=1}^{N} \exp\left(-\lambda \arccos\left[\hat{\mathbf{s}}_i \cdot (\sin\theta\cos\phi, \sin\theta\sin\phi, \cos\theta)\right]^2\right)} \begin{bmatrix} \sin\theta\cos\phi \\ \sin\theta\sin\phi \\ \cos\theta \end{bmatrix} \tag{7.5}$$

where the summation indexed by i, runs over the N anchor points present in the micelle and $\mathbf{s}_i$ is the vector pointing from $\mathbf{c}_m$ to the i^{th} anchor point. From this

formulation, the local Gaussian curvature can be calculated as the ratio of the first and second fundamental forms of the intrinsic surface function, $r(\theta, \phi)$:

$$\kappa = \frac{\det(\mathbf{II})}{\det(\mathbf{I})} = \frac{\mathrm{LN} - \mathrm{M}^2}{\mathrm{EG} - \mathrm{F}^2} \tag{7.6}$$

where κ is the Gaussian curvature, $\mathbf{I}$ denotes the first fundamental form with coefficients E, F and G, $\mathbf{II}$ denotes the second fundamental form with coefficients L, M and N [145]. The first fundamental form is often written in the modern notation of the metric tensor. The coefficients may then be written as:

$$\mathbf{I} = (\mathrm{g_{ij}}) = \begin{bmatrix} g_{11} & g_{12} \\ g_{21} & g_{22} \end{bmatrix} = \begin{bmatrix} E & F \\ F & G \end{bmatrix} \tag{7.7}$$

where the components of this tensor are calculated as the scalar product of tangent vectors $\mathbf{r}(\theta, \phi)_\theta$ and $\mathbf{r}(\theta, \phi)_\phi$ (the first partial derivatives of $\mathbf{r}$ with respect to θ and ϕ):

$$g_{ij} = \mathbf{r}(\theta, \phi)_i \cdot \mathbf{r}(\theta, \phi)_j \tag{7.8}$$

To calculate the second fundamental form, denoted as $\mathbf{II}$, first the normal vector field to the surface is defined as follows:

$$\mathbf{n} = \frac{\mathbf{r}(\theta, \phi)_\theta \times \mathbf{r}(\theta, \phi)_\phi}{|\mathbf{r}(\theta, \phi)_\theta \times \mathbf{r}(\theta, \phi)_\phi|} \tag{7.9}$$

Once the normal vector field is determined, the second fundamental form is calculated:

$$\mathbf{II} = \begin{bmatrix} L & M \\ M & N \end{bmatrix} \tag{7.10}$$

where these coefficients are realised through the dot product of the normal vector $\mathbf{n}$ and second partial derivatives of $\mathbf{r}$: $L = \mathbf{n} \cdot \mathbf{r}(\theta, \phi)_{\theta\theta}$, $M = \mathbf{n} \cdot \mathbf{r}(\theta, \phi)_{\theta\phi}$ and $N = \mathbf{n} \cdot \mathbf{r}(\theta, \phi)_{\phi\phi}$. Finally, the Gaussian curvature is calculated by substituting in the

expressions for the coefficients E, F, G, L, M and N for **I** and **II** into Eqn. 7.6 [145]. This provides a description of the local curvature of the micelle intrinsic surface, a useful property which has yet to be incorporated into the analysis of micelles in the literature. Positive values of curvature correspond to either convex or concave regions of the surface, whereas negative curvature values correspond to saddle points. As an illustration of how the curvature can be incorporated into analysis of micellar systems, the lifetimes of highly curved micelle regions are investigated in the hope of improving understanding of the typical time scales over which the micelle geometry fluctuates. This is achieved by choosing a curvature magnitude threshold and then producing histograms of the time taken for the curvature of a point on the micelle surface to change in the two following ways: i) to decrease from the positive threshold value to 0, corresponding to a convex/concave region flattening out and ii) to increase from the negative threshold value to 0, corresponding to a saddle point flattening out.

7.2.1.8 Angle Distributions

Torsional effects arising from thermal fluctuations in the solvent can influence micellar structure by causing the surfactant tails to bend relative to some average position with respect to the micelle radial axis. The SDS chain angle distribution is a relatively simple method of determining how significant this torsional motion is to the micelle structure. The SDS chain angle is defined as the angle between the vectors formed between C1 (the headgroup carbon) and the micelle centre of mass ($\mathbf{c}_m$), and the vector connecting C12 (the carbon of the terminal methyl group) and the micelle COM. When this angle is zero, the chain is aligned parallel to the micelle radial axis and when this angle is 90°, the SDS molecule has been dislodged from the micelle structure and the chain is at a tangent to the micelle surface. The chain angle distributions were produced by calculating the angle between the vectors defined above for every SDS molecule in every snapshot of the trajectory. The

SDS headgroup tilt angle has also been calculated, which is defined as the angle between the vector formed between S (the sulphur atom in the SDS headgroup) and C1 atoms, and the vector formed between C1 and C12 atoms. When this angle is zero, the entire molecule is aligned linearly and when this angle is 90° the headgroup is oriented such that it is perpendicular to the SDS hydrocarbon chain. The distribution of this angle has also been calculated in the same manner as described previously for the SDS chain angle.

7.2.2 Solubilisation of TP

To understand how the SDS micelles solubilise the TP molecules a useful property to calculate is the preferred position of a TP molecule with respect to the micelle. In order to realise this, the minimum distance between the O1 atoms of the TP molecules and the sulphur in any SDS molecule can be calculated as a function of time. Then, to obtain a statistical description of the position of TP molecules in relation to the micelle, the probability that a given heavy atom (non-hydrogen) in the SDS molecules is closest to an oxygen atom in TP was calculated.

7.2.3 Interfacial Properties of Micelles

Finally, interfacial effects of micelles have considerable influence on the ability of solutes to penetrate through the micelle surface and into the hydrophobic core. In order to characterise the interfacial interactions between the various molecular constituents of the micellar systems and the aqueous environments, radial distribution functions, $g(r)$, are used. Radial distribution functions describe the probability, relative to an ideal gas, of finding a neighbour atom within a distance r of a central species. From these $g(r)$, the number of hydration water molecules per surfactant is calculated using the same method as the one used for the monolayer simulations, as described in Chapter 3.

In the previous three chapters, results have been reported from simulations of dodecyl sulphate monolayers which have been used to model the interface of surfactant micelles. These simulations have revealed some interesting differences in the interfacial properties of monolayers with different ions. They have also shown that the orientational behaviour of testosterone-based drug compounds within monolayers is affected by the number of polar interaction sites contained within the drug molecules. In the next chapter, results are presented from MD simulations of SDS micelles with and without the presence of TP as this surfactant-drug pairing was found to be the most successful formulation of those studied by *Saaka* [32].

Chapter 8

Solubilisation of Testosterone Propionate within a Sodium Docecyl Sulphate Micelle

This chapter is based on the following two publications;

- Atomistic Description of the Solubilisation of Testosterone Propionate in a Sodium Dodecyl Sulfate Micelle. Allen *et al*, (2014) J. Phys. Chem. B. 118 (46), 13192–13201
- A novel method for constructing continuous intrinsic surfaces of nanoparticles. Allen *et al*, (2017), Submitted to *The Journal of Molecular Modeling*

8.1 Introduction

A wide-range of surfactants have been investigated as the building blocks of nanoscale drug delivery vehicles due to the solubilising ability of the self-assembled structures that they form (see [14–16] and the references within). Specifically, sodium dodecyl

sulphate (SDS, $SO_4(CH_2)_{11}CH_3$, shown in Figure 7.1a) has a relatively low toxicity compared to other surfactants and is used for many industrial applications including in the pharmaceutical industry as a wetting and solubilising agent in tablet formulations.

Numerous research groups have applied experimental techniques to characterise the solubilisation of various drug molecules within SDS micelles. Krishna and Flanagan used UV detection to determine that SDS significantly solubilises the antimalarial drug, β-arteether [146]. On the other hand, Rangel-Yagui *et al.* observed that SDS is less effective than non-ionic or cationic surfactants with the same hydrocarbon chain length in solubilising ibuprofen [147]. Mall *et al.* measured the free energy of adhesion between four different sulphanmides and the head and tail groups of SDS using contact angle data, and found that the most favoured interaction was adhesion to the SDS tails, as opposed to an interaction with the headgroups [148]. A similar finding has been presented as a result of the conductivity, spectroscopy and surface tension measurements carried out by Göktürk and Aslan that show an increase in trimetoorim binding as the length of the hydrocarbon chain in sulphate anionic surfactants increases, which led them to hypothesise that the increased binding is due to there being more hydrophobic volume for the drug molecules in the micelles [149]. Whereas, Enache *et al.* used UV-vis adsorption and voltammetry experimental results to develop the hypothesis that the anticancer drug, mitoxantrone, is located in the micelle surface layer as a result of both electrostatic and polar interactions playing an important role in the binding of the drug to SDS micelles [150].

Since SDS aggregates in aqueous environments have spatial length scales which are typically a few nanometers, it is challenging for experimental research to capture a direct view of the poorly water soluble substance under investigation. Furthermore, details regarding micellar structure on an atomic scale are hardly accessible by experimental techniques. However, molecular dynamics (MD) simulations have been utilised to study many surfactant aggregate systems including SDS. In these studies,

MD simulations provide an important compliment to experimental studies because they yield atomistic level insight into the structure and dynamics of the surfactant systems. Atomistic detail can provide insight on interactions between specific atoms or functional groups which in turn can be used to form a physical explanation for the qualitative behaviour observed. If we can probe the interactions which result in the solute's positioning then we can also predict the preferential position of other solutes in micelles and assess the practical potential of a given drug delivery vehicle.

A significant amount of simulation work has been carried out over the years investigating various structural, interfacial and kinetic properties of SDS micelles using MD simulations. The first simulation study of a SDS micelle was published in 1990, in which a 182 ps simulation showed that a micelle containing 42 SDS molecules was spherical in shape and an initial investigation of the structural and interfacial properties of the micelle was carried out [151]. In 1995, MacKerell published the results of a 120 ps simulation of a micelle consisting of 60 SDS molecules, which showed that it was spherical in shape also and that both headgroup atoms and terminal carbons were present at the micelles interface with water [152]. Bruce *et al.* conducted a 5 ns simulation of a micelle with 60 SDS molecules which resulted in them finding a slightly non-spherical micelle. They measured the surface area of the micelle, the orientation of the SDS chains within the micelle and the interactions between the SDS headgroup and water and Na^+ ions at the micelle's interface [142, 153]. Since these four initial simulation studies, various simulation studies have been conducted studying the interfacial properties of SDS micelles in an aqueous environment [112, 154–157], as well as the effect that the type of counter ion [112], the concentration of ions in the system [114] and the number of SDS molecules in a micelle [158] has on the structural and interfacial properties of the micelles. Some work has been done to study the aggregation of SDS micelles at high SDS concentrations ($\sim$ 1M) [114, 159]. Recently, a comparison of the various forcefields that exist to study SDS micelles in an aqueous environment has been reviewed and

found that only for large (aggregation number of $\sim$ 100 SDS molecules) micelles does the forcefield have a significant difference [160].

Despite the abundant use of MD simulations to study the structural and interfacial properties of SDS micelles, there is a distinct lack of work regarding the solubilisation properties of drug molecules within SDS micelles. Yan *et al* [161] assessed the structural and dynamical aspects of the solubilisation process of pyrene within a sodium dodecyl sulphate micelle using MD simulations. They observed that a free pyrene fluorescence probe was spontaneously solubilised into the SDS micelle and preferentially resides in the hydrophobic core region. As the local concentration of pyrene was increased, two probe molecules could enter the hydrophobic core region and an excited dimer of pyrene molecules was formed, which shortly separated and the pyrene molecules were later found to be distributed in the micelle palisade layer. More recently, groups have been utilising the structure of surfactant (including SDS) micelles in combination with COSMOmic to determine the partitioning and free energy of adsorption of drug molecules within the micelles, which allows for a relatively fast way of determining the most probable location of a drug molecule but does not provide any direct information regarding the interactions which govern the encapsulation of the drugs within the micelle [125, 162].

In this chapter, results are presented from large scale all-atom MD simulations of SDS micelles with and without testosterone propionate (TP). TP is a steroid which is used in hormone replacement therapy. Little is known regarding the interactions between TP and the solubilising agents used to enhance its aqueous solubility, in particular the location of solubilised TP in relation to an SDS micelle is unknown. The chemical structure of TP consists of both hydrophobic and hydrophilic functional groups and as a result, the location of solubilised TP in a micelle is difficult to predict. Moreover, testosterone has several analog compounds, such as testosterone enanthate, which have different functional groups but comparable molecular weights. The study of this group of compounds should provide insight into the key

Table 8.1: Average values of various structural properties of the SDS and the SDS+TP micelles calculated from the production simulation periods. The quoted errors are one standard deviation of the data distributions.

	SDS micelle	SDS+TP micelle
Eccentricity	0.11 ± 0.07	0.16 ± 0.08
I_x/I_y	1.01 ± 0.17	1.03 ± 0.18
I_x/I_z	1.04 ± 0.20	1.18 ± 0.29
I_y/I_z	1.04 ± 0.18	1.15 ± 0.28
Max l_x (Å)	48.06 ± 4.98	48.22 ± 5.81
Max l_y (Å)	48.21 ± 4.37	49.75 ± 5.67
Max l_z (Å)	49.18 ± 5.01	53.15 ± 6.06
SASA/molecule (Å^2)	169.9 ± 4.5	156.1 ± 4.2
Total SASA (Å^2)	13592.8 ± 358.2	13734.9 ± 371.6
Voronoi Surface Area/molecule (Å^2)	149.7 ± 2.6	136.9 ± 2.2
Total Voronoi Surface Area (Å^2)	11972.1 ± 206.6	12181.2 ± 193.5

interactions which govern solubilised position of solutes in micelles.

The influences of TP on micelle structure, shape and interfacial properties is investigated as it is solubilised into a SDS micelle. A detailed description of the TP solubilisation process is also provided.

8.2 Results and Discussion

In this section, results are presented from all-atom simulations of the SDS and SDS+TP micelle systems described in Chapter 7. First, the effect of TP on micelle shape and structure is discussed, followed by a detailed description of the TP solubilisation process and finally, the change in the interfacial properties of the SDS micelle due to the presence of TP is presented. Table 8.1 contains a summary of the results.

8.2.1 Effect of TP on SDS Micelle Shape and Structure

The solvent accessible surface area (SASA) is shown for the SDS and SDS+TP micelle systems in Figure 8.1. The SASA values remain stable during the simulations indicating that the systems are in equilibrium throughout the majority of the pro-

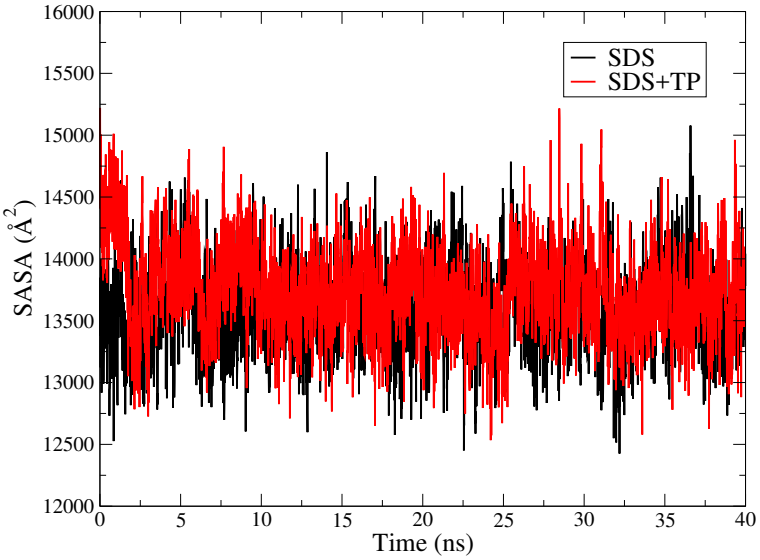

Fig. 8.1: The solvent accessible surface area of the SDS (black) and SDS+TP (red) micelle systems as a function of time.

duction stage of the simulation. The average SASA per molecule for the SDS and the SDS+TP micelle systems is 169.9Å^2/molecule and 156.1 Å^2/molecule respectively. Note that the value for SASA/molecule calculated from the SDS+TP micelle includes contributions from the drug molecules which are bound to the micelle surface. This was done in order to not report a value that could be misleading. If it was calculated merely from the SDS molecules it would include artificial voids from where the TP was located and therefore overestimate the SASA.

The SASA measurements are very sensitive to the size of the probe used so in order to remove this dependence, the surface area of both micelle systems was also calculated using the Voronoi tesselation method. The surface areas determined from the Voronoi tesselation yielded smaller surface area values than those calculated with SASA, as shown in Table 8.1. This result is expected since the Voronoi surface area measurements will be less sensitive to the roughness of the interface than those from SASA. Also, the Voronoi and SASA surface areas show that the surface area per molecule decreases with the inclusion of TP in the micelle. The Voronoi surface area was separated into contributions from head, tail and TP regions of the micelle

systems which were plotted as a function of time in Figure 8.2. From these measurements, it has been determined that 42% of the surface area of the SDS micelle is due to headgroup atoms, while 58% of the surface area is due to the hydrocarbon tails. Whereas, in the SDS+TP micelle, 39%, 45% and 16% of the surface area is due to the SDS headgroups, SDS hydrocarbon chains and TP molecules, respectively. The ratios of surface area contributions of head to tail are 0.72 and 0.87 for the SDS and SDS+TP micelles respectively.

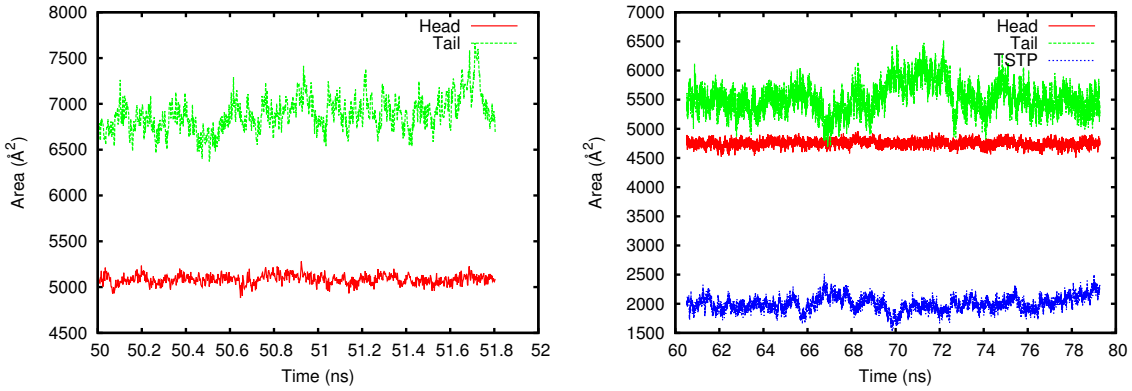

(a) **(b)**

Fig. 8.2: The Voronoi surface area contributions from head (red), tail (green) and TP where applicable (blue) of the SDS and SDS+TP micelles as a function of time.

The micelle shape is dynamic throughout the production periods in both simulations which is suggested by the eccentricity values typically fluctuating between 0.01-0.3. The average eccentricity values indicate that while the SDS and SDS+TP micelles have the same general shape, the SDS+TP micelle is slightly less spherical than the SDS micelle. This is supported by the average values for the ratios of the moments of inertia of the micelles, which are slightly larger for the SDS+TP micelle in accordance to the larger average eccentricity. The average values for the maximum micelle dimensions in the x and y directions are very similar for both micelle systems however, the maximum dimension in the z direction is 4 Å larger for the SDS+TP micelle.

The SDS chain angle distributions for both simulations are shown in Figure 8.3a

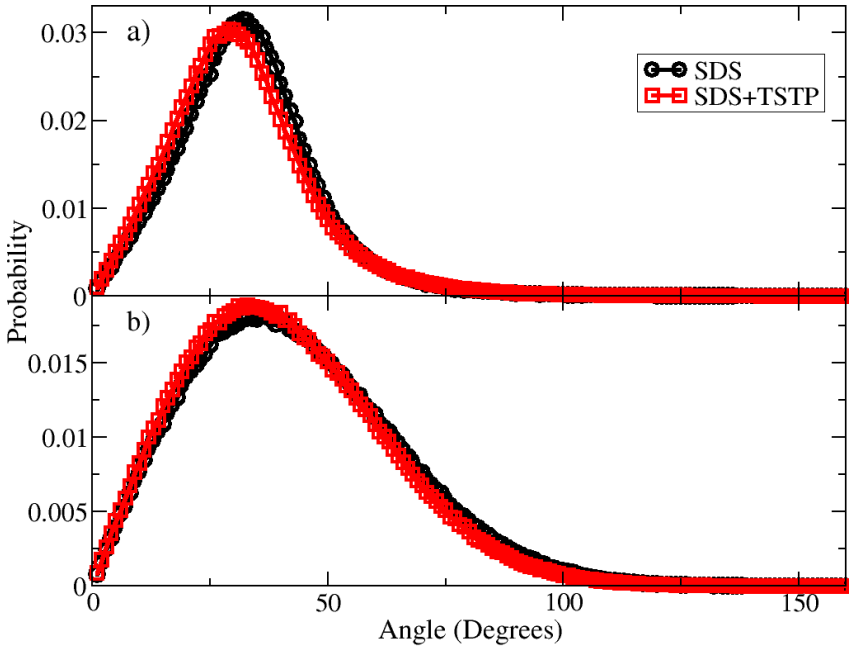

Fig. 8.3: a) Probability distributions of the angle formed between atoms C12 and C1 of the SDS molecule (as shown in Figure 7.1a) and the micelle centre of mass for the SDS and SDS+TP micelle systems. b) Probability distributions of the headgroup tilt angle formed between atoms S, O and C12 in the SDS molecule for the SDS and SDS+TP micelle systems.

and reveal that the mean chain angles for the SDS and SDS+TP micelles are 33.1° and 31.8° respectively. It was concluded that the presence of TP causes no statistical difference between the mean chain angle distributions calculated for the micelles. The SDS headgroup tilt angle distributions were also calculated and are shown in Figure 8.3b. These show that the presence of TP has almost no effect on the distribution of headgroup tilt angle either. The mean headgroup tilt angles are almost equal at 42.9° and 41.1° for the SDS and the SDS+TP micelles respectively.

Radial density plots provide a more detailed view of the internal and external micelle structures. Figures 8.4a and 8.4b show the average density of the different chemical species that are found in SDS, water and TP molecules. The plots reveal that the average micelle radius is approximately the same for both simulations, d_{cm} ~2 nm which is consistent with a study conducted by Bruce *et al.*[153] on an SDS micelle with an aggregation number of 60. The average micelle radius is also

consistent with the estimate provided by taking the average of the mean values for the maximum dimensions of the micelle in the x, y and z directions which would give the diameter, and then dividing by two to get the radius.

The radial density plots generally show that the monomers are arranged such that the headgroups are in contact with the water whereas the tails are contained in the micellar core forming a hydrophobic environment. Water penetration into the micelle core has been studied using the method used by Bruce *et al.* [142] and reveals water penetration of 14.5 Å and 15.5 Å away from the micelle centre of mass for the SDS and SDS+TP micelles respectively. Additionally, the contact between water molecules and the hydrocarbon tails in the micelle is described by shell regions of 9 Å and 10 Å for the SDS micelle and the SDS+TP micelle, respectively which suggests that the presence of TP has the very slight effect of drawing water into the micelle interior. The radial density plots can also be used to estimate the position of TP molecules in relation to the micelle centre of mass. The oxygen atoms in TP have a very broad density distribution, the peak of which is visible in the inset plot in Figure 8.4b and is situated at $d_{\mathrm{cm}} = 16.5$ Å. This distribution is very broad and spans from the micelle core to the surrounding water region. It is therefore difficult to say, to any great degree of certainty, where the TP molecules preferentially reside based upon the radial density plots alone.

The ability to accurately characterise the location of the TP molecules within the SDS micelle is crucial, given that the encapsulation capacity of an aggregate is directly related to the volume of the preffered region of the solute species. The inconclusive result from the radial density measurements provided the motivation to calculate the intrinsic density profiles of the SDS+TP system (Figure 8.5) to give more insight on the structure of the various different atomic species with respect to the micelle interface.

The intrinsic density of oxygen atoms in water molecules, Ow, is shown by the blue curve in Figure 8.5. At sufficiently large distance values, the number density

of Ow atoms converges to 0.033 $Å^{-3}$ corresponding to a density of 1 g/mL, which is consistent with the known bulk density of water. The intrinsic density profile of Ow atoms differs somewhat from the radial density in that it exhibits a small interfacial peak located at $d_{\text{int}} = 3.5$ Å. This peak corresponds to the attraction between the polar water molecules and the highly charged micelle surface. This is a subtle yet important structural feature which is undetected by the radial density plot.

The position of TP molecules was also studied in more detail by calculating the intrinsic density of the carbon atoms within them, as shown by the black curve in Figure 8.5. The density of C_{TP} vanishes at large distances and thus it is deduced that TP is not found at large distances away from the micelle in the bulk water. Then as d_{int} decreases, the C_{TP} density begins to increase gradually until it peaks within the micelle interior at $d_{\text{int}} = -6$ Å. Whilst the broad radial density profile for oxygen atoms in TP molecules suggests that TP molecules are present both inside and outside the micelle interior, the intrinsic density of TP molecules decreases to 0 $Å^{-3}$ at $d_{\text{int}} = 0$ which shows that the TP molecules are in fact situated in the micelle's palisade layer between the hydrophilic heads and the first few carbon atoms of the hydrophobic chains, not in the bulk water. Overall, the intrinsic density plots suggest the same basic micelle shape and properties as those determined from the radial density, however they also contain more detail about the structure of atomic species at the interface which is particularly useful for describing the interfacial water structure and the location of the TP molecules.

8.2.2 Water Orientation

The structure of interfacial water molecules is highly relevant to the study of encapsulation properties of micelles. Solutes must overcome an energy barrier which arises from the highly ordered water structure in the vicinity of the micelle. Studying the structure of water surrounding the micelle could provide some indications as to the

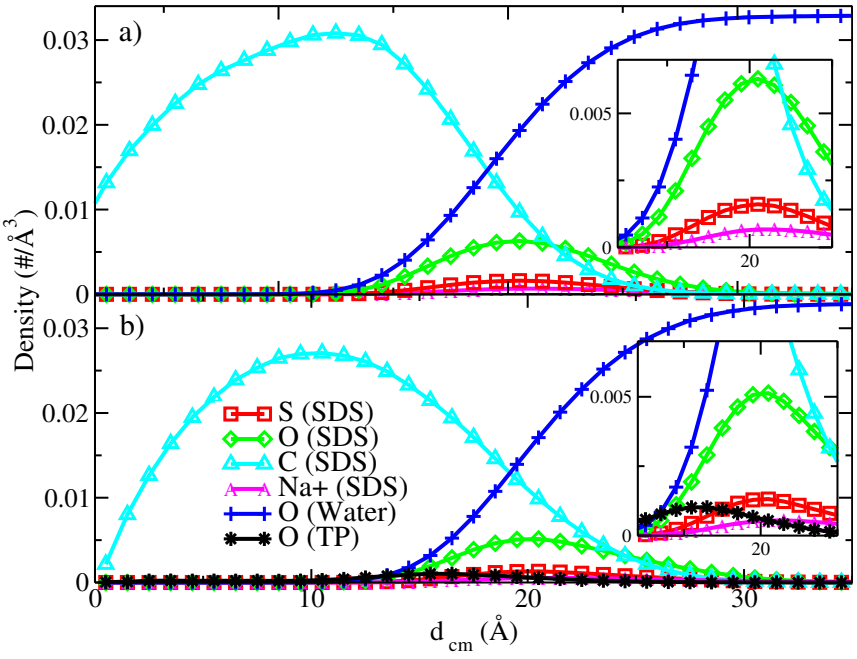

Fig. 8.4: Radial density plots of the different chemical elements within the SDS, TP and water molecules with respect to the centre of mass of the a) SDS and b) SDS+TP micelles. The inset plots magnify the interfacial region of the plots for clarity.

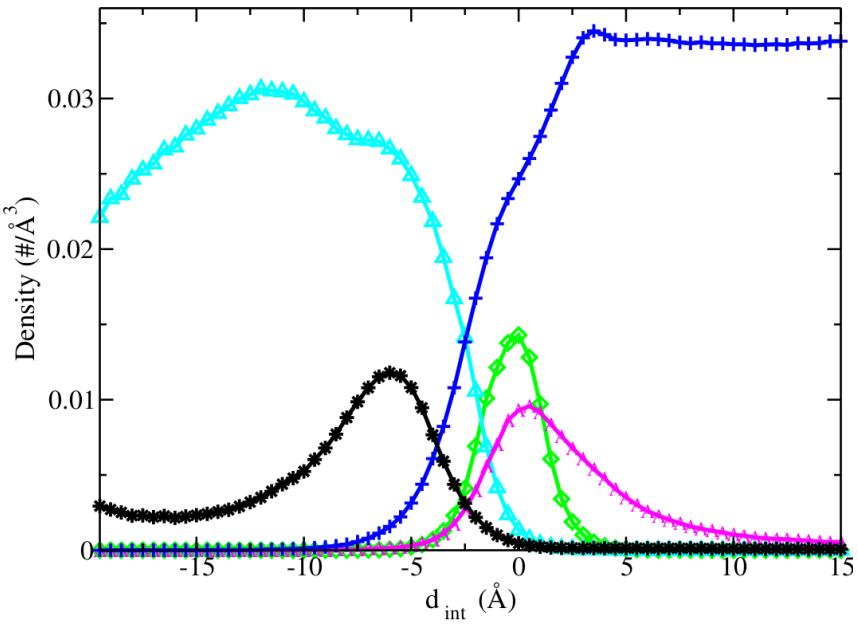

Fig. 8.5: The intrinsic density profiles for the SDS+TP micelle system, in which the colours green, cyan and magenta are used to depict the density of oxygen, carbon and sodium atoms in SDS respectively. Blue and black are used to show the density of oxygen atoms in water molecules and carbon atoms in TP respectively. Note that the density of Na^+ has been multiplied by ten to improve clarity.

micelle's potential as a solubilising agent. The orientation of water molecules was investigated by studying both the radial and the intrinsic water orientation probability profiles of the SDS+TP micelle, as outlined earlier in Section 7.2.1.6 in Chapter 7. The radial and intrinsic water orientation profiles are shown in Figures 8.6a and 8.6b respectively. In both of these plots, the x-axis represents the distance (d_{cm} or d_{int}) and the y-axis represents $\cos(\theta)$, where θ is the water dipole angle with respect to the vector pointing from $\mathbf{c}_{\mathrm{m}}$ to the Ow atom. Note that the integral of the probability density over $\cos(\theta)$ for a fixed value of the distance variable is normalised to 1.

The radial water orientation profile, Figure 8.6a, shows that for large distances away from the micelle, water molecules have no orientational preference when averaged over many snapshots. This is because the interaction with the charged micelle interface is very weak at large distances. This explains the approximately flat distributions of $\cos\theta$ at values of $35 \leq d_{\mathrm{cm}} \leq 50$. As the value of d_{cm} decreases, the orientation of the water molecules is significantly affected by the interaction with the electric field arising from the micelle surface. This is evident from the yellow region at $\cos\theta \sim -0.9$, $d_{\mathrm{cm}} \sim 35$ Å. This corresponds physically to an increased tendency of water molecules to orient their dipoles such that the Hw atoms are closer to the micelle surface than the Ow atoms. This effect becomes more prominent as d_{cm} decreases further as is clear from the broad red region in the vicinity of the micelle interface: $18 \leq d_{\mathrm{cm}} \leq 30$. As d_{cm} decreases further still, the distribution shifts back towards larger values of $\cos(\theta)$ as seemingly water molecules which have penetrated through the micelle interface attempt to reorient to allow favorable interactions between Hw atoms and surfactant headgroups. It seems from Fig. 8.6a that this reorientation affects water molecules as close as 8 Å away from $\mathbf{c}_{\mathrm{m}}$, shown by the yellow/green section on the far left of the plot, this would correspond to molecules which are ~ 14 Å deep in the micelle core.

Inspection of the intrinsic water orientation profile reveals qualitatively similar

behaviour to that arising from the radial water orientation profile. At large values of d_{int}, corresponding to large distances away from the micelle surface, the distribution of water molecule orientations is flat as one would expect. Whilst the intrinsic water orientation profile also predicts the reorientation of water molecules in the vicinity of the micelle interface, it occurs over a much smaller distance range: $0 \leq d_{\text{int}} \leq 5$ Å. This region exhibits a comparatively sharp probability density peak, shown by the bright red region in Figure 8.6b, located at $\cos\theta = -0.9$, $d_{\text{int}} = 2.5$ Å. The location of this peak is in direct correspondence with the location of the interfacial water peak in the intrinsic density profile as one would expect. The smaller distance range in which the reorientation occurs results in a v-shape trend where the probability density is severely skewed towards smaller values of $\cos\theta$ and then skewed back in the opposite direction. Interestingly, the intrinsic water orientation profile shows that the effect of the interface on the reorientation of water molecules is highly localised to those in the vicinity of the interface. At $d_{\text{int}} \leq$ -5 Å, the water orientation probability density distribution is more or less flat like in the bulk water. It seems then that the radial water orientation profile, in this instance at least, overestimates the range of interaction in which the orientation of water molecules is affected by the charged micelle surface which illustrates another instance in which the micelle intrinsic surface is an advantageous tool for analysis.

8.2.3 Surface Curvature Lifetimes

Prior to this study, local Gaussian curvature had yet to be incorporated into analysis of micelles in the literature. Here, this is utilised as an additional way of characterising micelle shape and dynamics. A curvature tolerance of 0.05 Å^{-1} was used for the SDS+TP micelle system as this encompassed regions of the surface that were highly curved, yet contained a sufficient number of examples for adequate statistics to be collected.

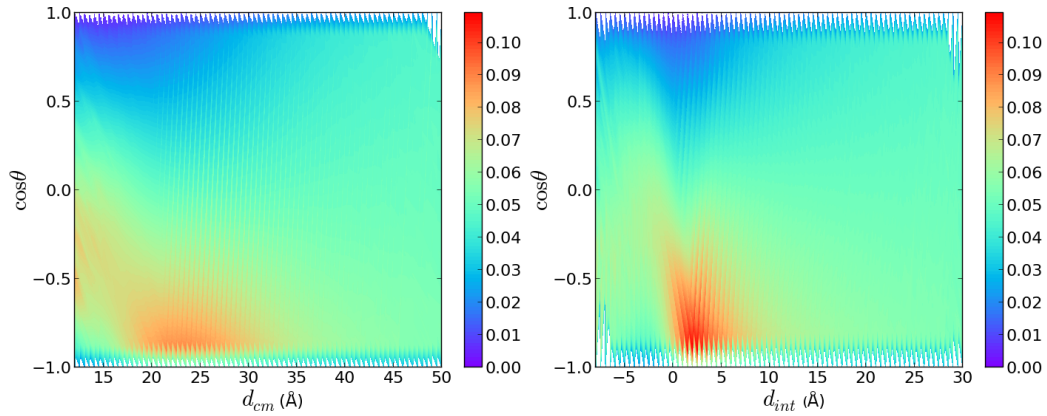

(a) Radial water orientation profile **(b)** Intrinsic water orientation profile

Fig. 8.6: Probability density plots for a) the radial orientation and b) the intrinsic orientation of water molecules. The negative values of the d_{int} variable in b) correspond to locations within the micelle interior.

The curvature lifetime can be thought of as the time taken for a surface point, which has an absolute value of curvature equal or greater than the tolerance, to decrease to 0. Histograms have been produced, Figure 8.8, that show the probability of different curvature lifetimes for concave/convex points (black curve) and saddle points (red curve) throughout the production simulation. As curvature lifetime increases, the curves in Figure 8.8 increase sharply from 0 to peaks in probability at values of 0.6 ns and 0.8 ns for concave/convex and saddle regions respectively. As the lifetime increases further, the curves decrease exponentially and tend towards 0 at large values. The probability of a highly curved surface region existing for longer than 8 ns is practically negligible (2.5×10^{-3}).

In general, the typical lifetime of a region of high curvature is fairly small at less than 10 ns, however saddle points appear to be more stable than concave/convex regions with a slightly larger peak lifetime and a higher probability of moderate lifetimes as shown by the red curve exhibiting larger probability values within the range $\sim$ 2.0-4.5 ns. For lifetimes $>$ 5 ns, the two curves coincide almost exactly.

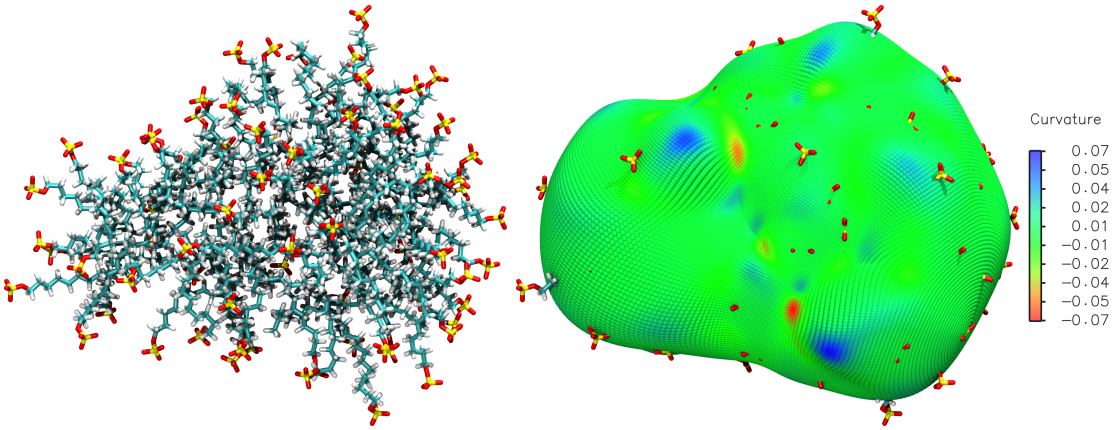

(a) (b)

Fig. 8.7: a) The final snapshot in the production simulation of the SDS+TP micelle. Atoms with the colours cyan, grey, red and yellow are used to represent the elements: carbon, hydrogen, oxygen and sulphur in SDS molecules respectively. TP molecules are omitted from this image for clarity. b) The micelle intrinsic surface superimposed over the last configuration of the production simulation. The colour of the surface represents the local Gaussian curvature, as defined on the colour scale bar on the right.

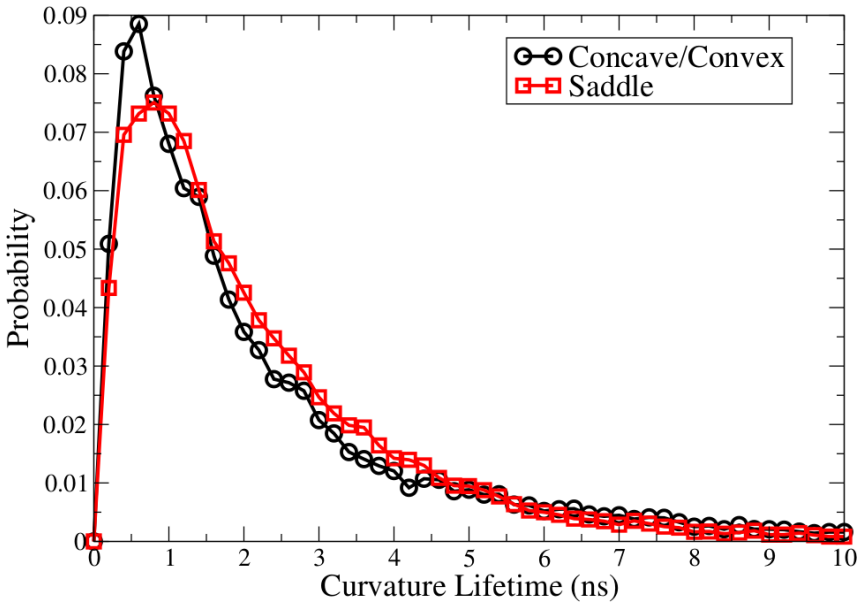

Fig. 8.8: Probability histograms of curvature lifetimes in units of nanoseconds for both convex/concave and saddle points.

8.2.4 Atomistic Description of the Solubilisation Process of TP into an SDS Micelle

The first step in understanding how the SDS micelles solubilise the TP molecules is to establish the preferred position of a TP molecule with respect to the micelle. Figure 8.9a shows the minimum distance between the O1 atoms of the TP molecules and the sulphur in any SDS molecule as a function of time. Most of the O1 atoms in TP molecules are found at a distance of $\sim$ 4-10 Å from a sulphur atom for the entirety of the production period. From visual inspection of the trajectory, it is observed that most of the TP molecules are oriented such that the major axis is at a tangent to the micelle surface and the SDS headgroups are very dynamic. The TP molecules are typically located between numerous SDS headgroups that periodically sway towards and away from the TP resulting in the $\sim$ 6 Å fluctuations in the distances between TP and the nearest SDS molecules as shown in Figure 8.9a. All but one of the TP molecules are bound to the SDS micelle from the beginning of the production simulation and the one unbound TP molecule adsorbs to the micelle's surface after 45 ns which is evident by the orange curve which fluctuates significantly throughout the first 45 ns of the trajectory and then reaches the same value of $\sim 4-10$ Å. For this reason that particular TP molecule is only used for the remaining analysis after the point that it adsorbs to the surface of the micelle.

Figure 8.10 shows the probability of a heavy atom in SDS being closest to O1 and O2 atoms in TP. This shows that O1 and O2 atoms in TP are most likely to be situated nearest to the SDS headgroup, with a sharp decrease in probability at C1 and then a gentle decay as one moves further down the SDS carbon chain before a slight rise at C11 and C12, the terminal carbons. The probability of sulphur being the closest heavy atom in SDS to any of the oxygens in a TP molecule is zero due to the steric and electrostatic energy barriers arising from the three oxygens which surround it. TP-O3 is most likely to be closest to C12 in SDS but has very low

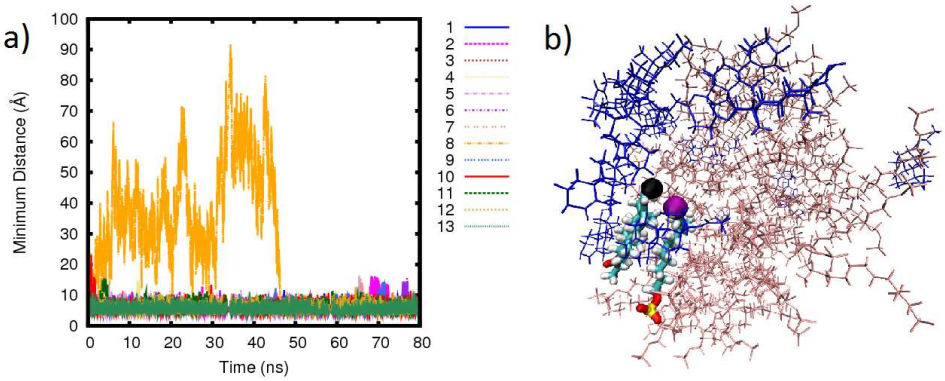

Fig. 8.9: a) The minimum distance between any sulphur atom in a SDS molecule and the O1 atom of each TP molecule as a function of time. The plot shows that one of the TP molecules does not adsorb to the micelle's surface until after 45 ns. The different colours represent individual TP molecules. b) Snapshot of an instance when the O1 atom of a TP molecule is closest to a C12 atom in a SDS molecule, which is at the surface of the micelle. The SDS and TP molecules are represented by pink and blue lines, respectively. The purple and black spheres represent the C12 on the SDS molecule and the O1 atom on the TP molecule, respectively.

probability of being closest to the headgroup. This corresponds to TP molecules interacting with the SDS hydrocarbon tails which are situated within the interfacial region of the micelle (as is shown in 8.9b), and do not represent TP molecules penetrating into the micelle core.

The three oxygen atoms have been identified as the most prominent interaction sites in the TP molecule due to their increased polarity, and thus hydrogen bonding capabilities, compared to the nonpolar carbon rings. For this reason the oxygen atoms in TP have been used to probe interfacial properties of the drug. Radial distribution functions ($g(r)$) between the oxygen atoms in the TP molecules and oxygen atoms in water molecules (Ow) have been calculated and are presented in Figure 8.11a. The O1-Ow and O2-Ow $g(r)$ curves show large sharp peaks between 2 and 3 Å indicating that water molecules are hydrogen bonding to these oxygen atoms on the TP molecules, however O3 has a small peak at a much larger distance ($\sim$ 4.5 Å) that is probably due to the water molecules hydrogen bonded to the O2 atom on the TP molecules. This is not surprising when one considers the position

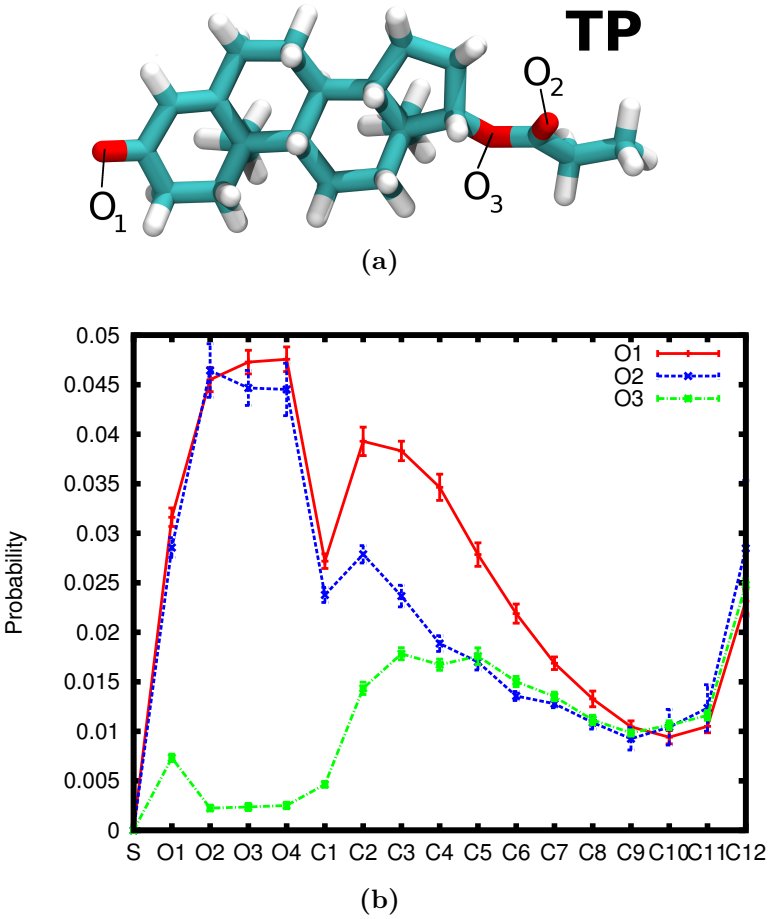

(a)

(b)

Fig. 8.10: a) The chemical structure of TP. The atoms O1, O2 and O3 are labelled b) The probability distributions of the closest SDS heavy atoms to each oxygen atom on a TP molecule, which has adsorbed to the micelle's surface.

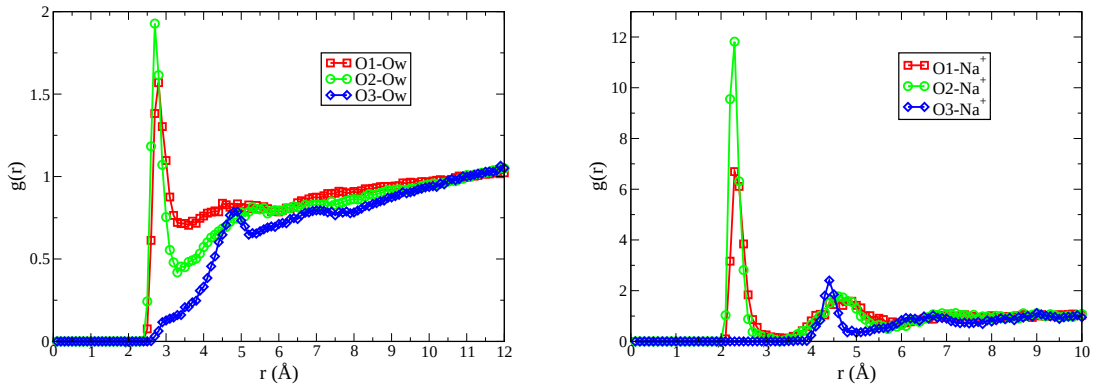

(a) TP-Water **(b)** TP-Na^+

Fig. 8.11: Radial distribution functions between oxygen atoms in TP molecules and a) Ow atoms, b) Na^+ counterions in the SDS+TP micelle simulation.

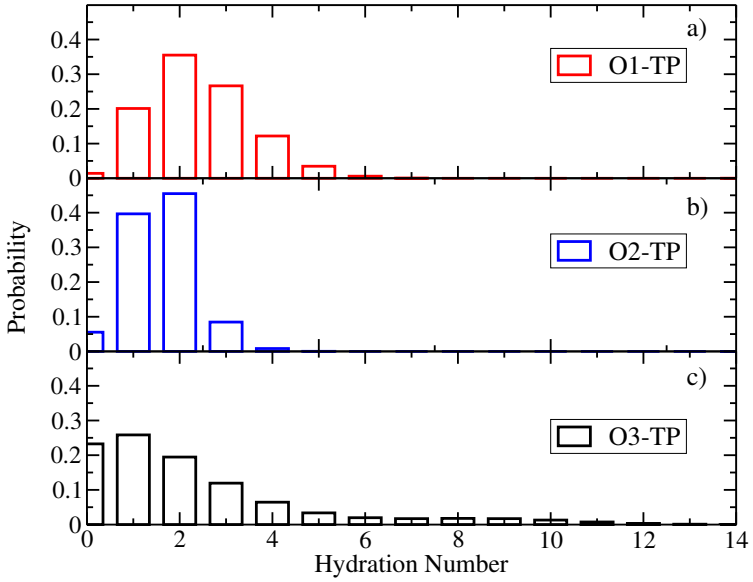

Fig. 8.12: Histograms showing the fraction of a) O1, b) O2 and c) O3 atoms in the adsorbed TP molecules that have a given hydration number.

of O3 in the TP, it is less exposed than O1 and O2 and it has one more covalent bond, as shown in Figure 7.1b in Chapter 7.

The mean number of hydrating water molecules around the O1, O2 and O3 atoms in the TP molecules were found to be 2.4 ± 1.1, 1.6 ± 0.8 and 2.2 ± 2.4, respectively. From these values alone, one might naively think that O3 is more hydrated than O2, which is counter intuitive. However this is rationalised when considering that the nearest neighbour distance of O3 is 2 Å larger than that of O2 and thus a larger volume is measured resulting in a misleadingly large hydration number. To put this into perspective, the number of hydration water molecules per unit volume (in $Å^3$) for O2 and O3 are 1×10^{-2} and 6×10^{-3} respectively. Probability histograms of the number of hydration water molecules around the oxygen atoms in the TP molecule are displayed in Figure 8.12 and show that the second most probable hydration number for O3 is zero, further illustrating its limited hydrogen bonding capabilities.

To determine whether the TP molecules have a preferential orientation with respect to each other, the TP molecule was divided up into various segments, which are shown in Figure 8.13a, and the shortest displacements between these segments on

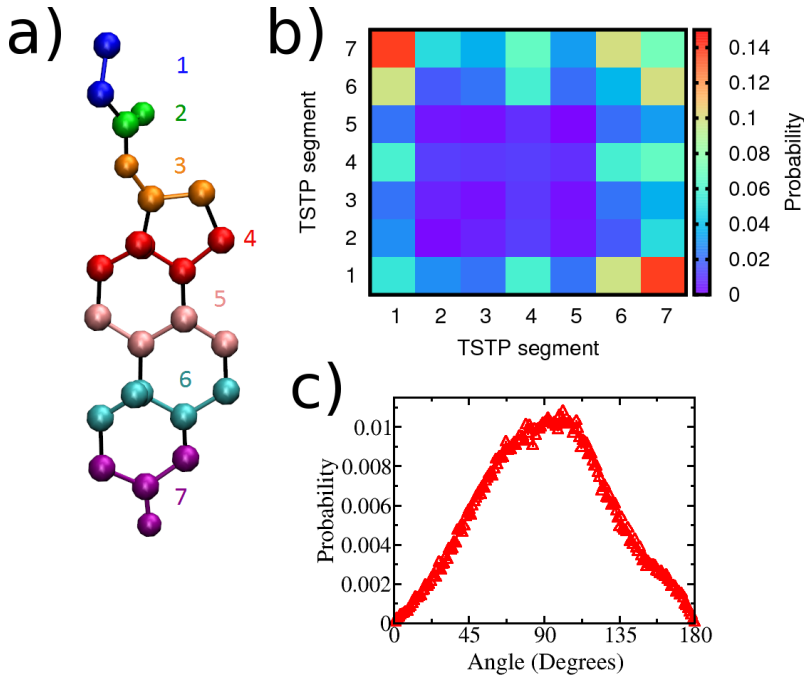

Fig. 8.13: a) Colour-coded picture of the segments of the TP molecules that have been used to describe the association of TP molecules. b) Histogram showing the probability that two neighbouring TP molecules associate via a pair of segments as defined in a). c) Probability distribution of the angle formed by the vectors between O1 and O2 atoms in nearest neighbour TP molecules.

nearest neighbour TP molecules were calculated. Figure 7.1b shows the probability of every different segment pairing and reveals that the most probable segment pairing is 1 and 7 indicated by the red squares in opposite corners of the plot. This suggests that the TP molecules prefer to be aligned in a head to tail fashion. In order to further understand the orientation of TP molecules with one another, the angle formed by the vectors between O1 and O2 atoms in nearest neighbour TP molecules was calculated. Figure 8.13c shows the probability histogram of the angles found between nearest neighbour TP molecules and exhibits a broad curve centred at $\sim 91°$. Therefore, the preferred orientation of two TP molecules are such that they are aligned with the head of one molecule (Segment 1) is nearest to the tail (Segment 7) of another molecule and they are oriented such that there major axes are perpendicular to one another.

From visual inspection of the trajectory, it is observed that the TP molecules

initially adsorb to the surface of the SDS micelle in a dense cluster, but as time evolves they gradually start to migrate until they are approximately evenly distributed around the shell. This is quantified by the plots in 8.14 which show the TP centre of mass locations, described by (θ, ϕ), where θ and ϕ denote the azimuthal and zenith angles respectively. θ is the projection onto the x-y plane of the vector from the origin to the centre of mass of a TP molecule, this angle goes clockwise around the x-y plane from 0 - 360°. ϕ is the angle between the z-axis and the vector to the centre of mass of a TP molecule, this angle ranges from 0 to 180 degrees which correspond to vectors pointing in the positive and negative z directions respectively. Both θ and ϕ are measured relative to the micelle centre of mass coordinate frame. Figure 8.14a shows that initially the TP molecules are clustered in dense groups leaving large regions of the micelle's surface unpopulated. In particular, there is a large void at the top of the plot in the centre which corresponds to a large proportion of the bottom hemisphere of the micelle as pictured. Figure 8.14b reveals that in a later stage of the simulation, the blank regions of sampling are more disperse and the data points are more equally distributed over the zenith angles.

8.2.5 Effect of TP on SDS Micelle Interfacial Properties

In order to study the effect of TP on micelle interfacial properties, a variety of $g(r)$s have been calculated to describe the interactions between the SDS molecules and their aqueous environments, and these are shown in Figures 8.15-8.16. The nearest neighbour distance for the oxygen and hydrogen atoms of the water molecules around the sulphur atoms in the SDS headgroup remains unchanged in the presence of TP. The calculated nearest neighbour distances for S-OW and S-HW are 4.8 Å and 3.5 Å respectively which are consistent with other values calculated from similar studies of SDS micelles [159]. This also shows that the interfacial water molecules orient themselves such that the hydrogen atoms are closer to the surfactant head-

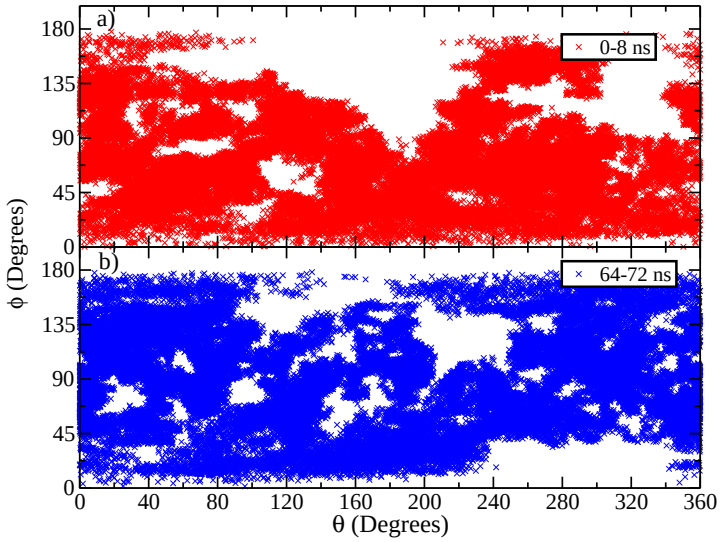

Fig. 8.14: Plot of the location of the centre of mass of the TP molecules as a function of the azimuthal θ and zenith ϕ angles around the surface of the micelle at a) an initial part of the simulation (0 - 8 ns) and b) towards the end of our simulation (64 - 72 ns).

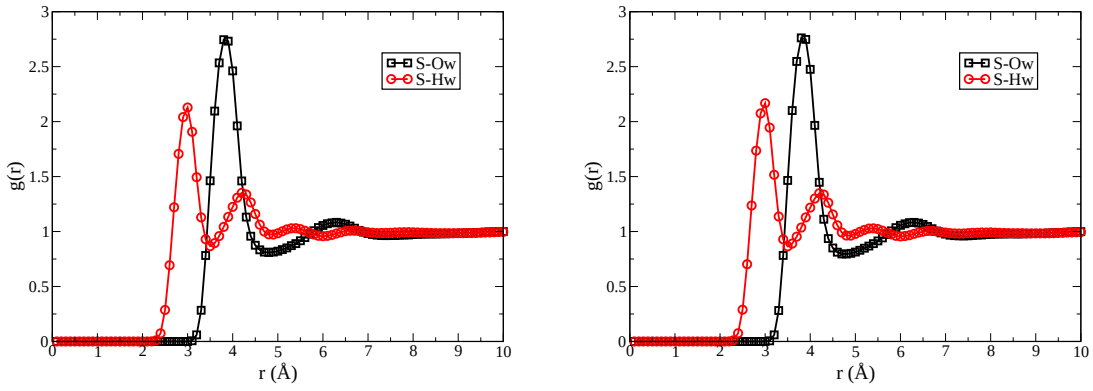

(a) SDS **(b)** SDS+TP

Fig. 8.15: Radial distribution functions between sulphur atoms in SDS and water molecules for the SDS and SDS+TP micelles.

groups than oxygen. Figure 8.17 shows histograms of the number of hydration water molecules for the two micelle systems. The distributions are almost identical suggesting that the presence of TP does not affect the hydrogen bonding network around the interfacial region and this is confirmed by the mean number of hydration water molecules around S which is 9.1 ± 2.3 and 9.2 ± 2.3 for the SDS and the SDS+TP micelle systems respectively. Both histograms exhibit broad distributions ranging

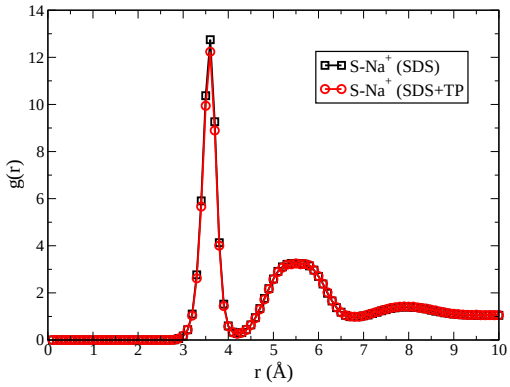

Fig. 8.16: Radial distribution functions between sulphur atoms in SDS and Na^+ counterions for the SDS and SDS+TP micelles.

from 2-15 water molecules per sulphur atom. The interfacial hydration properties were investigated further by calculating the hydration number distributions for O4 in SDS (the oxygen atom bound to sulphur and C1) and comparing them for both simulations. There is no significant difference between the distributions with and without TP so that means that the hydration of the entire headgroup is unaffected by the presence of TP.

To study the interfacial behaviour of the counterions, the $g(r)$s between the sulphur atoms in the SDS headgroup and the sodium counterions of SDS were calculated for both simulations, the resulting plots are shown in Figure 8.16. Ion shells are defined to exist when the $g(r)$ curves exhibit a peak followed by a trough. The first and second shells of sodium ions are located at 4.2 Å and 6.8 Å respectively and these values are in exact agreement with the study conducted by Bruce *et al* [153]. One way in which the data for the $g(r)$ between the sulphur atoms and sodium ions in SDS in the current study deviates from that of Bruce *et al* is that they obtain a "slight ledge" before the first peak whereas Figure 8.16 shows a smooth first peak. They postulate that the ledge they observe arises as a result of the favourable electrostatic interactions with three of the four headgroup oxygen atoms such that the sodium ion resides in the "pocket" formed by the tetrahedrally coordinated sulphur atom of the headgroup. This discrepancy between the $g(r)$s is most likely caused by

differences in the chosen forcefields in the respective simulations as choice of forcefield is known to affect counterion distribution [75]. Comparing the abundance of sodium ions in the first and second ion shells in both simulations revealed that the occupation of ions was similar for both systems but slightly less for the SDS+TP micelle. For the SDS micelle, it was found that 21% of the sodium ions occupy the first shell whilst 48% were contained within the first two shells. For the SDS+TP micelle, 17% were situated in the first shell while 43% were found in the first two shells.

To establish how the TP affects the local concentration of ions, the distribution of sodium ions within the nearest neighbour distance of the sulphur atoms that were closest and furthest away from any TP molecule were compared over every simulation snapshot. The probability that one of the sulphur atoms closest to the TP molecules have 1 or 2 sodium counterions bound to them was determined to be 0.31. This is significantly larger than for the sulphur atoms which were furthest away: 0.14. For comparison, the probability of a sulphur atom being bound to 1 or 2 Na^+ counterions is 0.19 in the SDS micelle. Therefore, it appears that TP molecules attract the Na^+ counterions. Consulting the $g(r)$ curves between Na^+ and the oxygen atoms in the TP molecules there are very prominent first neighbour peaks for the O1-Na^+ and O2-Na^+ interactions at a distance of ~ 3.0 Å.

8.3 Conclusions

Atomistic molecular dynamics simulations have been used to investigate the structural and interfacial properties of SDS micelles with and without the presence of TP. These micelles were created using the aggregation numbers found from recent neutron scattering data which is different from the aggregation number of 60 that has been previously used in most simulation studies of SDS micelles in aqueous environments. Also, care has been taken to carry out the micelle simulations at the

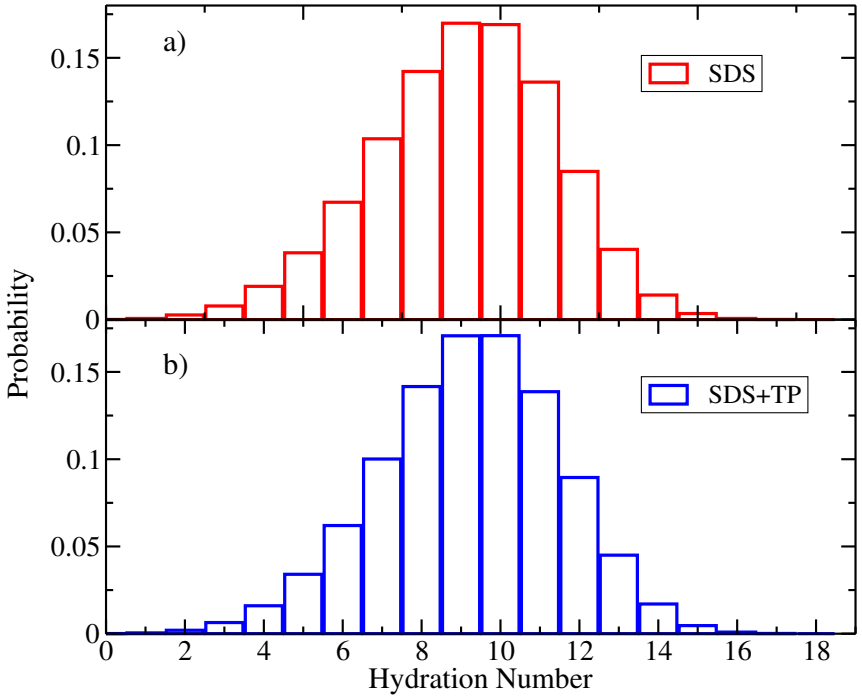

Fig. 8.17: Histograms showing the probability that a sulphur atom in the SDS headgroup has a given hydration number for a) the SDS and b) SDS+TP micelle.

same concentration of the SDS as was used experimentally, therefore reproducing the experimental system as accurately as possible. The structural properties of the SDS micelle that were calculated for the micelle systems reported in this chapter are consistent with those that have been published previously for micelles consisting of different numbers of SDS molecules.

It has been found that the SDS micelle was slightly non-spherical with an average eccentricity of 0.11, which is nearly identical to the values reported for micelles consisting of 60 SDS molecules [112, 153, 158, 161] and is a bit smaller but within error of the value reported by Palazzesi *et al.*[154] The earlier simulations that showed more spherical micelles were very short simulations and so the shape of the micelle had most likely not equilibrated [151, 152].

The surface area of the SDS micelle that was simulated in this chapter (SASA:$\sim$ 170 Å^2/molecule, Voronoi: $\sim$ 150 Å^2/molecule) is comparable to the values obtained from other recent simulation studies of SDS micelles containing 60 molecules in an

aqueous environment including 176 Å^2/molecule [153], and 147 Å^2/molecule [154]. However, in the current micelle systems which have a larger aggregation number than the micelle studied by Bruce *et al.*, a larger amount of the surface area consists of contributions from hydrocarbon atoms at the interface (58%) than was found by Bruce *et al.* ($\sim$ 30%) [142].

A novel method to construct the micelle intrinsic surface was proposed and applied to analysis. This helped to elucidate the position of TP molecules within the SDS+TP micelle system by calculating the intrinsic density of different atomic species in the system. Moreover, this intrinsic surface was useful when studying the orientation of water molecules and also enabled the Gaussian curvature of the micelle surface to be calculated.

The interfacial properties of the SDS micelles reported in this chapter are also consistent with those found in other MD simulation studies of similar systems. The hydration numbers that were obtained for the sulphur atom in the headgroup of the SDS molecules ($\sim$ 9.1) is nearly identical to that found by Rakitin and Pack ($\sim$ 9.4)[112] and is only slightly larger than that found by Sammalkorpi *et al.* ($\sim$ 8.0) who studied the self-assembly process of micelles and therefore had a distribution of micelle sizes within their system [159]. The proportion of Na^+ counterions found within the distances corresponding to the first and second minima in the $g(r)$ curves between Na^+ counter-ions and the sulphur atoms in the SDS headgroup is consistent with the majority of other simulation studies [112, 153, 156]. Meanwhile, Sammalkorpi *et al.* found a significantly smaller proportion of Na^+ counterions bound to the sulphur atoms of the headgroup [159], but Palazzesi *et al.* found a significantly larger proportion of bound Na^+ ions. This is not too surprising as this seems to be the most variable interaction observed when using different force fields for the simulation [160].

The solubilisation process of TP molecules within an SDS micelle has been studied in detail. The TP molecules preferentially sit at the micelle surface and interact

predominantly with the polar SDS headgroups. In some instances they seem to interact with carbons on the hydrocarbon chain of SDS that are at the surface of the micelle. Even though the TP is found at the interface, it has no observable effect on the hydration of the headgroup of the SDS molecules in the micelle. There does however seem to be a correlation between the distribution of the Na^+ counterions at the micelle's surface and the location of the TP on the surface. At a given instance, an SDS headgroup which is closest to a TP molecule is twice as likely to be bound to 1 or 2 Na^+ counterions than the SDS headgroup which is furthest away from the TP molecules. After the TP adsorb onto the surface of the micelle they are able to diffuse along the surface of the micelle in order to find preferential locations with relation to one another. In doing so, the TP appear to prefer to be more or less equally spaced on the micelle's surface.

A natural extension of the work presented in this chapter would be to utilise the distance from drug molecule to the micelle intrinsic surface (d_{int}) as a collective variable to perform metadynamics calculations of the encapsulation of TP (and other testosterone-based compounds) within surfactant micelles. This would provide a useful compliment to the simulations performed in Chapter 6 which studied the free energy of testosterone-based compounds interacting with SDS monolayers. Such simulations have been started, however they have not reached convergence at the time of writing this thesis.

Chapter 9

Conclusions and Outlook

Throughout the course of this thesis, surfactant monolayers and micelles interacting with testosterone-based compounds have been investigated using both classical molecular dynamics and metadynamics simulation techniques. This has enabled the study of structural and interfacial properties of the resulting aggregate structures. These simulations have been successful in developing an understanding of the encapsulation behaviour of the testosterone-based compounds, and how this is affected by the chemical composition of the counterion species and the drug compound. The results obtained in this thesis are relevant to the rational design of oral drug formulations in the future.

The simulations of dodecyl sulphate monolayers in the presence of different counterions revealed that the choice of counterion species can have drastic effects on the interfacial properties such as the hydration of surfactant headgroups, and salt bridging behaviour. Spatial density maps affirm that the ammonium ions directly compete with the hydrating water molecules for hydrogen bonds with the surfactant headgroup. This process causes the ADS monolayers to be the least hydrated of the monolayers studied. Furthermore, a significant increase in the salt bridging between the DS^- headgroups is seen when ammonium ions are present than when sodium ions are, which would result in a stronger association between the headgroups at

the micelle's surface. It is suspected that the differences in how counterion species interact with the surfactant headgroups stated above could be a prominent factor in producing the discrepancy between the observed encapsulation abilities of aggregates. Specifically, *Saaka* performed neutron scattering experiments which indicated that SDS and ADS micelles were the most and least successful surfactants, respectively, for encapsulating testosterone-based compounds [32].

The simulations of monolayers interacting with testosterone-based compounds presented in Chapter 4 revealed that the chemistry of the drug molecule and the number of drug molecules present within a monolayer have little effect on the monolayer interfacial properties. Furthermore, it has been determined that the ADS monolayers contain 50 % less water than the SDS monolayers which could be a crucial factor in explaining the lower encapculation capacity of ADS aggregates compared to SDS, due to the decreased potential for drug compounds to form hydrogen bonds with water molecules within the monolayer. This hypothesis could be further tested by conducting simulations of more highly polar drug molecules within the surfactant monolayers studied in this thesis. The interaction of the testosterone-based compounds within the monolayers was characterised by monitoring their position and orientation within the monolayers. This analysis revealed that the preferential orientation of the different drug compounds varies, depending on how deep into the monolayer tail region they are situated. Notably, drug molecules situated in the monolayer tail region near the headgroups adopt a perpendicular orientation with respect to the z-axis, whereas drug molecules inserted deeper into the monolayer tend to orient themselves such that they are approximately parallel to the z-axis, with their O1 atoms in contact with the water. This process enables hydrogen bonding between the O1 atoms in the drug molecules and water molecules, whilst the nonpolar ester chain is situated towards the vacuum region. This orientation preference is a relevant property to consider when designing drug formulations for oral delivery.

The interaction of the testosterone-based compounds with monolayers was then investigated further by using well-tempered metadynamics simulations to estimate the free energy of permeation of the drug molecules into SDS monolayers. These simulations yielded free energy surfaces which showed that the global free energy minimum for each of the testosterone-based compounds corresponds to a state in which the drug is located within the monolayer tail region, with the drug oriented approximately perpendicularly to the z-axis. Despite the similar form of the resulting free energy surfaces for the different drug compounds, the deepest free energy minimum was observed to be for TP which is consistent with the findings of *Saaka* [32]. The number of polar interaction sites within a drug molecule has a clear influence on its orientation within a surfactant monolayer as is clearly illustrated from the free energy surface of T, which shows very little orientational dependence on the systems free energy compared to TP or TE which both contain additional polar interaction sites and hydrophobic domains.

To the best of the author's knowledge, at the time of writing this thesis there are no examples in the literature where metadynamics simulations have incorporated a thorough treatment of the intrinsic surface of either monolayers or bilayers, when studying the free energy of permeation of solutes within these structures. The metadynamics protocol proposed in Chapter 6 can easily be applied to study the encapsulation of solutes within arbitrary monolayer and bilayer systems and should therefore be of great value in the field of biomolecular simulation in the future.

The molecular dynamics simulations of SDS micelles, with and without the presence of TP molecules presented in Chapter 8 show that the presence of TP does not significantly affect the structural or interfacial properties of the micelle. Intrinsic density plots elucidated that the preferred location of TP molecules in an SDS micelle within the micelle palisade region, interacting predominantly with the polar SDS headgroups. This finding is of great use to my experimental collaborators who had previously believed that the TP molecules preferentially reside in the micelle

core region and will be applicable to research of other, similar micelle-drug formulations. The detailed structural information provided to them from the simulations in Chapter 8 have improved the fitting of their neutron scattering data, therefore providing an example of simulation research directly contributing to experimental work. The novel method proposed in Chapter 7 and applied in Chapter 8 to construct the intrinsic surface of micelles (and other spherical nanoparticles) will be of great value to analysis of simulations of such systems in the future and can also be applied as a collective variable in metadynamics calculations of the encapsulation of solutes within micelles. Such calculations have been set up and conducted to study the encasulation of TP within both SDS and ADS micelles to probe the effect of the counterion species on the encapsulation process. These calculations have yet to reach convergence at the time of writing this thesis. This is due to the challenges of simulating such large molecular systems with limited computational resources. The preliminary free energy surface looks promising however, and it is hoped that they will elucidate the difference in the encapsulation process of TP for the sodium and ammonium counterion species in the future once convergence has been achieved.

9.1 Future Directions

For future work, metadynamics simulations should be the primary technique used to extend the work conducted in this thesis. Once the metadynamics simulations of the SDS+TP and ADS+TP micelle systems have converged, the resulting free energy surfaces should shed some light on the differences between their encapsulation behaviour and provide more insight than merely an MD simulation of an ADS micelle interacting with TP. After convergence of the SDS+TP and ADS+TP micelle systems is reached, a natural progression would be to investigate how the free energy surfaces of drug molecules encapsulated within different surfactant micelles change after incrementally adding drugs into the system. This would provide a

means to determine the encapsulation capacity of drug molecules into a particular micelle system by monitoring the change in the free energy surface as successive drug molecules are encapsulated. Presumably the depth of the global free energy minimum will decrease as more drug molecules are encapsulated within the micelle interior, until it is no longer energetically favourable for the additional drug molecule to enter the micelle due to steric packing constraints. This would require an enormous amount of computational resources so it is likely that compromises to the simulation set-up would have to be made, such as simulating the micelles in a smaller simulation box such that the concentration of surfactants would not be consistent with experiments, but would deem such a computationally exhaustive task to be feasible. Another compromise which could be made to decrease the computational resources required would be to estimate the free energy of encapsulation as a function of the depth of penetration of a drug molecule into the micelle alone, excluding the orientational CV which would leave a much smaller CV space to be sampled.

In addition to the drug delivery formulations studied in this thesis, there are many other nanoscale drug delivery systems, such as block-copolymer vesicles which should be investigated in the future, interacting with a wide range of different drug molecules permitting the comparison of encapsulation behaviour. Due to the larger, micrometre, length scales of block-copolymer vesicle systems, a coarse-grained simulation model would likely be required to achieve this and would produce challenges in force field parametrisation. The work presented within this thesis, including the novel methods proposed to describe nanoparticle interfaces is directly applicable to simulating other nanoscale drug delivery systems such as block-copolymer vesicles.

9.2 Limitations of Methodology

Whilst the simulation methodology used throughout this thesis has provided valuable insight into the molecular systems studied, such techniques are not without their drawbacks and limitations. In particular, the trajectory lengths obtainable from classical atomistic molecular dynamics simulations are limited to the order of nanoseconds which is restrictive to the sampling that can be obtained. Additionally, water molecules account for the majority of the atoms in the monolayer and micelle simulations yet an accurate description of water molecules has been, and continues to be a difficult challenge for researchers in the field. The TIP3P water model used within this thesis is not polarisable which will undoubtedly affect the accuracy of the overall dynamics. However, with the constant advancement of commerically available computational resources, these challenges will continue to be addressed and the field of molecular simulation will continue to move forward and play a key role in solving some of the most important problems in society.

References

[1] S. Singer and G. Nicolson, "The fluid mosaic model of the structure of cell membranes," *Science*, vol. 175, no. 4023, pp. 720–731, 1972.

[2] G. L. Nicolson, "The fluid—mosaic model of membrane structure: Still relevant to understanding the structure, function and dynamics of biological membranes after more than 40 years," *BBA-Biomembranes*, vol. 1838, no. 6, pp. 1451 – 1466, 2014.

[3] G. van Meer, D. R. Voelker, and G. W. Feigenson, "Membrane lipids: where they are and how they behave," *Nat. Rev. Mol. Cell Biol.*, vol. 9, no. 2, pp. 112–124, 2008.

[4] S. De, S. Malik, A. Ghosh, R. Saha, and B. Saha, "A review on natural surfactants," *RSC Adv.*, vol. 5, pp. 65757–65767, 2015.

[5] P. L. du Noüy, "An Interfacial Tensiometer For Universal Use," *J. Gen. Physiol*, vol. 7, no. 5, pp. 625–631, 1925.

[6] A. M. Khan and S. S. Shah, "Determination of critical micelle concentration (Cmc) of sodium dodecyl sulfate (SDS) and the effect of low concentration of pyrene on its Cmc using ORIGIN software," *J. Chem. Soc. Pakistan*, vol. 30, no. 2, p. 186, 2008.

[7] E. Goddard, N. Turro, P. Kuo, and K. Ananthapadmanabhan, "Fluorescence probes for critical micelle concentration determination," *Langmuir*, vol. 1, no. 3, pp. 352–355, 1985.

[8] L. I. Schramm, *Emulsions, Foams and Suspensions: Fundamentals and Applications*. WILEY-VCH Verag GmbH & Co. KGaA, 2005.

[9] S. Paria and K. C. Khilar, "A review on experimental studies of surfactant adsorption at the hydrophilic solid–water interface," *Adv. Drug Delivery Rev.*, vol. 45, pp. 89–121, 2000.

[10] L. Cohen, M. Martin, F. Soto, F. Trujillo, and E. Sanchez, "The Effect of Counterions of Linear Alkylbenzene Sulfonate on Skin Compatibility," *J. Surfactants Deterg.*, vol. 19, no. 1, pp. 219–222, 2016.

[11] T. S. Banipal, H. Kaur, A. Kaur, and P. K. Banipal, "Effect of tartarate and citrate based food additives on the micellar properties of sodium dodecylsulfate for prospective use as food emulsifier.," *Food Chem.*, vol. 190, pp. 599–606, 2016.

[12] S. Kumar and A. Mandal, "Studies on interfacial behavior and wettability change phenomena by ionic and nonionic surfactants in presence of alkalis and salt for enhanced oil recovery," *Appl. Surf. Sci.*, vol. 372, pp. 42–51, 2016.

[13] M. V. Pattarkine and K. N. Ganesh, "DNA–Surfactant Interactions: Coupled Cooperativity in Ligand Binding Leads to Duplex Stabilization," *Biochem. Bioph. Res. Co.*, vol. 263, no. 1, pp. 41 – 46, 1999.

[14] M. J. Lawrence and G. D. Rees, "Microemulsion-Based Media as Novel Drug Delivery Systems," *Adv. Colloid Interface Sci.*, vol. 110, no. 3, pp. 75–95, 2004.

[15] B. E. Rabinow, "Nanosuspensions in Drug Delivery," *Nat. Rev. Drug Discovery*, vol. 3, pp. 785–796, 2004.

[16] B. Mishra, B. B. Patel, and S. Tiwari, "Colloidal nanocarriers: a review on formulation technoloy, types and applications toward targeted delivery," *Nanomed. Nanotech. Bio. Med.*, vol. 6, no. 1, pp. 9–24, 2010.

[17] M. Ramanathan, L. K. Shrestha, T. Mori, Q. Ji, J. P. Hill, and K. Ariga, "Amphiphile nanoarchitectonics: from basic physical chemistry to advanced applications," *PCCP*, vol. 15, pp. 10580–10611, 2013.

[18] C. Tanford, "Thermodynamics of Micelle Formation: Prediction of Micelle Size and Size Distribution," *P. Natl. Acad. Sci. USA*, vol. 71, no. 5, pp. 1811–1815, 1974.

[19] J. N. Israelachvili, D. J. Mitchell, and B. W. Ninham, "Theory of self-assembly of hydrocarbon amphiphiles into micelles and bilayers," *J. Chem. Soc. Faraday Trans. 2*, vol. 72, no. 0, pp. 1525–1568, 1976.

[20] T. Li, A. J. Senesi, and B. Lee, "Small Angle X-ray Scattering for Nanoparticle Research," *Chem. Rev.*, vol. 116, no. 18, pp. 11128–11180, 2016.

[21] D. A. Jacques and J. Trewhella, "Small-angle scattering for structural biology—Expanding the frontier while avoiding the pitfalls," *Protein Sci.*, vol. 19, no. 4, pp. 642–657, 2010.

[22] M. M. Borner, P. Schöffski, R. de Wit, F. Caponigro, G. Comella, A. Sulkes, G. Greim, G. J. Peters, K. van der Born, J. Wanders, R. F. de Boer, C. Martin, and P. Fumoleau, "Patient preference and pharmacokinetics of oral modulated UFT versus intravenous fluorouracil and leucovorin," *Eur. J. Cancer*, vol. 38, no. 3, pp. 349–358, 2017.

[23] P. Pfeiffer, J. P. Mortensen, B. Bjerregaard, L. Eckhoff, K. Schønnemann, E. Sandberg, K. Aabo, and A. Jakobsen, "Patient preference for oral or intravenous chemotherapy: A randomised cross-over trial comparing capecitabine and Nordic fluorouracil/leucovorin in patients with colorectal cancer," *Eur. J. Cancer*, vol. 42, no. 16, pp. 2738–2743, 2017.

[24] N. A. Peppas and N. J. Kavimandan, "Nanoscale analysis of protein and peptide absorption: Insulin absorption using complexation and ph-sensitive hydrogels as delivery vehicles," *Eur. J. Pharm. Sci.*, vol. 29, no. 3–4, pp. 183 – 197, 2006.

[25] A. Müllertz, A. Ogbonna, S. Ren, and T. Rades, "New perspectives on lipid and surfactant based drug delivery systems for oral delivery of poorly soluble drugs," *J. Pharm. Pharmacol.*, vol. 62, no. 11, pp. 1622–1636, 2010.

[26] P. L. Toutain and A. Bousquet-Mélou, "Bioavailability and its assessment," *J. Vet. Pharmacol. Ther.*, vol. 27, no. 6, pp. 455–466, 2004.

[27] T. Kimura and H. K, "Gastrointestinal transit and drug absorption.," *Biol. Pharm. Bull.*, vol. 25, no. 2, pp. 149–164, 2002.

[28] R. N. Gursoy and S. Benita, "Self-emulsifying drug delivery systems (SEDDS) for improved oral delivery of lipophilic drugs," *Biomed. Pharmacother.*, vol. 58, no. 3, pp. 173 – 182, 2004.

[29] C. A. Lipinski, "Drug-like properties and the causes of poor solubility and poor permeability," *J. Pharmacol. Toxicol. Methods*, vol. 44, no. 1, pp. 235 – 249, 2000.

[30] J. P. Rao and K. E. Geckeler, "Polymer nanoparticles: Preparation techniques and size-control parameters," *Prog. Polym. Sci.*, vol. 36, no. 7, pp. 887 – 913, 2011.

[31] A. Kumari, S. K. Yadav, and S. C. Yadav, "Biodegradable polymeric nanoparticles based drug delivery systems," *Colloids Surf. B Biointerfaces*, vol. 75, no. 1, pp. 1 – 18, 2010.

[32] Y. Saaka, *Effect of surfactant headgroup on the micellar solubilisation of poorly water soluble drugs.* PhD Thesis, University of London, 2016.

[33] B. J. Alder and T. E. Wainwright, "Phase Transition for a Hard Sphere System," *J. Chem. Phys.*, vol. 27, no. 5, pp. 1208–1209, 1957.

[34] A. Rahman, "Correlations in the Motion of Atoms in Liquid Argon," *Phys. Rev.*, vol. 136, pp. A405–A411, 1964.

[35] F. H. Stillinger and A. Rahman, "Improved simulation of liquid water by molecular dynamics," *J. Chem. Phys.*, vol. 60, no. 4, pp. 1545–1557, 1974.

[36] S. Sun, J. T. Y. Wong, and T.-Y. Zhang, "Molecular dynamics simulations of phase transition of lamellar lipid membrane in water under an electric field," *Soft Matter*, vol. 7, pp. 147–152, 2011.

[37] K. Lindorff-Larsen, N. Trbovic, P. Maragakis, S. Piana, and D. E. Shaw, "Structure and Dynamics of an Unfolded Protein Examined by Molecular Dynamics Simulation," *J. Am. Chem. Soc.*, vol. 134, no. 8, pp. 3787–3791, 2012.

[38] S. K. Sinha and S. Bandyopadhyay, "Dynamic properties of water around a protein-dna complex from molecular dynamics simulations.," *J. Chem. Phys.*, vol. 135, no. 13, p. 135101, 2011.

[39] J. Gsponer and A. Caflisch, "Molecular dynamics simulations of protein folding from the transition state.," *P. Natl. Acad. Sci. USA*, vol. 99, no. 10, pp. 6719–24, 2002.

[40] O.-S. Lee, V. Cho, and G. C. Schatz, "Modeling the Self-Assembly of Peptide Amphiphiles into Fibers Using Coarse-Grained Molecular Dynamics," *Nano Lett.*, vol. 12, no. 9, pp. 4907–4913, 2012.

[41] W. L. Ash, M. R. Zlomislic, E. O. Oloo, and D. P. Tieleman, "Computer simulations of membrane proteins," *BBA-Biomembranes*, vol. 1666, no. 1–2, pp. 158 – 189, 2004.

[42] A. J. Cohen, P. Mori-Sánchez, and W. Yang, "Challenges for Density Functional Theory," *Chem. Rev.*, vol. 112, no. 1, pp. 289–320, 2012.

[43] K. Burke and L. O. Wagner, "DFT in a nutshell," *Int. J. Quantum Chem.*, vol. 113, no. 2, pp. 96–101, 2013.

[44] S. Lifson and A. Warshel, "Consistent force field for calculations of conformations, vibrational spectra, and enthalpies of cycloalkane and nalkane molecules," *J. Chem. Phys.*, vol. 49, no. 11, pp. 5116–5129, 1968.

[45] B. H. Besler, K. M. Merz, and P. A. Kollman, "Atomic Charges Derived from Semiempirical Methods," *J. Comput. Chem.*, vol. 11, pp. 431–439, May 1990.

[46] W. D. Cornell, P. Cieplak, C. I. Bayly, I. R. Gould, K. M. Merz, D. M. Ferguson, D. C. Spellmeyer, T. Fox, J. W. Caldwell, and P. A. Kollman, "A Second Generation Force Field for the Simulation of Proteins, Nucleic Acids, and Organic Molecules," *J. Am. Chem. Soc.*, vol. 117, no. 19, pp. 5179–5197, 1995.

[47] D. A. Case *et al.*, "AMBER 12," 2012.

[48] B. Brooks *et al.*, "CHARMM: the biomolecular simulation program,"

[49] T. Darden, D. York, and L. Pedersen, "Particle mesh ewald: An nlog(n) method for ewald sums in large systems," *J. Chem. Phys.*, vol. 98, no. 12, pp. 10089–10092, 1993.

[50] L. Monticelli and E. Salonen, *Biomolecular simulations*. Humana Press, 1 ed., 2013.

[51] L. Martinez, R. Andrade, E. G. Birgin, and J. M. Martinez, "PACKMOL: a package for building initial configurations for molecular dynamics simulations.," *J. Comput. Chem.*, vol. 30, no. 13, pp. 2157–64, 2009.

[52] M. Bartholomew-Biggs, *The Steepest Descent Method*, pp. 1–8. Boston, MA: Springer US, 2008.

[53] M. Born and R. Oppenheimer, "Zur Quantentheorie der Molekeln," *Annalen der Physik*, vol. 389, no. 20, pp. 457–484, 1927.

[54] L. Verlet, "Computer "Experiments" on Classical Fluids. I. Thermodynamical Properties of Lennard-Jones Molecules," *Phys. Rev.*, vol. 159, pp. 98–103, 1967.

[55] D. Fincham, "Choice of timestep in molecular dynamics simulation," *Comput. Phys. Commun.*, vol. 40, no. 2, pp. 263 – 269, 1986.

[56] J.-P. Ryckaert, G. Ciccotti, and H. J. Berendsen, "Numerical integration of the cartesian equations of motion of a system with constraints: molecular dynamics of n-alkanes," *J. Comput. Phys.*, vol. 23, no. 3, pp. 327 – 341, 1977.

[57] H. J. C. Berendsen, J. P. M. Postma, W. F. van Gunsteren, A. DiNola, and J. R. Haak, "Molecular dynamics with coupling to an external bath," *J. Chem. Phys.*, vol. 81, no. 8, pp. 3684–3690, 1984.

[58] H. C. Andersen, "Molecular dynamics simulations at constant pressure and/or temperature," *J. Chem. Phys.*, vol. 72, no. 4, pp. 2384–2393, 1980.

[59] W. G. Hoover, "Canonical dynamics: Equilibrium phase-space distributions," *Phys. Rev. A*, vol. 31, pp. 1695–1697, 1985.

[60] W. G. Hoover, "Constant-pressure equations of motion," *Phys. Rev. A*, vol. 34, pp. 2499–1697, 1986.

[61] M. P. Allen, "Introduction to Molecular Dynamics simulation," *Lecture Notes from The John von Neumann Institute for Computing*, 2004.

[62] P. Larsson, B. Hess, and E. Lindahl, "Algorithm improvements for molecular dynamics simulations," *Wiley Interdiscip. Rev. Comput. Mol. Sci.*, vol. 1, no. 1, pp. 93–108, 2011.

[63] K. M. Dyer, J. S. Perkyns, G. Stell, and B. M. Pettitt, "Site-renormalised molecular fluid theory: on the utility of a two-site model of water," *Mol. Phys.*, vol. 107, no. 4-6, pp. 423–431, 2009.

[64] H. Nada and J. P. J. M. van der Eerden, "An intermolecular potential model for the simulation of ice and water near the melting point: A six-site model of H2O," *J. Chem. Phys.*, vol. 118, no. 16, pp. 7401–7413, 2003.

[65] W. L. Jorgensen, J. Chandrasekhar, J. D. Madura, R. W. Impey, and M. L. Klein, "Comparison of simple potential functions for simulating liquid water," *J. Chem. Phys.*, vol. 79, no. 2, pp. 926–935, 1983.

[66] W. I. Reiher, *Theoretical Studies of Hydrogen Bonding.* Ph.D. dissertation, Harvard University, 1985.

[67] P. Mark and L. Nilsson, "Structure and Dynamics of the TIP3P, SPC, and SPC/E Water Models at 298 K," *J. Phys. Chem. A*, vol. 105, no. 43, pp. 9954–9960, 2001.

[68] A. Barducci, G. Bussi, and M. Parrinello, "Well-Tempered Metadynamics: A Smoothly Converging and Tunable Free-Energy Method," *Phys. Rev. Lett.*, vol. 100, p. 020603, 2008.

[69] T. Kawai, H. Kamio, T. Kondo, and K. Kon-No, "Effects of concentration and temperature on SDS monolayers at the air-solution interface studied by infrared external reflection spectroscopy.," *J. Phys. Chem. B*, vol. 109, no. 10, pp. 4497–500, 2005.

[70] S. Plimpton, "Fast parallel algorithms for short-range molecular dynamics," *J. Comput. Phys.*, vol. 117, no. 1, pp. 1 – 19, 1995.

[71] K. Vanommeslaeghe *et al.*, "CHARMM General Force Field (CGenFF): A Force Field for Drug-like Molecules Compatible with the CHARMM All-Atom Additive Biological Force Fields," *J. Comput. Chem.*, vol. 31, pp. 671–690, 2010.

[72] W. Yu, K. Vanommeslaeghe, and A. D. J. MacKerell, "Extension of the CHARMM General Force Field to Sulgonyl-Containing Compounds and its Utility to Biomolecular Simulations," *J. Comput. Chem.*, vol. 33, pp. 2451–2468, 2012.

[73] J. B. Klauda *et al.*, "Update of the CHARMM All-Atom Additive Force Field for Lipids: Validation on Six Lipid Types," *J. Phys. Chem. B*, vol. 114, pp. 7830–7843, 2010.

[74] R. W. Pastor and A. D. J. MacKerell, "Development of the CHARMM Force Fields for Lipids," *J. Phys. Chem. Lett.*, vol. 2, pp. 1526–1532, 2011.

[75] X. Tang, P. H. Koenig, and R. G. Larson, "Molecular Dynamics Simulations of Sodium Dodecyl Sulfate Micelles in Water—The Effect of the Force Field," *J. Phys. Chem. B*, vol. 118, no. 14, pp. 3864–3880, 2014.

[76] D. T. Allen, Y. Saaka, M. J. Lawrence, and C. D. Lorenz, "Atomistic description of the solubilisation of testosterone propionate in a sodium dodecyl sulfate micelle.," *J. Phys. Chem. B*, vol. 118, no. 46, pp. 13192–201, 2014.

[77] W. G. Hoover, "Canonical dynamics: Equilibrium phase-space distributions," *Phys. Rev. A*, vol. 31, pp. 1695–1697, 1985.

[78] E. Chacón and P. Tarazona, "Intrinsic Profiles beyond the Capillary Wave Theory: A Monte Carlo Study," *Phys. Rev. Lett.*, vol. 91, p. 166103, 2003.

[79] H. Martínez, E. Chacón, P. Tarazona, and F. Bresme, "The intrinsic interfacial structure of ionic surfactant monolayers at water–oil and water–vapour interfaces," *P. Roy. Soc. Lond. A Mat.*, vol. 467, no. 2131, pp. 1939–1958, 2011.

[80] A. P. Willard and D. Chandler, "Instantaneous Liquid Interfaces," *J. Phys. Chem. B*, vol. 114, no. 5, pp. 1954–1958, 2010.

[81] S. A. Pandit, D. Bostick, and M. L. Berkowitz, "An algorithm to describe molecular scale rugged surfaces and its application to the study of a water/lipid bilayer interface," *J. Chem. Phys.*, vol. 119, no. 4, pp. 2199–2205, 2003.

[82] J. R. Lu, A. Marrocco, T. J. Su, R. K. Thomas, and J. Penfold, "Adsorption of Dodecyl Sulfate Surfactants with Monovalent Metal Counterions at the Air-Water Interface Studied by Neutron Reflection and Surface Tension," *J. Colloid Interface Sci.*, vol. 158, no. 2, pp. 303–316, 1993.

[83] S. G. Oh and D. O. Shah, "Effect of counterions on the interfacial tension and emulsion droplet size in the oil/water/dodecyl sulfate system," *J. Phys. Chem.*, vol. 97, no. 2, pp. 284–286, 1993.

[84] J. R. Lu, M. Hromadova, E. A. Simister, R. K. Thomas, and J. Penfold, "Neutron Reflection from Hexadecyltrimethylammonium Bromide Adsorbed at the Air/Liquid Interface: The Variation of the Hydrocarbon Chain Distribution with Surface Concentration," *J. Phys. Chem.*, vol. 98, no. 44, pp. 11519–11526, 1994.

[85] D. J. Lyttle, J. R. Lu, T. J. Su, R. K. Thomas, and J. Penfold, "Structure of a Dodecyltrimethylammonium Bromide Layer at the Air/Water Interface Determined by Neutron Reflection: Comparison of the Monolayer Structure of Cationic Surfactants with Different Chain Lengths," *Langmuir*, vol. 11, no. 3, pp. 1001–1008, 1995.

[86] J. Lu, R. Thomas, and J. Penfold, "Surfactant layers at the air/water interface: structure and composition," *Adv. Colloid Interface Sci.*, vol. 84, no. 1-3, pp. 143–304, 2000.

[87] T. Gilányi, I. Varga, and R. Mészáros, "Specific counterion effect on the adsorption of alkali decyl sulfate surfactants at air/solution interface," *PCCP*, vol. 6, no. 17, pp. 4338–4346, 2004.

[88] C. M. Johnson and E. Tyrode, "Study of the adsorption of sodium dodecyl sulfate (SDS) at the air/water interface: targeting the sulfate headgroup using vibrational sum frequency spectroscopy.," *PCCP*, vol. 7, no. 13, pp. 2635–40, 2005.

[89] V. L. Shapovalov and G. Brezesinski, "Breakdown of the Gouy-Chapman model for highly charged Langmuir monolayers: counterion size effect.," *J. Phys. Chem. B*, vol. 110, no. 20, pp. 10032–40, 2006.

[90] M. Sovago, G. W. H. Wurpel, M. Smits, M. Müller, and M. Bonn, "Calcium-induced phospholipid ordering depends on surface pressure.," *J. Am. Chem. Soc.*, vol. 129, no. 36, pp. 11079–84, 2007.

[91] C. Wang and H. Morgner, "Effects of counterions on adsorption behavior of anionic surfactants on solution surface.," *Langmuir*, vol. 26, no. 5, pp. 3121–5, 2010.

[92] P. Brown, C. Butts, R. Dyer, J. Eastoe, I. Grillo, F. Guittard, S. Rogers, and R. Heenan, "Anionic surfactants and surfactant ionic liquids with quaternary ammonium counterions.," *Langmuir*, vol. 27, no. 8, pp. 4563–71, 2011.

[93] R. A. Livingstone, Y. Nagata, M. Bonn, and E. H. G. Backus, "Two Types of Water at the Water-Surfactant Interface Revealed by Time-Resolved Vibrational Spectroscopy.," *J. Am. Chem. Soc.*, vol. 137, no. 47, pp. 14912–9, 2015.

[94] A. P. Dabkowska, L. E. Collins, D. J. Barlow, R. Barker, S. E. McLain, M. J. Lawrence, and C. D. Lorenz, "Comparative atomic-scale hydration of the ceramide and phosphocholine headgroup in solution and bilayer environments," *J. Chem. Phys.*, vol. 144, no. 22, p. 225101, 2016.

[95] D. Hu, A. Mafi, and K. C. Chou, "Revisiting the Thermodynamics of Water Surfaces and the Effects of Surfactant Head Group.," *J. Phys. Chem. B*, 2016.

[96] K. J. Schweighofer, U. Essmann, and M. Berkowitz, "Simulation of Sodium Dodecyl Sulfate at the WaterVapor and WaterCarbon Tetrachloride Interfaces at Low Surface Coverage," *J. Phys. Chem. B*, vol. 101, no. 19, pp. 3793–3799, 1997.

[97] P. A. Kralchevsky, K. D. Danov, G. Broze, and A. Mehreteab, "Thermodynamics of Ionic Surfactant Adsorption with Account for the Counterion Binding: Effect of Salts of Various Valency," *Langmuir*, vol. 15, no. 7, pp. 2351–2365, 1999.

[98] H. Kuhn and H. Rehage, "Molecular Dynamics Computer Simulations of Surfactant Monolayers: Monododecyl Pentaethylene Glycol at the Surface between Air and Water," *J. Phys. Chem. B*, vol. 103, no. 40, pp. 8493–8501, 1999.

[99] H. Dominguez and M. L. Berkowitz, "Computer Simulations of Sodium Dodecyl Sulfate at Liquid/Liquid and Liquid/Vapor Interfaces," *J. Phys. Chem. B*, vol. 104, no. 22, pp. 5302–5308, 2000.

[100] C. D. Lorenz and A. Travesset, "Atomistic simulations of Langmuir monolayer collapse," *Langmuir*, vol. 22, no. 24, pp. 10016–10024, 2006.

[101] G. Hantal, L. B. Partay, I. Varga, P. Jedlovszky, and T. Gilányi, "Counterion and surface density dependence of the adsorption layer of ionic surfactants at the vapor-aqueous solution interface: a computer simulation study.," *J. Phys. Chem. B*, vol. 111, no. 7, pp. 1769–74, 2007.

[102] J. J. Giner Casares, L. Camacho, M. T. Martín-Romero, and J. J. López Cascales, "Effect of Na+ and Ca2+ ions on a lipid Langmuir monolayer: an atomistic description by molecular dynamics simulations.," *ChemPhysChem*, vol. 9, no. 17, pp. 2538–43, 2008.

[103] L. Shi, N. R. Tummala, and A. Striolo, "C12E6 and SDS surfactants simulated at the vacuum-water interface.," *Langmuir*, vol. 26, no. 8, pp. 5462–74, 2010.

[104] T. Zhao, G. Xu, S. Yuan, Y. Chen, and H. Yan, "Molecular dynamics study of alkyl benzene sulfonate at air/water interface: effect of inorganic salts.," *J. Phys. Chem. B*, vol. 114, no. 15, pp. 5025–33, 2010.

[105] H. Yan, X.-L. Guo, S.-L. Yuan, and C.-B. Liu, "Molecular dynamics study of the effect of calcium ions on the monolayer of SDC and SDSn surfactants at the vapor/liquid interface.," *Langmuir*, vol. 27, no. 10, pp. 5762–71, 2011.

[106] M. Chen, X. Lu, X. Liu, Q. Hou, Y. Zhu, and H. Zhou, "Temperature-dependent phase transition and desorption free energy of sodium dodecyl sulfate at the water/vapor interface: approaches from molecular dynamics simulations.," *Langmuir*, vol. 30, no. 35, pp. 10600–7, 2014.

[107] M. Chen, X. Lu, X. Liu, Q. Hou, Y. Zhu, and H. Zhou, "Specific Counterion Effects on the Atomistic Structure and Capillary-Waves Fluctuation of the Water/Vapor Interface Covered by Sodium Dodecyl Sulfate," *J. Phys. Chem. C*, vol. 118, no. 33, pp. 19205–19213, 2014.

[108] J.-H. Kim, M. M. Domach, and R. D. Tilton, "Effect of Electrolytes on the Pyrene Solubilization Capacity of Dodecyl Sulfate Micelles," *Langmuir*, vol. 16, no. 26, pp. 10037–10043, 2000.

[109] S. S. Berr, M. J. Coleman, R. R. M. Jones, and J. S. Johnson, "Small-angle neutron scattering study of the structural effects of substitution of tetramethylammonium for sodium as the counterion in dodecyl sulfate micelles," *J. Phys. Chem.*, vol. 90, no. 24, pp. 6492–6499, 1986.

[110] S. Chen, "small angle neutron scattering studies of the structure and interaction in micellar and microemulsion systems," *Ann. Rev. Phy. Chem.*, vol. 37, pp. 351–399, 1986.

[111] M. Benrraou, B. L. Bales, and R. Zana, "Effect of the Nature of the Counterion on the Properties of Anionic Surfactants. 1. Cmc, Ionization Degree at the Cmc and Aggregation Number of Micelles of Sodium, Cesium, Tetramethylammonium, Tetraethylammonium, Tetrapropylammonium, and Tetrabutylammoniu," *J. Phys. Chem. B*, vol. 107, no. 48, pp. 13432–13440, 2003.

[112] A. R. Rakitin and G. R. Pack, "Molecular dynamics simulations of ionic interactions with dodecyl sulfate micelles," *J. Phys. Chem. B*, vol. 108, pp. 2712–2716, 2004.

[113] C. M. Tcacenco, R. Zana, and B. L. Bales, "Effect of the nature of the counterion on the properties of anionic surfactants. 5. Self-association behavior and micellar properties of ammonium dodecyl sulfate.," *J. Phys. Chem. B*, vol. 109, no. 33, pp. 15997–6004, 2005.

[114] M. Sammalkorpi, M. Karttunen, and M. Haataja, "Ionic surfactant aggregates in salene solutions: Sodium dodecyl sulfate in the presence of excess sodium chloride (NaCl) or calcium chloride ($CaCl_2$)," *J. Phys. Chem. B*, vol. 113, pp. 5863–5870, 2009.

[115] N. Schwierz, D. Horinek, U. Sivan, and R. R. Netz, "Reversed Hofmeister Series - the Rule rather than the Exception," *Curr. Opin. Colloid. In.*, 2016.

[116] D. Bastos-González, L. Pérez-Fuentes, C. Drummond, and J. Faraudo, "Ions at interfaces: the central role of hydration and hydrophobicity," *Curr. Opin. Colloid. In.*, vol. 23, pp. 19–28, 2016.

[117] U. Sivan, "The inevitable accumulation of large ions and neutral molecules near hydrophobic surfaces and small ions near hydrophilic ones," *Curr. Opin. Colloid. In.*, 2016.

[118] F. Hofmeister, "Zur Lehre von der Wirkung der Salze," *Naunyn Schmiedebergs Arch. Exp. Pathol. Pharmakol.*, vol. 25, no. 1, pp. 1–30, 1888.

[119] W. Kunz, J. Henle, and B. W. Ninham, "'Zur Lehre von der Wirkung der Salze' (about the science of the effect of salts): Franz Hofmeister's historical papers," *Curr. Opin. Colloid. In.*, vol. 9, no. 1, pp. 19–37, 2004.

[120] W. Kunz, *Specific Ion Effects*. Wiley & Sons, 2007.

[121] M. L. San-Román, M. Carrillo-Tripp, H. Saint-Martin, J. Hernández-Cobos, and I. Ortega-Blake, "A theoretical study of the hydration of li+ by monte carlo simulations with refined ab initio based model potentials," *Theor. Chem. Acc.*, vol. 115, no. 2, pp. 177–189, 2006.

[122] C. N. Rowley and B. Roux, "The Solvation Structure of Na+ and K+ in Liquid Water Determined from High Level ab Initio Molecular Dynamics Simulations," *J. Chem. Theory Comput.*, vol. 8, no. 10, pp. 3526–3535, 2012.

[123] C. F. Schwenk, T. S. Hofer, , and B. M. Rode*, ""Structure Breaking" Effect of Hydrated Cs+," *J. Phys. Chem. A*, vol. 108, no. 9, pp. 1509–1514, 2004.

[124] W. L. Jorgensen and J. Gao, "Monte Carlo simulations of the hydration of ammonium and carboxylate ions," *J. Phys. Chem.*, vol. 90, no. 10, pp. 2174–2182, 1986.

[125] S. Storm, S. Jakobtorweihen, I. Smirnova, and A. Z. Panagiotopoulos, "Molecular dynamics simulation of SDS and CTAB micellization and prediction of partition equilibria with COSMOmic," *Langmuir*, vol. 29, pp. 11582–11592, 2013.

[126] N. Yoshii, K. Iwahashi, and S. Okazaki, "A molecular dynamics study of free energy of micelle formation for sodium dodecyl sulfate in water and its size distribution," *J. Chem. Phys.*, vol. 124, no. 18, p. 184901, 2006.

[127] K. Fujimoto, N. Yoshii, and S. Okazaki, "Free energy profiles for penetration of methane and water molecules into spherical sodium dodecyl sulfate micelles obtained using the thermodynamic integration method combined with molecular dynamics calculations," *J. Chem. Phys.*, vol. 136, no. 1, p. 014511, 2012.

[128] E. Darve, D. Rodríguez-Gómez, and A. Pohorille, "Adaptive biasing force method for scalar and vector free energy calculations," *J. Chem. Phys.*, vol. 128, no. 14, p. 144120, 2008.

[129] A. Neumann, M. Wieczor, J. Zielinska, M. Baginski, and J. Czub, "Membrane Sterols Modulate the Binding Mode of Amphotericin B without Affecting Its Affinity for a Lipid Bilayer," *Langmuir*, vol. 32, no. 14, pp. 3452–3461, 2016.

[130] J. P. M. Jämbeck and A. P. Lyubartsev, "Exploring the Free Energy Landscape of Solutes Embedded in Lipid Bilayers," *J. Phys. Chem. Lett.*, vol. 4, no. 11, pp. 1781–1787, 2013.

[131] G. A. Tribello, M. Bonomi, D. Branduardi, C. Camilloni, and G. Bussi, "PLUMED 2: New feathers for an old bird," *Comput. Phys. Commun.*, vol. 185, no. 2, pp. 604–613, 2014.

[132] C. D. Lorenz, C.-M. Hsieh, C. A. Dreiss, and M. J. Lawrence, "Molecular dynamics simulations of the interfacial and structural properties of dimethyldodecylamine-N-oxide micelles," *Langmuir*, vol. 27, pp. 546–553, 2011.

[133] R. W. Hockney and J. W. Eastwood, "Computer simulation using particles," *J. Chem. Phys.*, vol. 79, pp. 926–935, 1983.

[134] M. Parrinello and A. Rahamn, "Polymorphic transitions in single crystals: A new molecular dynamics method," *J. Appl. Phys.*, vol. 52, pp. 7182–7190, 1981.

[135] G. J. Martyna, D. J. Tobias, and M. L. Klein, "Constant pressure molecular dynamics algorithms," *J. Chem. Phys.*, vol. 101, pp. 4177–4189, 1994.

[136] W. Shinoda, M. Shiga, and M. Mikami, "Rapid estimation of elastic constants by molecular dynamics simulation under constant stress," *Phys. Rev. B*, vol. 69, p. 134103, 2004.

[137] M. E. Tuckerman, J. Alejandre, R. López-Rendón, A. L. Jochim, and G. J. Martyna, "A Lioville-operator derived measure-preserving integrator for molecular dynamics simulations in isothermal-isobaric ensemble," *J. Phys. A: Math. Gen.*, vol. 39, pp. 5629–5651, 2006.

[138] J. P. Ryckaert, G. Ciccotti, and H. J. C. Berendsen, "Numerical integration of the cartesion equations of motion of a system with constraints: molecular dynamics of *n*-alkanes," *J. Comput. Phys.*, vol. 23, no. 3, pp. 327–341, 1977.

[139] T. J. Richmond, "Solvent accessible surface area and excluded volume in proteins," *J. Mol. Biol.*, vol. 178, no. 1, pp. 63 – 89, 1984.

[140] M. L. Connolly, "Computation of molecular volume," *JACS*, vol. 107, no. 5, pp. 1118–1124, 1985.

[141] C. H. Rycroft, "Voro++: A three-dimensional Voronoi cell library in C++," *Chaos*, vol. 19, p. 041111, 2009.

[142] C. D. Bruce, S. Senepati, M. L. Berkowitz, L. Perera, and M. D. E. Forbes, "Molecular dynamics simulation of sodium dodecyl sulfate micelle in water: Micellar structural characteristics and couterion distribution," *J. Phys. Chem. B*, vol. 106, pp. 10902–10907, 2002.

[143] D. T. Allen, Y. Saaka, L. C. Pardo, M. J. Lawrence, and C. D. Lorenz, "Specific effects of monovalent counterions on the structural and interfacial properties of dodecyl sulfate monolayers," *PCCP*, pp. –, 2016.

[144] J. Chowdhary and B. M. Ladanyi, "Molecular Dynamics Simulation of Aerosol-OT Reverse Micelles," *J. Phys. Chem. B*, vol. 113, no. 45, pp. 15029–15039, 2009.

[145] E. Abbena, S. Salamon, and A. Gray, *Modern Differential Geometry of Curves and Surfaces with Mathematica.* Chapman & Hall/CRC, 3 ed., 2006.

[146] A. K. Krishna and D. R. Flanagan, "Micellar solubilization of a new antimalarial drug β-arteether," *J. Pharm. Sci.*, vol. 78, no. 7, pp. 574–576, 1989.

[147] C. O. Rangel-Yagui, H. W. L. Hsu, A. Pessua, Jr., and L. Costa Tavares, "Micellar solubilization of ibuprofen - influence of surfactant head groups on the extent of solubilization," *Brazil. J. Pharm. Sci.*, vol. 41, no. 2, pp. 237–246, 2005.

[148] S. Mall, G. Buckton, and D. A. Rawkins, "Dissolution behaviour of sulphonamides into sodium dodecyl sulfate micelles: A thermodynamic approach," *J. Pharm. Sci.*, vol. 85, no. 1, pp. 75–78, 1996.

[149] S. Göktürk and S. Aslan, "Study on binding properties of poorly soluble drug trimethoprim in anionic micellar solutions," *J. Disp. Sci. Technol.*, vol. 35, pp. 84–92, 2014.

[150] M. Enache, I. Anghelache, and E. Volanschi, "Coupled spectral and electrochemical evaluation of the anticancer drug mitoxantrone-sodium dodecyl sulfate interaction," *Int. J. Pharm.*, vol. 390, pp. 100–106, 2010.

[151] J. Shelley, K. Watanabe, and M. L. Klein, "Simulation of a sodium dodecylsulfate micelle in aqueous solution," *Int. J. Quant. Chem.*, vol. 17, pp. 103–117, 1990.

[152] A. D. MacKerell Jr., "Molecular dynamics simulation analysis of a sodium dodecyl sulfate micelle in aqueous solution: Decreased fluidity of the micelle hydrocarbon interior," *J. Phys. Chem.*, vol. 99, pp. 1846–1855, 1995.

[153] C. D. Bruce, M. L. Berkowitz, L. Perera, and M. D. E. Forbes, "Molecular dynamics simulation of sodium dodecyl sulfate micelle in water: Micellar structural characteristics and couterion distribution," *J. Phys. Chem. B*, vol. 106, pp. 3788–3793, 2002.

[154] F. Palazzesi, M. Calvaresi, and F. Zerbetto, "A molecular dynamics investigation of structure and dynamics of SDS and SDBS micelles," *Soft Matter*, vol. 7, pp. 9148–9156, 2011.

[155] J. Gao, W. Ge, G. Hu, and J. Li, "From homogeneous dispersion to micelles - A molecule dynamics simulation on the compromise of the hydrophilic and hydrophobic effects of sodium dodecyl sulfate in aqueous solutions," *Langmuir*, vol. 21, pp. 5223–5229, 2005.

[156] N. Yoshii and S. Okazaki, "A molecular dynamics study of surface structure of spherical SDS micelles," *Chem. Phys. Lett.*, vol. 426, pp. 66–70, 2006.

[157] S. Jalili and M. Akhavan, "A coarse-grained molecular dynamics simulation of a sodium dodecyl sulfate micelle in aqueous solution," *Coll. Surf. A*, vol. 352, pp. 99–102, 2009.

[158] N. Yoshii and S. Okazaki, "A molecular dynamics study of structural stability of spherical SDS micelle as a function of its size," *Chem. Phys. Lett.*, vol. 426, pp. 58–61, 2006.

[159] M. Sammalkorpi, M. Karttunen, and M. Haataja, "Structural properties of ionic detergent aggregates: A large-scale molecular dynamics study of sodium dodecyl sulfate," *J. Phys. Chem. B*, vol. 111, pp. 11722–11733, 2007.

[160] X. Tang, P. H. Koenig, and R. G. Larson, "Molecular dynamics simulations of sodium dodecyl sulfate micelles in water - The effect of the forcefield," *J. Phys. Chem. B*, vol. 118, pp. 3864–4880, 2014.

[161] H. Yan, D. Cui, C. Bu-Liu, and S.-L. Yuan, "Molecular dynamics simulations of pyrene solubilized in a sodium dodecyl sulfate micelle," *Langmuir*, vol. 28, pp. 4931–4938, 2011.

[162] M. Schwarze, I. Volovych, S. Wille, L. Mokrushina, W. Arlt, and R. Schomcäcker, "Partition coefficients of itaconates in aqueous micellar solutions: Measurements and predictions with COSMO-RS," *Ind. Eng. Chem. Res.*, vol. 51, pp. 1846–1852, 2012.

Appendix A

A.1 Molecular axis sets

Fig. A.1 shows the molecular axis sets which were placed on the surfactant, water and ammonium molecules and were used to construct the spatial density maps and to investigate the molecular orientation of water molecules (via the Euler angles) in a specific region around the DS^- headgroups in Chapter 4. The axis sets are constituted of 4 pseudoatoms. These pseudoatoms can be placed by using the centre of mass position of a selection of atoms, or alternatively, they can be placed as a cross product of two vectors. This is very useful because the axes must be orthogonal to each other. Note that a slightly different set of molecular axes were used to construct the bivariate probability plots as a function of $cos(\theta_{cm})$ and ϕ_{cm} presented in the main article. The alternate frames of reference presented the results in a clearer way.

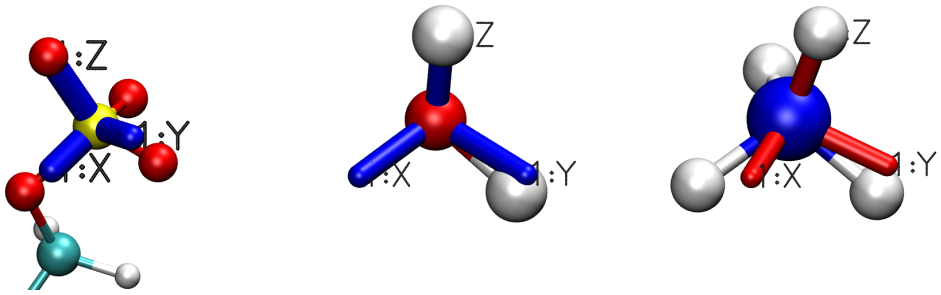

(a) DS^- **(b)** H_2O **(c)** NH_4^+

Fig. A.1: Molecular axes that were used to construct the SDMs and study the orientations of molecules for the (a) dodecyl sulfate headgroup, (b) the water molecule and the NH_4^+ counterions. The axes for the dodecyl sulfate headgroup and the water molecules are shown in blue. The axes for the NH_4^+ ions are shown in red rather than blue so as not to clash with the blue nitrogen atom.